

# MANGANESE DOPED ZnS NANOPARTICLES: SYNTHESIS, PARTICLE SIZING AND OPTICAL PROPERTIES

THÈSE N° 3029 (2004)

PRÉSENTÉE À LA FACULTÉ SCIENCES ET TECHNIQUES DE L'INGÉNIEUR

Institut des matériaux

SECTION DES MATÉRIAUX

ÉCOLE POLYTECHNIQUE FÉDÉRALE DE LAUSANNE

POUR L'OBTENTION DU GRADE DE DOCTEUR ÈS SCIENCES

PAR

**Yvonne AXMANN**

Diplom-Chemikerin, Universität Ulm, Allemagne  
et de nationalité allemande

acceptée sur proposition du jury:

Prof. H. Hofmann, directeur de thèse

Dr A. Fink, rapporteur

Dr M. Liley, rapporteur

Prof. G. Schmid, rapporteur

Prof. H. Vogel, rapporteur

Lausanne, EPFL  
2004



# Abstract

Nanostructured materials can be defined as those materials whose structural elements - clusters, crystallites or molecules - have dimensions in the 1-100 nm range. The explosion in both academic and industrial interest over the past 20 years arises from the remarkable variations in fundamental electrical, optical and magnetic properties that occur as one progresses from an "infinitely extended" solid to a particle of material consisting of a countable number of atoms.

In this work the attention was laid on the optical properties of  $\text{Mn}^{2+}$  doped ZnS nanoparticles with respect to a possible application as bio sensor in medical and biological analytics. A synthesis for this type of particles has been developed and the nanocrystals obtained have been investigated in terms of their composition, particle size and optical properties.

The particles synthesized were stabilized with the amino acid L-cysteine and showed the typical ZnS:Mn emission spectrum with its orange emission due to the  ${}^4\text{T}_1 \rightarrow {}^6\text{A}_1$  transition within the d-orbitals of the  $\text{Mn}^{2+}$  at 585 nm and its blue emission due to recombination over the ZnS band gap from shallow electron traps at 380 nm. The onset of the absorption was blue shifted from 340 nm (bulk) to 310 nm, indicating a quantum size effect.

The particle sizes and particle size distributions were determined with methods such as transmission electron microscopy, photon correlation spectroscopy, analytical ultra centrifugation and field flow fractionation. The particle size has also been calculated from the shift in the band gap with the help of the effective mass approximation. The limits of the applied techniques are discussed and the particle size distribution determined to go from 3-20 nm with a first maximum at about 5 nm and a second maximum at about 17 nm.

The particles' luminescence quantum yields have been determined between 1.5-2 %. They could be enhanced by a factor of three by coating the particles with a  $\text{SiO}_2$  shell. The quantum yields showed a strong dependence on the dispersion concentration and  $\text{Mn}^{2+}$  content. These effects have been investigated with quantum yield measurements at different temperatures and  $\text{Mn}^{2+}$  contents, and lifetime measurements. The lifetime measurements showed decay times in the ns region for the blue and in the  $\mu\text{s}$ -ms region for the orange emission, indicating a fluorescence mechanism for the ZnS and a phosphorescence mechanism for the  $\text{Mn}^{2+}$  radiation.



# Zusammenfassung

Nanostrukturierte Materialien können als die Materialien definiert werden, deren kleinste strukturelle Einheiten - Cluster, Kristallite oder Moleküle - Ausdehnungen im 1-100 nm Bereich haben. Die explosionsartige Zunahme des akademischen als auch des industriellen Interesses in den letzten 20 Jahren, rührt von den aussergewöhnlichen Änderungen der grundlegenden elektrischen, optischen und magnetischen Eigenschaften her, wenn man vom "unendlich ausgedehnten" Feststoff zu einem Material gelangt, das aus einer zählbaren Menge an Atomen besteht.

In dieser Arbeit wurde das Hauptaugenmerk auf die optischen Eigenschaften  $Mn^{2+}$  dotierter ZnS Nanopartikel gelegt, in Hinblick auf eine Anwendung im Bereich der Biosensorik für die medizinische und biologische Analytik. Eine Synthese für diese Partikel wurde entwickelt, und die so erhaltenen Nanokristalle auf ihre Zusammensetzung, Partikelgrösse und optischen Eigenschaften untersucht. Die synthetisierten Partikel wurden mit der Aminosäure L-Cystein stabilisiert und zeigten das typische ZnS:Mn Emissionsspektrum mit seiner orangefarbenen Emission, resultierend aus dem  ${}^4T_1 \rightarrow {}^6A_1$  Übergang in den  $Mn^{2+}$  d-Orbitalen, bei 585 nm, und der blauen ZnS Emission, resultierend aus Rekombinationen über die Bandlücke von leitungsbandnahen Elektronenfallen aus, bei 380 nm. Die Absorptionskante war zu 310 nm blauverschoben im Vergleich zu 340 nm für den ausgedehnten Festkörper, was deutlich auf einen "quantum size" Effekt hindeutet. Partikelgrössen und Partikelgrössenverteilungen wurden mit Methoden wie Transmissionselektronenmikroskopie, Photonenkorrelationsspektroskopie, analytischer Ultrazentrifugation sowie Feldflussfraktionierung bestimmt. Die Partikelgrösse wurde auch aus der Bandlückenverschiebung mit Hilfe der "effective mass" Annäherung bestimmt. Die Grenzen der verwendeten Methoden werden diskutiert und die Partikelgrösse als eine Verteilung von 3-20 nm mit ihrem ersten Maximum bei etwa 5 nm und einem zweiten Maximum bei ca. 17 nm bestimmt. Die gemessenen Quantenausbeuten ergaben 1.5-2 %. Sie konnten um einen Faktor 3 durch Beschichtung mit  $SiO_2$  erhöht werden. Die Quantenausbeuten hingen erheblich von der Konzentration der Dispersionen und dem Mangangehalt ab. Diese Effekte wurden mit Hilfe von Quantenausbeutenmessungen bei unterschiedlichen Temperaturen und Mangangehalten, sowie mit Lebenszeitmessungen untersucht. Die Lebenszeitmessungen ergaben Lebenszeiten im ns Bereich für die blaue und im  $\mu s$ -ms Bereich für die orangefarbene Emission. Dies deutet auf einen Fluoreszenzmechanismus für die ZnS und einen Phosphoreszenzmechanismus für die  $Mn^{2+}$  Emission hin.



## *Remerciements - Danksagungen*

Je tiens à remercier toutes les personnes qui m'ont aidé à réaliser, de près ou de loin, mon travail de thèse et plus particulièrement:

- Le prof. H. Hofmann, directeur du Laboratoire de Technologie des Poudres et directeur de ma thèse. Merci pour ses conseils avisés.
- Alke Fink, la responsable du groupe Nanomatériaux au laboratoire qui fut aussi ma chef et qui restera une amie.
- Paul Bowen, pour ses conseils sur la caractérisation des poudres et sa disponibilité
- Raymond Houriet, pour son aide pour le LINASpark et le IR
- Annie Ferrari, qui fut toujours prête à faire un petit roupillon avec moi à l'ICP
- Sandrine Kobi, pour le travail qu'elle a fourni
- François Perche, mon conseiller informatique
- Ulrich Jäger, für sein offenes Ohr für meine LaTeX Probleme
- Bertrand Pichon, pour l'excellent travail effectué dans le cadre de son projet de semestre
- Catarina Minelli, pour les mesures de durée de vie

A mes collègues du laboratoire, en particulier à Violaine Guérin, la maîtresse du bon français de France, Mathieu Chastellain, le roi des boules en papier, Benedikt Steitz, mein Lieblingspfälzer, et Frédéric Juillerat, le Lance Armstrong de la Suisse.

Meiner Familie für ihre Unterstützung in den letzten acht Jahren.

A tout ceux que je n'ai pas cités....





# Contents

<b>1</b>	<b>Introduction</b>	<b>4</b>
<b>2</b>	<b>Theory</b>	<b>7</b>
2.1	Types of Luminescence . . . . .	7
2.1.1	Photoluminescence . . . . .	7
2.1.2	Fluorescence Lifetimes and Quantum Yields . . . . .	8
2.1.3	Fluorescence quenching . . . . .	10
2.1.4	Quenching and lifetimes . . . . .	12
2.2	Stabilization of Colloidal Systems . . . . .	13
2.2.1	Forces between atoms and molecules . . . . .	13
2.2.2	Forces between particles . . . . .	13
2.2.3	Total interacting potential . . . . .	19
2.3	Semiconductor Quantum Dots . . . . .	20
2.3.1	Quantum size effects . . . . .	21
<b>3</b>	<b>State of the Art</b>	<b>24</b>
3.1	Synthesis of colloidal nanocrystals . . . . .	24
3.1.1	Synthesis of doped ZnS . . . . .	28
3.2	Coating of particles . . . . .	28
3.3	ZnS:Mn nanoparticles . . . . .	31
3.3.1	Fluorescence characteristics and doping . . . . .	31
3.3.2	Lifetime measurements . . . . .	33
3.4	Biological application . . . . .	34
<b>4</b>	<b>Conclusions and goals</b>	<b>36</b>
<b>5</b>	<b>Characterization methods</b>	<b>38</b>
5.1	Fractionating hydrodynamic methods . . . . .	38
5.1.1	Analytical ultra centrifugation . . . . .	38
5.1.2	Field flow fractionation . . . . .	41
5.2	Photon correlation spectroscopy . . . . .	43
5.3	X-ray diffraction . . . . .	44
5.3.1	Size determination . . . . .	45

5.3.2	The Rietveld method . . . . .	46
<b>6</b>	<b>Particle synthesis and properties</b>	<b>47</b>
6.1	Experimental section . . . . .	47
6.1.1	Sample preparation . . . . .	48
6.1.2	Surfactants . . . . .	48
6.1.3	Dispersion stability . . . . .	50
6.1.4	Crystal structure . . . . .	51
6.1.5	Investigation of the precipitate . . . . .	54
6.2	Absorption, excitation and emission spectra . . . . .	57
6.3	Synthesis parameters and particle size . . . . .	60
6.3.1	Stability over time . . . . .	64
6.4	Cysteine adsorption . . . . .	65
6.5	Composition of the particles . . . . .	68
6.6	SiO <sub>2</sub> coated particles . . . . .	73
6.7	Conclusions and discussion . . . . .	75
<b>7</b>	<b>Particle size measurements</b>	<b>77</b>
7.1	Transmission electron microscopy . . . . .	77
7.2	X-ray diffraction . . . . .	79
7.3	Field flow fractionation . . . . .	80
7.4	Photon correlation spectroscopy . . . . .	82
7.5	Analytical ultra centrifugation . . . . .	85
7.6	Optical diameter . . . . .	89
7.7	Conclusions and discussion . . . . .	91
<b>8</b>	<b>Optical properties</b>	<b>95</b>
8.1	Luminescence quantum yield . . . . .	96
8.1.1	Quinine sulphate . . . . .	96
8.1.2	Fluorescence quenching . . . . .	97
8.1.3	Mean free path . . . . .	104
8.1.4	Influence of the SiO <sub>2</sub> shell . . . . .	105
8.1.5	Influence of the doping . . . . .	107
8.2	Luminescence lifetimes . . . . .	110
8.2.1	Flash lamp measurements . . . . .	112
8.2.2	Nanosecond measurements . . . . .	115
8.3	Photo bleaching . . . . .	120
8.4	Doping metals . . . . .	121
8.5	Conclusions and discussion . . . . .	123
<b>9</b>	<b>Final conclusions and discussion</b>	<b>127</b>

<b>A</b>	<b>List of symbols and abbreviation</b>	<b>134</b>
A.1	Symbols . . . . .	134
A.2	Abbreviations . . . . .	137
<b>B</b>	<b>Instrumentation</b>	<b>138</b>
<b>C</b>	<b>Rietveld measurements</b>	<b>141</b>
<b>D</b>	<b>TGA-IR</b>	<b>142</b>
<b>E</b>	<b>Composition</b>	<b>144</b>
E.1	Ethanol isolated powders . . . . .	144
E.2	Freeze dried powders . . . . .	145
<b>F</b>	<b>Particle concentration</b>	<b>147</b>
<b>G</b>	<b>Magnetization measurements</b>	<b>148</b>
<b>H</b>	<b>Bibliography</b>	<b>150</b>

# Chapter 1

## Introduction

Fluorescence is a widely used tool in medical science and biology. It's a powerful technique for studying molecular interactions in analytical chemistry and biology, medicine and environmental science. New developments in instrumentation, software, probes, and applications have resulted in a burst of popularity for a technique that was first observed over 150 years ago.

Fluorescence detection has three major advantages over other light-based investigation methods

- high sensitivity
- high speed
- non-invasive

Sensitivity is an important issue because the fluorescence signal is proportional to the concentration of the substance investigated and relatively small changes in ion concentration in living cells can already have significant physiological effects. Because it is a non-invasive technique, fluorescence does not interfere with a sample. The excitation light wavelength required to generate a fluorescence signal are low for most organic fluorophores and living tissue can be investigated with no damaging effects on its natural physiological behaviour.

As the theoretical underpinnings of fluorescence became more understood, a set of powerful applications such as fluorescence microscopy and fluorescence cell imaging [Uzu03] emerged. Another application of fluorophores are the so called bio assays. These are assays which serve as detection platforms for biomolecules. A biomolecule with a free functional group is attached to its surface and can react selectively with a specific molecule via the "lock-key-principle". If the free molecule was tagged with a fluorophore before reaction with the surface, it can be detected afterwards on the bio assay (see figure 1.1).

The ability to discriminate different colours simultaneously under long-term excitation holds great promise for fluorescent labelling technologies [Bru98, Cha98].

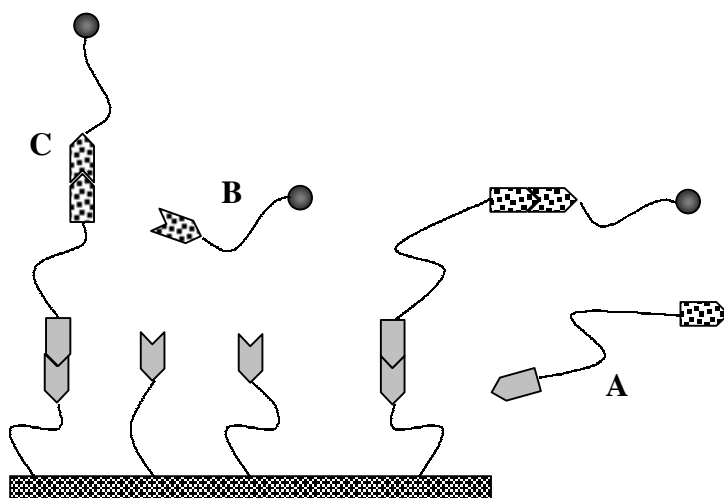


Figure 1.1: Principle of a bio assay, (A) bio molecule to detect, (B) free functionalized nanoparticle, (C) particle and bio molecule attached to the assay

In this respect organic dye molecules suffer from several limiting factors. First their narrow absorption bands make it difficult to excite several colours with a single excitation source. In addition, due to large spectral overlaps of the emissions of dye fluorophores (their emission spectra show a so called "red-tail"), multi-colour experiments require complex mathematical analysis of the data. Second, the emission intensity of organic dyes depend on their environment, and photo bleaching imposes a stringent upper limit on the number of photons detectable per molecule. Photo bleaching is the irreversible destruction of the excited fluorophore under high-intensity illumination conditions which introduces limits for the detectability of the fluorophore. There exist multiple pathways for photo bleaching. Some include reactions between adjacent dye molecules, making the process considerably more complex in labelled biological specimens than in dilute solutions of free dye. In all cases, photo bleaching originates from the triplet excited state, which is created from the singlet state via an excited-state process called intersystem crossing [Son96].

Third, the fast fluorescence emission of the dyes coincides with a high degree to short-lived auto fluorescence background from many naturally occurring species, reducing therefore the signal to noise ratio [Dah01].

Ideal probes for multicolour experiments should emit at spectrally resolvable energies with lifetimes sufficiently long to separate them from the background signal, they should have a narrow, symmetric emission spectrum, and the whole group of probes should be excitable at a single wavelength [Bru98].

This can be achieved with inorganic semiconductor nanocrystals. The unique properties of these so called quantum dots result from quantum confinement,

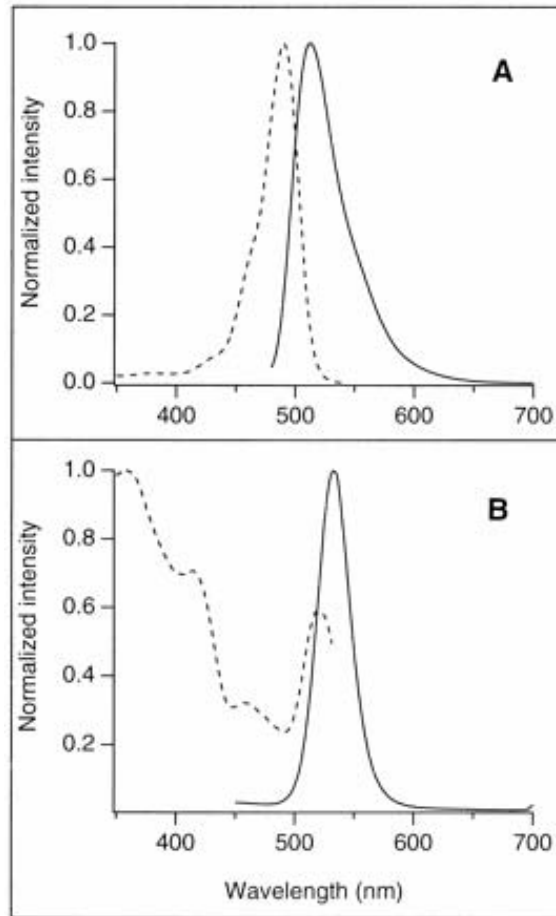


Figure 1.2: Excitation (dashed) and fluorescence (solid) spectra of (A) fluorescein and (B) a typical nanocrystal [Bru98]

which occurs when metal and semiconductor particles get smaller than their exciton Bohr radii (about 1-5 nm) [Cha98]. For semiconductor nanocrystals the energy gap increases with decreasing size. The absorption onset and emission maximum shifts to higher energy with decreasing size. The excitation tracks the absorbance, resulting in a tuneable fluorophore that can be excited efficiently at any wavelength shorter than the emission peak yet will emit with the same characteristic narrow, symmetric spectrum regardless of the excitation wavelength (see figure 1.2). Variation of the material used for the nanocrystal and variation of the size afford a spectral range of 400 nm to 2  $\mu\text{m}$  [Bru98].

These characteristics make QD's ideal probes for multicolour experiments because a whole range of emission wavelengths can be obtained with a single excitation wavelength.

# Chapter 2

## Theory

### 2.1 Types of Luminescence

Luminescence is the general term applied to all forms of cool light, i.e., light emitted by sources other than a hot, incandescent body, such as a black body radiator. It is caused by applying an external source of energy to an atomic or molecular system which undergoes a transition to higher energy levels. In the course of decaying to a lower energy the system subsequently emits optical radiation. Luminescence radiators are classified according to the source of excitation energy, as indicated by the following examples [Pho91].

- **Cathodoluminescence** is caused by accelerated electrons colliding with the atoms of a target.
- **Photoluminescence** is caused by energetic optical photons.
- **Chemiluminescence** provides energy through a chemical reaction.
- **Electroluminescence** results from energy provided by an applied electric field
- **Sonoluminescence** is caused by energy acquired from a sound wave.

#### 2.1.1 Photoluminescence

Photoluminescence occurs when a system is excited to a higher energy level by absorbing a photon, and then spontaneously decays to a lower energy level, emitting a photon in the process. To conserve energy, the emitted photon cannot have more energy than the exciting photon, unless two or more excitation photons act in tandem. Intermediate nonradiative downward transitions are possible. The electron can also be stored in an intermediate state for a long time, resulting in delayed luminescence.

Photoluminescence is divided into two types, depending upon the nature of the ground and the excited states. In a singlet excited state, the electron in the higher-energy orbital has the opposite spin orientation as the second electron in the lower orbital. These two electrons are said to be paired. In a triplet state these electrons are unpaired, that is, their spins have the same orientation. Return to the ground state from an excited singlet state does not require an electron to change its spin orientation. A change of spin orientation is needed for a triplet state to return to the singlet ground state (see figure 2.1). **Fluorescence** is the emission which results from the return to the lower orbital of the paired electron. Such transitions are quantum mechanically "allowed" and the emissive rates are typically near  $10^8 \text{ s}^{-1}$ . These high emissive rates result in fluorescence lifetimes near  $10^{-8} \text{ s}$  or 10 ns. The lifetime is the average period of time a fluorophore remains in the excited state. **Phosphorescence** is the emission which results from transition between states of different multiplicity, generally a triplet excited state returning to a singlet ground state. Such transitions are not allowed and the emissive rates are slow. Typical phosphorescent lifetimes range from milliseconds to seconds, depending primarily upon the importance of deactivation processes other than emission [Lak83].

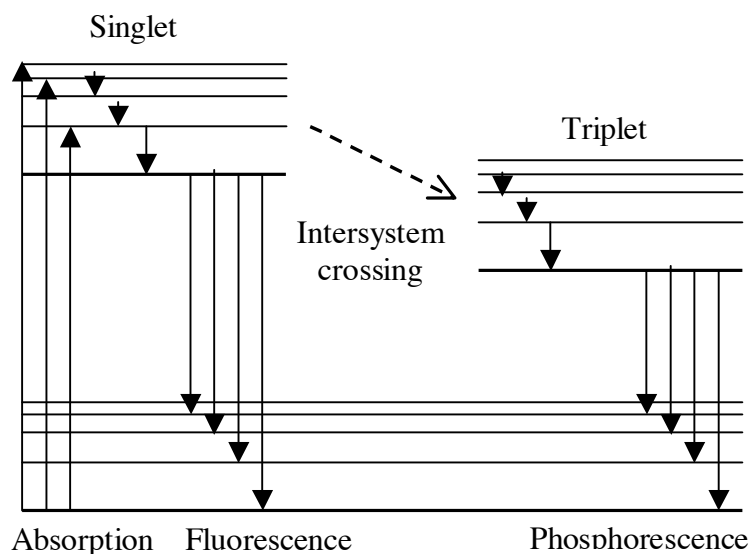


Figure 2.1: Fluorescence and phosphorescence mechanism

### 2.1.2 Fluorescence Lifetimes and Quantum Yields

The fluorescence lifetimes and quantum yields of fluorescent substances are frequently measured. The meaning of these parameters are best illustrated by reference to a modified Jablonski diagram (see figure 2.2). In this diagram the individual relaxation processes leading to the relaxed  $S_1$  state are not explicitly



illustrated. Instead attention to those processes responsible for return to the ground state is increased. Of special interest is the emissive rate of the fluorophore ( $\Gamma$ ) and its rate of radiationless decay to  $S_0$  ( $k$ ).

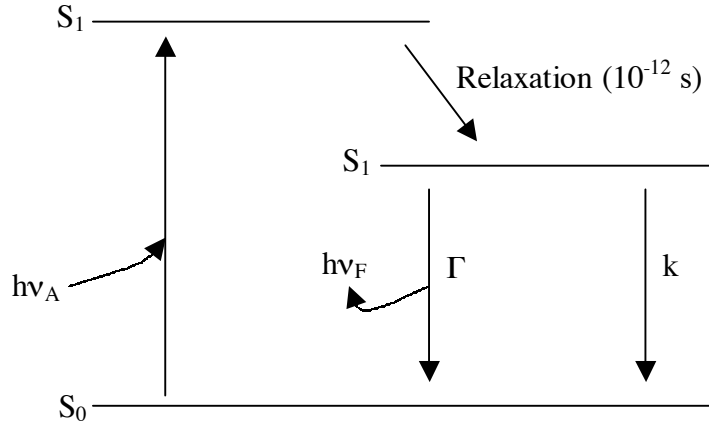


Figure 2.2: Modified Jablonski diagram after reference [Lak83]

The fluorescence quantum yield is the ratio of the number of photons emitted to the number absorbed. The rate constants  $\Gamma$  and  $k$  both depopulate the excited state. The fraction of fluorophores that decays through emission, and hence the quantum yield, is given by

$$\Phi = \frac{\Gamma}{\Gamma + k} \quad (2.1)$$

The quantum yield can be close to unity if the radiationless rate of deactivation is much smaller than the rate of radiative decay, that is  $k \ll \Gamma$ . The lifetime  $\tau$  of the excited state is defined by the average time the molecule spends in the excited state prior to return to the ground state.

$$\tau = \frac{1}{\Gamma + k} \quad (2.2)$$

The lifetime of the fluorophore in the absence of nonradiative processes is called intrinsic lifetime  $\tau_0$ , and is given by

$$\tau_0 = \frac{1}{\Gamma} \quad (2.3)$$

This leads to the familiar relationship between the quantum yield and the lifetime

$$\Phi = \frac{\tau}{\tau_0} \quad (2.4)$$

The quantum yield and lifetime can be modified by any factors which affect either of the rate constants. For example, a molecule may be nonfluorescent as a result of a large rate of internal conversion or a slow rate of emission [Lak83]. Because it is difficult to determine absolute quantum yields, relative methods are often used which compare the sample with a compound of known quantum yield. The determination of quantum yields using optically dilute solutions is the most common method currently employed. These measurements rest on Beer's law and a spectrofluorimeter is used as the detector. Absorbance of sample and reference must be similar and it is preferable that they are in the same solvent. If this is not possible, then correction for the differences in the refractive indices of the solvents must be made. The need for the refractive index correction arises from two sources. As radiation passes from the solution to air (i.e., from high to low index region), its intensity changes because of the refraction. Second, internal reflection within the measure cell can occur [Mee83].

When this is taken into account the sample quantum yield  $\Phi_S$  can be calculated with equation 2.5 [Dem71], where A is the absorbance, E the integral over the emission peak and n the refractive index. The indices S and R always indicating sample and reference.

$$\Phi_S = \frac{A_R \cdot E_S \cdot n_S^2}{A_S \cdot E_R \cdot n_R^2} \cdot \Phi_R \quad (2.5)$$

### 2.1.3 Fluorescence quenching

Fluorescence quenching refers to any process which decreases the fluorescence intensity of a given substance. A variety of processes can result in quenching. This includes excited state reactions, energy transfer, complex formation (static quenching) or collisional quenching (dynamic quenching). In the following we will only consider dynamic and static quenching. For static quenching the fluorophore and its quencher form a nonfluorescent complex, for dynamic quenching the fluorophore returns to the ground state without emission of a photon on contact with the quencher.

#### Dynamic quenching

Collisional quenching of fluorescence is described by the Stern-Volmer equation:

$$\frac{F_0}{F} = 1 + k_q \tau_0 [Q] = 1 + K_D [Q] \quad (2.6)$$

In this equation  $F_0$  and  $F$  are the fluorescence intensities in the absence and the presence of a quencher, respectively,  $k_q$  is the bimolecular quenching constant,  $\tau_0$  the lifetime of the fluorophore in the absence of the quencher,  $[Q]$  is the concentration of the quencher, and  $K_D$  is the Stern-Volmer quenching constant. It is useful to note that  $K_D^{-1}$  is the quencher concentration at which  $F_0/F=2$  or

50 % of the intensity is quenched. A linear Stern-Volmer plot ( $F_0/F \rightarrow [Q]$ ) is generally indicative of a single class of fluorophores, all equally accessible to the quencher.

To see the diffusion dependency of the dynamic quenching one has to look at the collisional frequency  $Z$  of a fluorophore and its quencher that is given by

$$Z = k_0 \cdot [Q] \quad (2.7)$$

where  $k_0$  is the diffusion-controlled bimolecular rate constant.  $k_0$  is dependant of the diffusion coefficient by the Smoluchowski equation:

$$k_0 = \frac{4\pi RDN_A}{1000} = \frac{4\pi N_A}{1000}(R_f + R_q)(D_f + D_q) \quad (2.8)$$

where  $R$  is the collision radius,  $D$  is the sum of the diffusion coefficients of the fluorophore ( $D_f$ ) and the quencher ( $D_q$ ),  $N_A$  is Avogadro's number. The collision radius is generally assumed to be the sum of the molecular radii of the fluorophore ( $R_f$ ) and the quencher ( $R_q$ ). The equation describes the diffusive flux of a molecule with a diffusion coefficient  $D$  through the surface of a sphere with the radius  $R$ . The factor 1000 is necessary to keep the units correct when the concentration is expressed in terms of molarities. The term  $N_A/1000$  converts molarities to molecules /cm<sup>3</sup> [Lak83]. So if  $R_f$  and  $R_q$  are given in cm, the unit of  $k_0$  is [ $\frac{1}{s}$ ].

### Static quenching

Static quenching occurs as a result of the formation of a nonfluorescent ground state complex between the fluorophore and the quencher. When this complex absorbs light it immediately returns to the ground state without emission of a photon. The dependence of the fluorescence intensity upon quencher concentration is easily derived by consideration of the association constant  $K_s$  of the complex formation. This constant is given by

$$K_s = \frac{[F - Q]}{[F][Q]} \quad (2.9)$$

where  $[F - Q]$  is the concentration of the complex and  $[F]$  the concentration of the uncomplexed fluorophore. If the complexed species is nonfluorescent then the fraction of the fluorescence which remains is ( $F/F_0$ ) is given by the fraction of the total fluorophore which is not complexed ( $f$ ). That is,  $f = F/F_0$ . Recalling that the total concentration of fluorophore  $[F_0]$  is given by

$$[F]_0 = [F] + [F - Q] \quad (2.10)$$

substitution in equation 2.9 yields

$$K_s = \frac{[F]_0 - [F]}{[F][Q]} = \frac{[F]_0}{[F][Q]} - \frac{1}{[Q]} \quad (2.11)$$

We can substitute the fluorophore concentrations with the fluorescence intensities, and rearrangement of 2.11 yields

$$\frac{F_0}{F} = 1 + K_s \cdot [Q] \quad (2.12)$$

Observe that the dependence of  $F/F_0$  on  $[Q]$  is identical to what was observed for the dynamic quenching, except that the quenching constant is now the association constant. Fluorescence quenching data, obtained by intensity measurements alone, can be explained by either dynamic or static processes unless additional information is provided. Measurements at different viscosities or temperatures (see section 8.1.2) can be used to distinguish between static and dynamic quenching another possibility is the changes in lifetimes [Lak83].

### 2.1.4 Quenching and lifetimes

Lifetime measurements can give additional information that help to distinguish between collisional and static quenching. Collisional quenching is a additional process which depopulates the excited state of the fluorophore and influences therefore the lifetimes as described in section 2.1.2.

The lifetimes in absence ( $\tau_0$ ) and presence ( $\tau$ ) of quencher are given by

$$\tau_0 = \frac{1}{\Gamma} \quad (2.13)$$

and

$$\tau = \frac{1}{(\Gamma + k_q \cdot \tau_0)} \quad (2.14)$$

and therefore

$$\frac{\tau_0}{\tau} = 1 + k_q \tau_0 \cdot [Q] \quad (2.15)$$

This latter deviation corresponds to equation 2.6 and illustrates an important characteristic of collisional quenching, which is an equivalent decrease in fluorescence intensity and lifetime.

$$\frac{F_0}{F} = \frac{\tau_0}{\tau} \quad (2.16)$$

The decrease in lifetime occurs because quenching is an additional process which depopulates the excited state. The decrease in yield occurs because the quenching depopulates the excited state without fluorescence emission.

Static quenching removes a fraction of the fluorophores from observation. The complexed fluorophores are nonfluorescent and the only observed fluorescence is from the uncomplexed fluorophore. The uncomplexed fraction is unperturbed, and hence the lifetime is  $\tau_0$ . Therefore, for static quenching  $\tau_0/\tau = 1$  (see figure 8.3).

## 2.2 Stabilization of Colloidal Systems

It is commonly accepted that the stability of colloidal systems is, in most cases, the result of an extremely slow aggregation process. The main reason for such a slow aggregation is a high electrostatic energy barrier and in some cases a protective layer of a surfactant [Kal02].

### 2.2.1 Forces between atoms and molecules

Since the work of van der Waals in 1873 it is known that there exist attractive forces between non polar molecules. London showed in 1930 that these attractive forces are due to fluctuating dipoles resulting from the movement of the electrons within the electron cloud of the atoms. He calculated the free attractive energy  $\Delta G^{att}$  between two atoms or molecules to be

$$\Delta G^{att} = -\frac{A}{d_{aa}^6} \quad (2.17)$$

where A is a molecule or atom specific constant and  $d_{aa}$  the distance between two atoms or molecules.

When the atoms get below a certain distance their electron clouds begin to interact, which creates repulsive forces and lead to an increase of  $\Delta G^{att}$ . This free repulsive energy  $\Delta G^{rep}$  can be expressed with the following equation

$$\Delta G^{rep} = \frac{B}{d_{aa}^{12}} \quad (2.18)$$

where B is as A a molecule or atom specific constant.

The sum of these interactions is the so called *Lennard-Jones-Potential*  $\Delta G_{LJ}$  [Eve92].

$$\Delta G_{LJ} = \Delta G^{rep} + \Delta G^{att} = \frac{B}{d_{aa}^{12}} + \frac{A}{d_{aa}^6} \quad (2.19)$$

### 2.2.2 Forces between particles

To calculate the attractive forces between two particles one assumes that every atom of one particle interacts with every atom of the other particle following the Lennard-Jones-Potential, and that the free energy of these interactions is the sum

over the contribution of all possible atom pairs. Since the repulsive forces are of short range, only the surface atoms are taken into account.

The easiest way to solve this problem is to calculate it for two infinite surfaces separated by a distance  $H$ , which was done by Hamaker and leads to

$$\Delta G^{att} = -\frac{A_H}{12\pi H^2} \quad (2.20)$$

for the free energy between the surfaces with  $A_H$  being the so called Hamaker constant. A similar approach for two spheres of the same radius  $r$  leads to

$$\Delta G^{att} = -\frac{A_H r}{12H^2} \left[ 1 + \frac{3H}{4r} + \dots \right] \quad (2.21)$$

where  $H$  now represents the distance between the centres of the two spheres. The higher terms can be neglected for most cases.

Equation 2.20 and 2.21 show clearly that for bigger particles the attractive forces decrease considerably slower than for single molecules and atoms which has a significant influence on the stability of particle dispersions [Eve92].

### Electrostatic Stabilization

Particles in aqueous dispersion normally show a surface charge that can be due to the ionization of surface groups or to the adsorption of charged molecules or simply ions.

Following Coulomb's law every charge creates an electric potential that will be compensated by charges of opposite sign in its proximity. That means that around every negatively charged ion an excess of positive charges will be present and vice versa. This cloud of counter ions is called electric double layer.

The concept of double layer was first introduced by Helmholtz. He imagined it as a molecular condensator in which the potential decreases linearly. But thermal movement leads to a distribution of the counter ions, so that a diffuse double layer is formed (Gouy and Chapman 1913). This double layer results in a Coulombic repulsion between two particles which decays approximately exponentially with the interparticle distance  $z$  (see equation 2.22).

$$\psi = \psi^0 e^{-\frac{\kappa}{z}} \quad (2.22)$$

The net result is shown schematically in figure 2.3. The weak minimum in the potential energy at moderate interparticle distances defines a stable arrangement for the colloidal particles which is easily disrupted by medium effects, and at room temperature, by the thermal motion of the particles. Thus, if the electric potential associated with the double layer is sufficiently high, then electrostatic repulsion will prevent particle agglomeration.

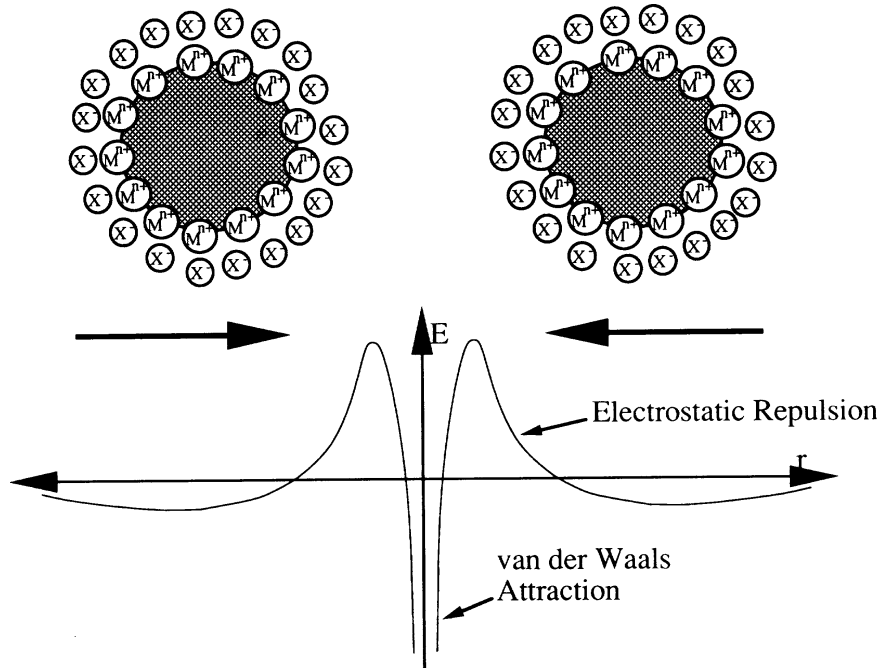


Figure 2.3: Electrostatic stabilization of colloidal particles. Attractive van der Waals forces are outweighed by repulsive electrostatic forces between adsorbed ions and associated counterions at moderate interparticle separation [Sch94].

According to the Debye-Hückel-theory for electrolytes the thickness of the double layer is defined by

$$\frac{1}{\kappa} = \sqrt{\frac{\varepsilon_r \varepsilon_0 k_B T}{2N_A e^2 I}}. \quad (2.23)$$

with  $\varepsilon_r$  and  $\varepsilon_0$  being the electric permittivity of the medium and the vacuum,  $k_B$  Boltzmann's constants,  $N_A$  Avogadro's constant,  $T$  the temperature,  $e$  the elementary charge and  $I$  the ionic strength.

In equation 2.23 one can see that the thickness of the double layer depends strongly on the ionic strength in the solution. This shows that an electrostatically stabilized sol can be coagulated if the ionic strength of the dispersing medium is increased sufficiently, since this compresses the double layer and shortens the range of the repulsion [Sch94].

At long distances two particles will not "see" one another because of their neutralizing double layers. When they get closer these double layers act like the electron clouds around an atom. When the two double layers are charged in the same way they will repel one another [Eve92, Wed97]. This is the basis of the DVLO theory. The DVLO theory takes only two interactive energies into account, the

van-der-Waal attraction (see equation 2.20) and the repulsive potential due to the overlapping of the double layers. When the double layers of two charged surfaces overlap their electric potentials add up. This results in an increase of the electric Gibbs energy  $\Delta G_{elst}$ :

$$\Delta G_{elst} = \frac{64c_0k_B T}{\kappa} e^{-\kappa H} \quad (2.24)$$

with  $c_0$  being the ion concentration without potential. This concentration dependence mainly comes from the dependence of the double layer thickness  $\frac{1}{\kappa}$  on the ionic strength.

Added with the term for the van-der-Waals attraction we get an expression for the potential interactive energy  $\Delta G_{pot}$  between two flat surfaces per surface unit:

$$\Delta G_{pot} = \frac{64c_0k_B T}{\kappa} \cdot e^{-\kappa H} - \frac{A_H}{12\pi H^2} \quad (2.25)$$

The stabilizing effect of surface ions is not only dependent on the concentration of the ions in solution, but also on the concentration of ions adsorbed at the particle surface. If the surface charge is reduced by the displacement of adsorbed ions by a more strongly binding neutral adsorbate, the colloidal particles can collide and agglomerate under the influence of the van der Waals attractive forces.

### Steric Stabilization

Colloidal dispersions can also be stabilized by the addition of a surfactant that is in most cases a polymer. The surfactant forms a protecting layer around the particle and so prevents flocculation. The adsorbed layers can influence the van der Waals attractions or induce repulsion of the particles. This is called steric stabilization. We have to distinguish between three cases:

**Anchored polymers** In the case of a compact adsorbed layer the particles can be regarded as a hard sphere with the diameter  $2(r + \delta)$ , where  $r$  is the particle radius and  $\delta$  the thickness of the adsorbed layer. So this adsorbed layer prevents that the centres of the particles can get closer than  $2(r + \delta)$ .

When the protective layer resembles the dispersing medium, the attraction between the particles for a distance  $H$  without contact will not be influenced by the adsorbed layer. But since the particles can not get closer than  $2(r + \delta)$  on contact, the attractive potential on contact will be smaller than for particles without protective layers.

On the other hand, when the layer resembles the particle material, it will act like a bigger particle and so result in a higher attractive potential than a not coated particle (see equation 2.21).

But normally the adsorbed polymer does not act like a hard surface. The polymer chains will extend into the dispersing medium in a degree that depends on



the interaction between polymer and dispersing medium.

The more the surfactant resembles the dispersing medium the more the polymer chains will be directed outward into the solvent. When two particles collide the surfactant or polymer chains will penetrate one another. This has two consequences:

First, the local density of the polymer will be increased so that the osmotic effect will cause a diffusion of solvent molecules between the two surfaces to diminish the surfactant concentration. This will push apart the particles.

Second, the higher surfactant concentration between the particles will lead to a reduced number of possible arrangements of the chains. So the entropy decreases by a value  $\Delta S$  and so the free repulsive energy increases by  $|T\Delta S|$ . This is called entropic repulsion. In this case the polymer chains of one layer penetrate in the layer of another particle, so the center-center distance of the particles can be smaller than  $2(r + \delta)$ , but the repulsive potential increases strongly. So to achieve a good steric stabilization the surfactant should be different from the nature of the particle but similar to the one of the dispersing agent. The longer the chain length the better the stabilization, because the repulsive strength depends strongly on the thickness of the surfactant layer around the particle. The surfactant can be attached to the surface by chemical bonding or by a strong and specific binding [Eve92, Rus89].

**Non adsorbing polymers** Dissolved, non-adsorbing polymer molecules must alter their configuration if their centre of mass is to approach a particle surface. This leads to the formation of a so called depletion layer around each particle. That means a layer from which the polymer is excluded.

A particle immersed in a polymer solution experiences an osmotic pressure acting normal to its surface. For an isolated particle, the integral of the pressure over the entire surface nets zero force. But when the depletion layers of two particles overlap, polymer will be excluded from a portion of the gap between the particles. Consequently, the pressure due to the polymer becomes unbalanced. The polymer concentration between the particles is lower than in the volume, so the dispersing agent diffuses in the volume leading to an attractive force and particle flocculation. This is called *depletion flocculation* [Eve92, Rus89].

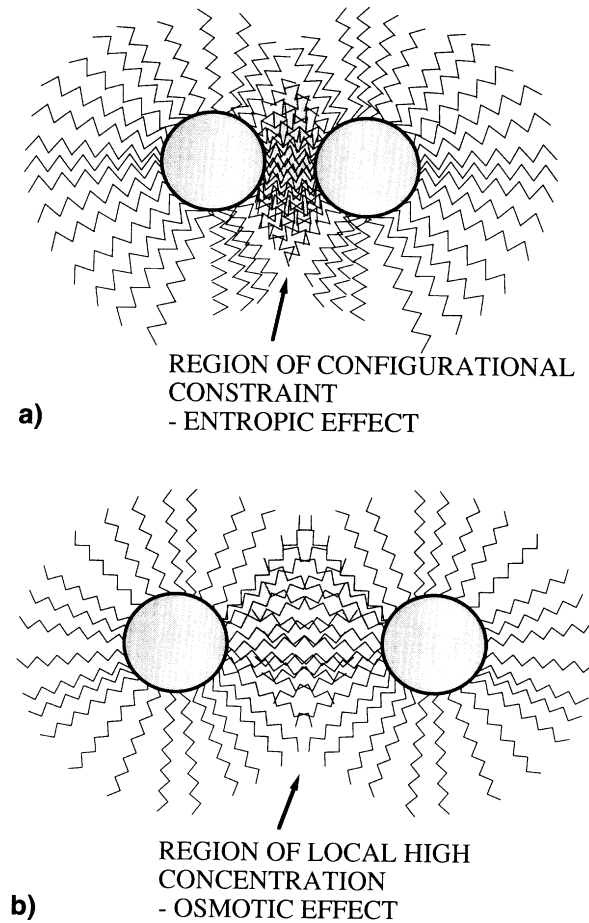


Figure 2.4: Steric stabilization of colloidal particles with anchored polymers: **a)** in the interparticle space the configurational freedom of the polymer chains of two approaching particles is restricted causing a lowering of entropy; **b)** the local concentration of polymer chains between the approaching particles is raised and the resulting higher local activity is osmotically counteracted by solvation [Sch94].

**Adsorbing polymers** Thus far, we have considered only the extremes of irreversibly anchored and non adsorbing polymers. More commonly, though, polymers adsorb at random points along their backbone to a degree that depends on the nature of the polymer, the solvent and the surface. The interactions between surfaces is more complicated with adsorbed polymer layers than with terminally anchored chains for two reasons:

1. Chains originally attached to one surface can adsorb at the same time to the surface of a second particle to create a bridging between two particles.

2. Given enough time, chains can desorb from the surface and migrate out of the gap between two particles.

With strong adsorption at full coverage of the particles surface in a good solvent the produced potential between two particles is purely repulsive. The polymer layers interact at separations somewhat greater than twice the end-to-end distance of the free chains. Since the coverage of the surface is approximately full there is no significant bridging.

With strong adsorption but only partial coverage, the situation differs considerably. Then the layers interpenetrate more easily and excess surface is available for adsorption of tails from the opposing layer leading to attraction via bridging of the particles. But still the potential stays repulsive at small separations, demonstrating that strongly adsorbed polymers do not desorb and migrate out of the gap between the particles.

With still weaker adsorption and a solvent only slightly better than a theta solvent, even interaction at full coverage produces attraction. But there is still a repulsion at very small separations indicating that complete desorption of the polymer from the surface does not occur [Rus89].

### 2.2.3 Total interacting potential

One gets the general equation for the change of the free energy  $\Delta G$  for two approaching particles from an infinite distance to a distance  $H$  by addition of the discussed contributions.

Normally not all these effects are simultaneously present in a sample, so we show in figure 2.5 the total free interacting potential for electrostatically and sterically stabilized system separately. In figure 2.5 (a) the graphs i-iii represent increasing electrolyte concentration. So one can clearly see that the repulsion due to the double layer depends strongly on the ionic strength of the medium. At low ionic strength one observe a higher energy barrier, at medium ionic strength there is often a secondary minimum accompanying a lower energy barrier and for high ionic strengths this barrier completely vanishes.

In the same way the steric repulsion is influenced by the thickness of the adsorbed polymer layer. In figure 2.5 (b) the potential curves i-iii for decreasing layer thickness  $\delta$  by constant polymer density can be seen. The thicker the adsorbed polymer layer, the greater the distances at which repulsion occurs [Eve92, Eva99].

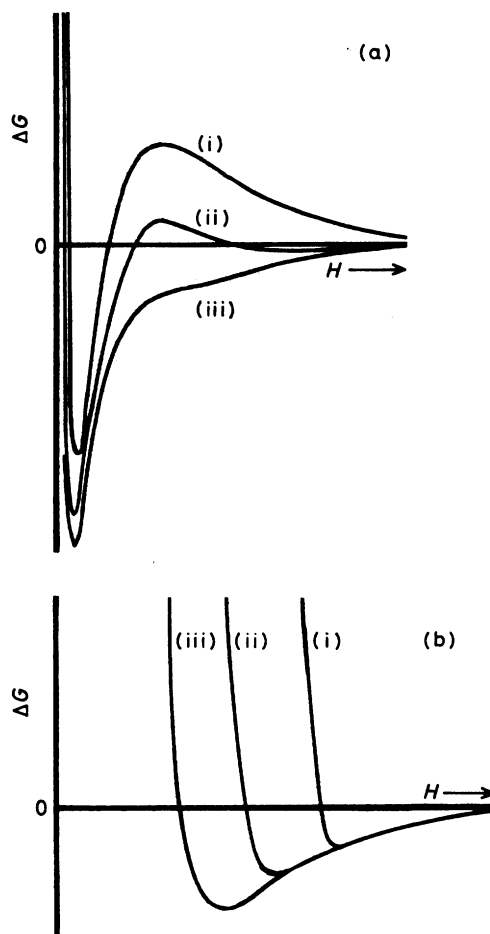


Figure 2.5: Potential curves for (a) electrostatic and (b) steric stabilized particles. i-iii indicating different ionic strength for (a) and different layer thickness for (b)

## 2.3 Semiconductor Quantum Dots

The explosion in both academic and industrial interest in nanostructured materials over the past 15 years arises from the remarkable variations in fundamental electrical, optical and magnetic properties that occur when one passes from an infinitely extended solid to a particle of material consisting of a countable number of atoms. For semiconductor nanoparticles Brus [Ros83, Ros84] was one of the first that ascribed the changes in band gap with the so called quantum size effects.

### 2.3.1 Quantum size effects

The band gap of a semiconductor is defined as the difference between the highest energy level of the valence band and the lowest energy level of the conduction band [Lip89]. When a semiconductor is excited by a photon with sufficient energy two quasiparticles are created. A hole  $h^+$  with the mass  $m_h^*$  and a positive charge  $+e$  and an electron  $e^-$  with the mass  $m_e^*$  and the negative charge  $-e$ . The concept of quasiparticles is used in theory to replace a consideration of a large number of interacting particles by a small number of *non interacting* quasiparticles. These quasiparticles are described as elementary excitations of a system of a number of real particles. In our case the electron in the conduction band represents the primary elementary excitation of the electron subsystem of the crystal. The hole represents an ensemble of electrons in the valence band from which one electron was removed (e.g. to the conduction band). In reality, the electron and the hole as charged particles do interact via the Coulomb potential and form a third quasiparticle the so called exciton, which corresponds to a hydrogen-like bound state of an electron-hole pair and is therefore characterized by the exciton Bohr radius  $a_B$  [Gap98]:

$$a_B = \frac{4\pi\epsilon_0\epsilon_r\hbar^2}{e^2} \cdot \left( \frac{1}{m_e^*} + \frac{1}{m_h^*} \right) \quad (2.26)$$

The exciton Bohr radius is considerably larger than the respective value for a hydrogen atom because the values for the effective masses for the electron and the hole are smaller than the effective mass of the electron at rest  $m_0$ , and the dielectric constant  $\epsilon$  in a semiconductor several times larger than 1 which is the value for vacuum. Typical values for  $a_B$  for common semiconductors range in the interval from 1-10 nm. As a result of the creation of an exciton and a free e-h pair, the absorption spectrum of direct band gap semiconductor monocrystals contains a pronounced resonance peak at the energy

$$h\nu = E_g - Ry^* \quad (2.27)$$

with  $\nu$  the frequency and the Rydberg energy being

$$Ry^* = \frac{e^2}{2\epsilon a_B} \quad (2.28)$$

when the Rydberg energy is smaller than  $kT$  ( $kT \ll Ry^*$ ). When the radius of a particle approaches  $a_B$  the exciton in the particles experience a spatial confinement and can only exist in the particle when it is in a state of higher energy which leads to an increase in the energy gap of the semiconductor. As a result of such a quantum confinement an exciton in a nanocrystal has to be considered as a particle in a box, so its kinetic energy becomes quantized and the energy bands split into discrete levels. This is the origin of the name quantum dots for such

particles [Gap98].

This quantum confinement can be explained by two approaches, first with the effective mass approximation [Bru84], second with the tight binding model [Baw90].

### Effective Mass Approximation

The effective mass approximation calculates the size dependence of the band gap quantum mechanically with the particle in a box approach and uses the effective masses of electron and hole in the term for the kinetic energy, which leads to the following result [Lip89]:

$$E = E_g + \frac{\pi^2 \hbar^2}{2m_0 r^2} \cdot \left( \frac{1}{m_e^*} + \frac{1}{m_h^*} \right) - \frac{1.8e^2}{4\pi\epsilon_0\epsilon_r r} - 0.25 \cdot \frac{e^4}{8\pi^2\epsilon_0^2\epsilon_r^2\hbar} \left( \frac{1}{m_e^*} + \frac{1}{m_h^*} \right) \quad (2.29)$$

The first term is the bulk band gap energy, the second the kinetic energy of both the electron and the hole in a spherical box, the third term is their Coulomb attraction and the last one corresponds to the correlation between two particles. When  $r$  tends to high values  $E$  approaches  $E_g$ .

However, this approach fails for the smallest crystallite sizes because of the oversimplified description of the crystal potential as a spherical well with an infinitely high potential at the interface [Lip89]. Another problem could be the fact that the effective masses were assumed to be constant which is only correct when dealing with electronic states near the band edges [Hen89]. In fact it was shown in a study of PbS that the effective masses increase with decreasing particle size [Wan87].

### The tight binding Model

Nanometer sized semiconductor crystallites, if treated correctly, should be described in the same way as very large molecules. That means that the particular number of atoms and their spatial configuration should be regarded rather than the size.

In II-VI zinc blende crystals such as ZnS, each Zn atom is surrounded tetrahedrally by four S atoms and vice versa. With three p and one s atomic orbital on each cation and anion, we will obtain four  $sp^3$ -hybridized atomic orbitals. When these atoms assemble in a cluster these orbitals should be treated as a set of bond, rather than atomic, orbitals between nearest neighbour atoms. They so form a set of bonding orbitals  $\sigma$  and a set of antibonding orbitals  $\sigma^*$  [Baw90]. As the number of atoms in the crystallite grows, each of the localized bond orbital sets form molecular orbitals extended over the crystallite that finally develop into conduction and valence bands. The highest occupied molecular orbital (HOMO) becomes the top of the valence band, and the lowest unoccupied molecular orbital (LUMO) becomes the bottom of the conduction band. The HOMO-LUMO

spacing tends to the band gap energy of the bulk nanocrystals. In figure 2.6 it can be seen that with decreasing number of atoms in the particle the band gap increases and we obtain discrete energy levels [Wan87].

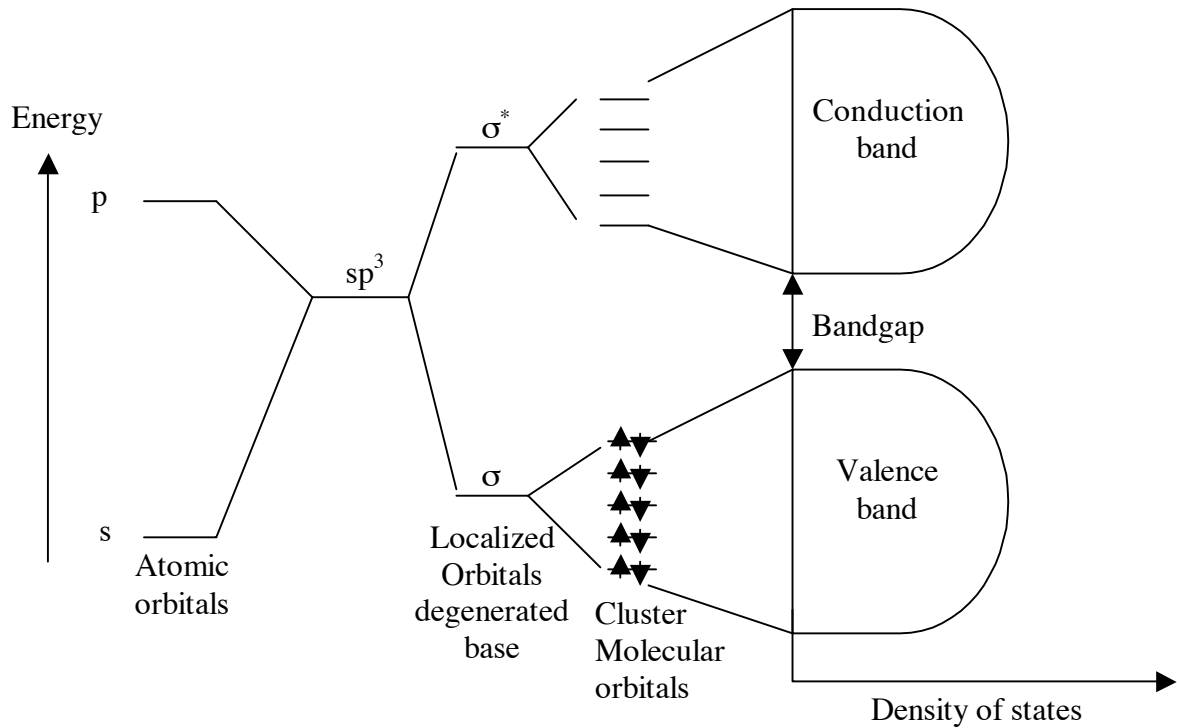


Figure 2.6: Evolution from molecular orbitals into bands after reference [Baw90]

With the tight binding model the electronic structure for very small crystallites can be calculated using quantum mechanical methods [Gap98], but it is not possible to calculate the energy levels for big clusters [Lip89], because too many atoms have to be taken into account.

# Chapter 3

## State of the Art

### 3.1 Synthesis of colloidal nanocrystals

The first to demonstrate that the blue shift in semiconductor absorption spectra is related with a widening of the band gap was the group of Brus at Bell Laboratories in 1983 [Ros83]. For this ZnS and CdS dispersions were prepared by precipitation at different temperatures with Na<sub>2</sub>S either in methanol or in water [Ros85] at low concentrations. Cd(ClO<sub>4</sub>)<sub>2</sub> and Zn(ClO<sub>4</sub>)<sub>2</sub> were used as Zn<sup>2+</sup> and Cd<sup>2+</sup> precursors. This led to an explosion in synthesis of semiconductor nanoparticles with different methods. Structured reaction media showed to improve size control and stabilization of the particles so synthesis with different surfactants were developed. Fendler and colleagues discovered that CdS particles in the nanometre sized water pools of inverse micelles were unusually stable against flocculation [Fen87]. Herron, Wang and co workers [Wan87/2] reported the use of small zeolite cavities as hosts for (CdS)<sub>4</sub> clusters. In this synthesis it was not possible to recover the clusters and redisperse them. However, Henglein, Weller, and co-workers used polymeric sodiumhexametaphosphat to protect the surface of the otherwise bare particles. The coated particles could be recovered after precipitation as a powder and, importantly, were then redispersible in water [Foj84]. To get a narrow size distribution the particles were redispersed in water and size separation was achieved by exclusion chromatography [Fis86], [Fis89]. Transfer of the inorganic particles into organic medium was first made by Brus *et al* ([Ste88], [Ste90]). By treating micelle-encapsulated CdSe particles, having a Cd<sup>2+</sup> rich surface, with phenyl(trimethylsilyl)selenium (PhSeTMS), the particles were covalently coated with Ph-Se<sup>-</sup> and could be isolated as powders and redispersed in organic solvents. The organic group at the surface showed little effect on the HOMO-LUMO absorption and could be varied to obtain changes in the physical properties such as solubility. The solubility of the passivated molecular particles allowed their purification and subsequent study. It was also possible to nucleate and grow CdSe particles on seeds of ZnS, and vice versa, in inverse



micelle media [Kor90].

A breakthrough in nanoparticle synthesis came in the 90's when two strategies of nanoparticle synthesis have been developed working with TOPO (n-triethylphosphine oxide) to stabilize the particles. In the first case developed by the group of Bawendi in 1993, nucleation and growth were allowed to take place over an extended period of time at a moderate temperature (180-300 °C), yielding a wide range of sizes [Mur93]. For this selenium or tellurium salts were directly dissolved in TOP (n-octylphosphine), mixed with a solution of dimethylcadmium ( $\text{Me}_2\text{Cd}$ ) and were then injected into hot TOPO at 300°C. The rapid introduction of the reaction mixture into the hot TOPO produced a deep yellow/orange colour and a sudden decrease in temperature to  $\sim 180$  °C. After the addition of the reaction mixture the temperature of the TOPO was gradually raised to 230-260 °C. The temperature was lowered in response to a spreading in size distribution and increased when growth appeared to stop. When the desired UV/vis - absorption characteristics were obtained a sample was taken. In this way, a series of sizes ranging from  $\sim 1.5$  to 11.5 nm could be obtained. The still rather broad particle size distribution could be sorted out by selective size precipitation were to a particle dispersion in 1-butanol, methanol was added leading to precipitation with the biggest particles precipitating first.

The second approach developed by Alivisatos *et al* uses the synthesis described above, but separates nucleation from growth by injecting the reaction mixture rapidly at higher temperatures (350 °C) into the TOPO to induce nucleation and then reducing the temperature during the growth phase, yielding particles of nearly one size [Kat94]. Nucleation occurs rapidly, followed by growth. At the growth temperature, surfactant molecules adsorb and desorb rapidly from the nanocrystal surface, enabling the addition as well as removal of atoms from the crystallites, while aggregation is suppressed by the presence of the surfactant at the crystallite surface. During the focusing of the size distribution, the concentration of the precursors in solution is higher than the solubility of all the particles present, a situation in which all the particles grow, regardless of their size. At high precursor concentration, the smaller particles grow faster than the larger ones, and as a result, the size distribution can be focused down to one that is nearly monodisperse.

If the precursor concentration drops below a critical threshold, small nanocrystals are depleted as larger ones grow and the distribution broadens, or defocuses. The desired size of the nanocrystals can be adjusted by changing the amount of injected precursors and the time they are grown in the hot TOPO. The nanocrystals obtained in this way are hydrophobic, since they are covered with a surfactant layer. This layer of TOPO molecules stabilizes the nanocrystals in solvents like toluene or chloroform and prevents agglomeration. According to the size of the synthesized nanocrystals, fluorescence in practically all colours of the visible spectrum can be obtained [Par03] [Pen98].

Even though all sorts of semiconductor nanocrystals (ZnS, ZnSe, GaAs, InAs,

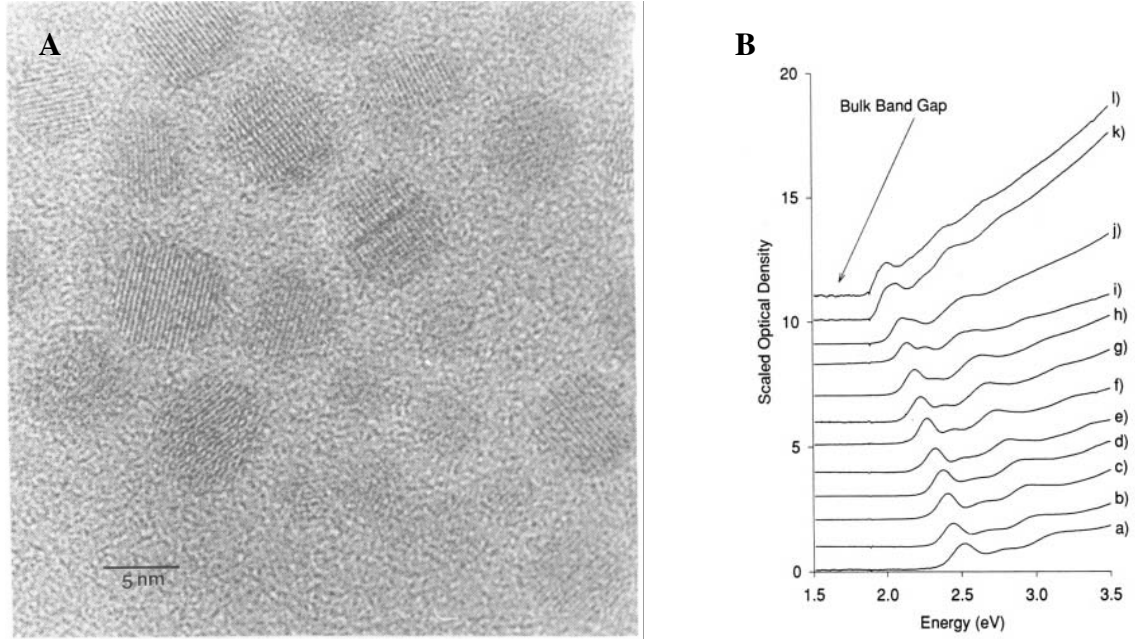


Figure 3.1: **(A)** Transmission electron micrograph of CdSe nanocrystals, **(B)** Uv-vis absorption spectra of CdSe nanocrystals: (a)  $r=9.3 \text{ \AA}$ ; (b)  $r=10.0 \text{ \AA}$ ; (c)  $r=10.4 \text{ \AA}$ ; (d)  $r=10.7 \text{ \AA}$ ; (e)  $r=11.4 \text{ \AA}$ ; (f)  $r=12.3 \text{ \AA}$ ; (g)  $r=13.2 \text{ \AA}$ ; (h)  $r=14.1 \text{ \AA}$ ; (i)  $r=15.9 \text{ \AA}$ ; (j)  $r=18.0 \text{ \AA}$ ; (k)  $r=24.2 \text{ \AA}$ ; (l)  $r=33.5 \text{ \AA}$ ; from reference [Kat94]

etc.) have been synthesized, the most frequently used materials are still CdSe and CdS because of their bulk band gaps ( $E_g^{CdS}=2.42 \text{ eV}$ ,  $E_g^{CdSe}=1.74 \text{ eV}$  [Crc87]) which lead to a whole range of colours in the visible region when the size is reduced and the high quantum yields that can be achieved with these materials. In order to obtain a narrow size distribution, the synthesis is generally performed in organic solvents at high temperatures.

Besides spherical nanocrystals, more complex geometries such as rods and tetrapods can also be synthesized in a controlled way. Shape control of the nanocrystals can be achieved by manipulating the growth kinetics. This is possible because the growth of CdSe in the wurtzite structure is highly anisotropic when the system is kinetically overdriven by extremely high precursor concentrations. CdSe is an anisotropic material with a unique c-axis, and when overall growth rate is fast, growth is generally faster along this axis. If the overall growth rate is slow, a nearly spherical shape that minimizes the surface is favoured. So if the growth rate is increased significantly, the result is a rod like shape. In order to maintain control of the growth rate, it is necessary to change the surfactant. So hexylphosphonic acid (HPA) that binds strongly to cadmium ions is added to the pure TOPO [Pen00]. The so obtained rods show a larger splitting of absorbing and emitting states, they have a polarized emission along the long axis, a quantum

yield of about 1 %, and their band gap depends on the length of the rod [Li01].

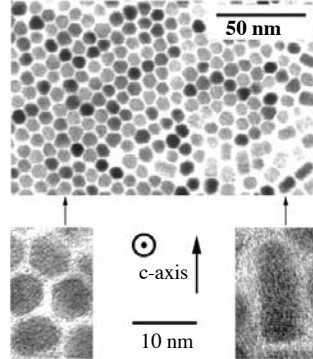


Figure 3.2: Orientation of quantum rods observed by TEM; from reference [Pen00]

Variation of the TOPO/HPA ratio leads to the growth of arrow or tree like forms. Tetra pods are formed when a CdSe nanocrystal nucleates in the zinc blende structure instead of the wurtzite structure. Then wurtzite arms grow out of the four (111) equivalent faces of the tetrahedral zinc blende core. More complex shapes, such as dendritic tetra pods, are produced by performing additional injections of precursor into a solution already containing tetra pods [Man00].

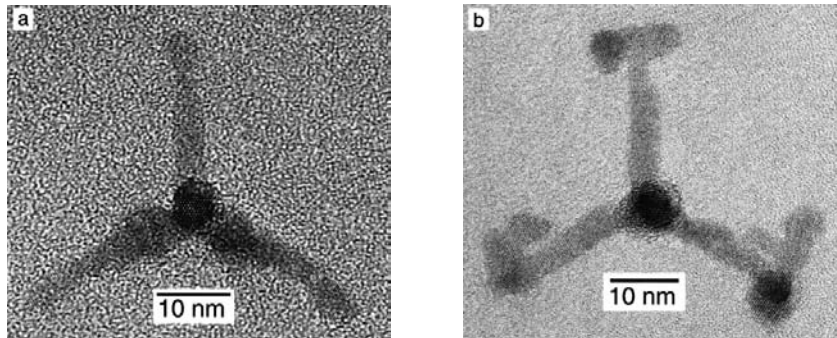


Figure 3.3: HRTEM images of (a) a typical tetra pod shaped CdSe nanocrystal, looking down the [001] direction of one arm. Lattice spacing confirms that all four arms are of wurtzite structure, (b) tetra pod that has branches growing out of every arm. There are zinc blende layers near the ends of the original arms, and the branches are wurtzite with some stacking faults; from reference [Man00]

### 3.1.1 Synthesis of doped ZnS

In recent years, also the optical properties of impurity-doped nanocrystals have attracted much attention. Since both electronic states and electromagnetic fields are modified, optical properties of impurities may change drastically in nanostructures. A favourable phosphor for these studies is  $\text{Mn}^{2+}$  doped ZnS-nanoparticles. Since the first report of ZnS:Mn nanoparticles [Bha94/2], several studies on doped metal chalcogenide quantum dots have appeared, including new preparation methods [Cou98, Soo96], luminescence properties [Bha94/2, Bol98, Yu96], and potential applications [Bha94/2, Din99]. For doped nanoparticles, the most fundamentally interesting results are the luminescence enhancement and the lifetime shortening of the  $\text{Mn}^{2+}$  emission [Bha94] with decreasing size. But for ZnS:Mn nanoparticles, many aspects concerning their photo physics are unclear and remain controversial.

Bulk ZnS is usually doped by thermal diffusion at high temperatures ( $>1100$  °C), but since nanocrystallites sinter at extremely low temperatures, they must be doped during precipitation. So to synthesize doped semiconductor nanocrystals a simple coprecipitation of the host material and the dopant is usually applied. The first synthesis of ZnS:Mn quantum dots carried out by Bhargava and co workers [Bha94/2] was made in toluene with diethyl salt precursors and methacrylic acid as surfactant. They obtained particles with two emission peaks (265 and 584 nm) and a 18% QY at room temperature. Since then a lot of syntheses both in water and organic solvents have been carried out with changing surfactants such as hexametaphosphate [Bol98], thioglycerol [Eth03], polyethylenoxide [Gal94], and hydroxypropyl cellulose [Soh98]. They were synthesized in block copolymer nanoreactors [Kan99] and zeolites [Che01], and with different amounts of  $\text{Mn}^{2+}$  to investigate the influence of the dopant concentration on the fluorescence properties [Bol98, Soo96], see figure 3.4.

## 3.2 Coating of particles

The surfaces of nanocrystals play a key role in virtually every property, from structural transformation to light emission to solubility. Control of the surface is in particular the key to highly luminescent nanocrystals. Organically capped nanocrystals are reported to have room temperature quantum yields of about  $\sim 10$ -15% [Dab97, Mur93] for CdSe and about 1% for CdS [Spa87] in water. For manganese doped ZnS synthesized in organic solvent quantum yields of 3-6% [Lee99] up to 18% were reported [Bha94]. One of the limiting factors for luminescence of nanoparticles is radiationless recombination of the electron and the hole at defect states at the particle surface, arising from surface nonstoichiometries, so called "dangling", what means unsaturated bonds [Eyc00]. Saturation of these bonds with an inorganic capping layer leads to remarkable increases in

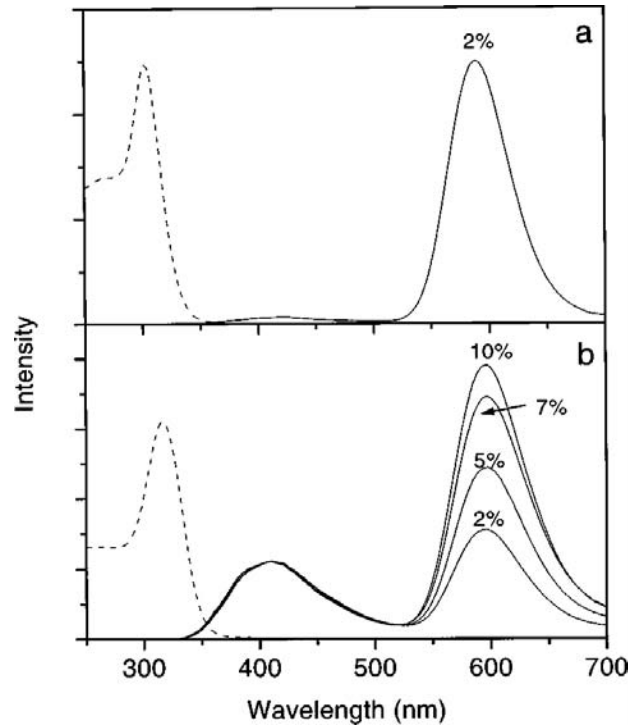


Figure 3.4: Emission spectra (solid lines), recorded for  $\lambda_{ex}=300$  nm, and excitation spectra (dashed lines), recorded for  $\lambda_{em}=590$  nm, of ZnS:Mn nanocrystals, made using (a) organometallic synthesis route, and (b) inorganic synthesis route. In the figure the manganese precursor percentages relative to Zn are mentioned; from reference [Bol98]

the fluorescence quantum yields. Henglein and co workers reported in 1987 an increase of the fluorescence intensity for CdS sols, when Cd(OH)<sub>2</sub> was precipitated at the particle surface. When they synthesized co-colloids of CdS and ZnS quantum yields of 50% could be achieved [Spa87]. CdSe synthesized by the inverse micelle method has been successfully capped with ZnS [Kor90] and ZnSe [Hoe92], particles from TOP/TOPO synthesis were also capped with ZnS or CdS and showed afterwards quantum yields of 50-70% [Dab97, Pen97, Hin96]. To perform the coating first the quantum dots are synthesized and the shell is then precipitated in a second step on the particle surface by addition of the shell precursors. The shell material used for the respective particles must meet two conditions. First it must be a material with a higher band gap than the core, otherwise one would excite the shell and not the core, and there must be sufficient lattice match between the two materials.

This leads to problems for coatings of ZnS nanoparticles. Since ZnS is a material with high band gap energy (3.6 eV [Gum81]) there exists no other semiconductor with a band gap sufficiently higher than the one of ZnS. So until now there is not

much literature about coating of ZnS nanocrystals. Velikov *et al* [Vel01] reported the coating of 100 nm ZnS particles with SiO<sub>2</sub> by the Stöber method [Stö68], but did not investigate the changes in optical properties. SiO<sub>2</sub> thin films loaded either with ZnS [Heb01] or manganese doped ZnS (ZnS:Mn) [Bha02, Bha02/2] were synthesized without investigating the changes in quantum yield. To our knowledge the only ones who observed an increase in fluorescence intensity for SiO<sub>2</sub> coated ZnS:Mn nanoparticles are Ethiraj *et al* [Eth03]. To obtain this increase in fluorescence they synthesize ZnS:Mn particles with thioglycerol as surfactant. After particle synthesis the SiO<sub>2</sub> shell was formed with TEOS (tetraethylorthosilicate). Particles with a diameter of about 600 nm diameter were obtained, unfortunately the fluorescence increase was not further quantified.

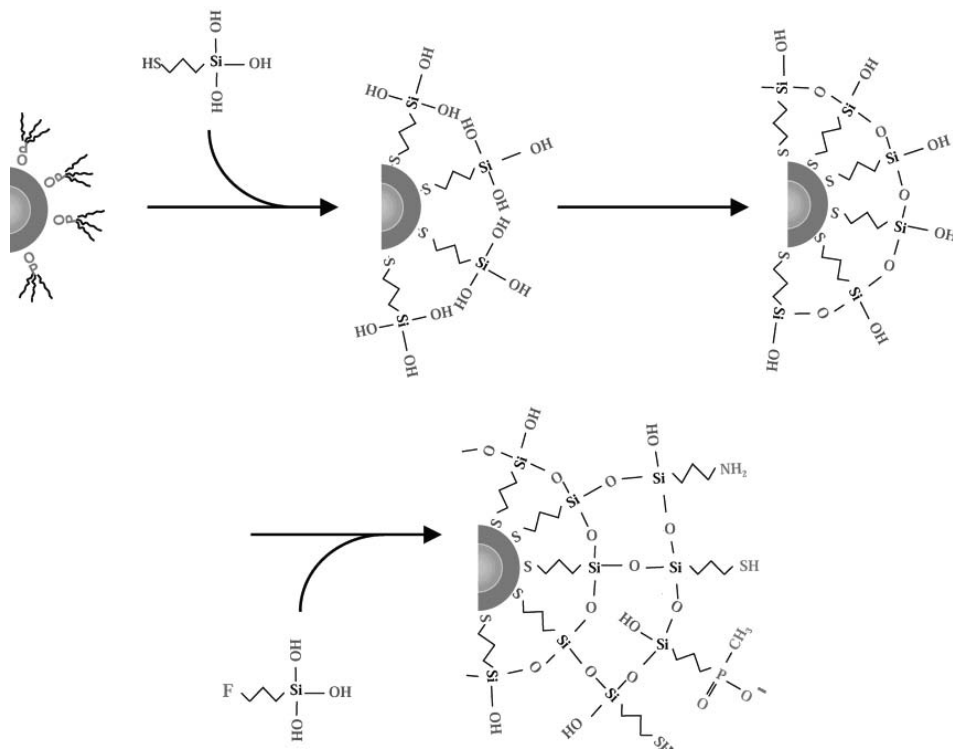


Figure 3.5: Sketch of the silanization method. The TOPO-capped CdSeZnS core/shell particles are dissolved in pure MPS to replace the TOPO molecules at the surface. The methoxysilane groups (Si-OCH<sub>3</sub>) hydrolyze into silanol groups (Si-OH), and form a primary polymerization layer. Then, fresh silane precursors containing a functional group (F=-SH, -NH<sub>2</sub>, PO(O<sup>-</sup>CH<sub>3</sub>)) are incorporated into the shell and may tailor the nanocrystal surface functionality; from reference [Ger01]

Since biological processes are typically situated in an aqueous environment, a hydrophilic nanocrystal surface is desired for reactions with biological molecules. The best particles in terms of quantum yield and size distribution are ZnS coated CdSe particles synthesized in TOPO [Dab97]. Their surface is hydrophobic and therefore they are not directly soluble in aqueous solution. The easiest way to obtain a hydrophilic surface is by exchanging the hydrophobic TOPO surfactant molecules with bifunctional molecules that are hydrophilic on one end and bind to ZnS with the other end. Commonly, thiols (-SH) are used as ZnS-binding groups, and carboxylic groups (-COOH) are a prominent example for hydrophilic groups. In this way TOPO -capped CdSe/ZnS nanocrystals can be transferred into aqueous solution by exchanging TOPO adsorbed at their surface for a layer of mercaptocarboxylic acids. Unfortunately their solubility in water is limited [Ald01]. A method to obtain more stable particles is a surface silanization. The first step is to bind a layer of mercapto-trimethoxysilane (MPS) molecules to the surface via thiol/ZnS bonds. The trimethoxysilane groups can be cross-linked, which greatly stabilizes the silane layer on the CdSe/ZnS surface. In the second step, hydrophilic trimethoxysilane molecules are added. By cross linking the trimethoxysilane groups through the formation of siloxane bonds, this shell is connected with the first layer [Bru98, Ger01, Par02]. The hydrophilic trimethoxysilanes used have two different head groups, phosphonates or ammonium heads, both are charged in aqueous medium (figure 3.5) [Par02]. In this way the particles repel each other electrostatically and they are soluble at micro molar concentrations in buffer solutions of a few hundred milli molar ionic strength. Importantly the quantum yields remain about  $\sim 60-80\%$  of the initial QY of the CdSe/ZnS nanoparticles in toluene and does not decrease by a factor of 20 like reported by Rogach *et al* for CdSe/SiO<sub>2</sub>, CdS/SiO<sub>2</sub> and CdSe/CdS/SiO<sub>2</sub> systems [Rog00].

## 3.3 ZnS:Mn nanoparticles

### 3.3.1 Fluorescence characteristics and doping

Considerable experimental work has been performed in the past years in order to understand the physical and chemical properties of Mn<sup>2+</sup> doped ZnS nanoparticles, but still a lot of things are unclear. For example the effect of quantum confinement on the luminescence efficiency is a point of debate. Nevertheless, strong photoluminescence is observable from ZnS:Mn nanoparticles due to the Mn<sup>2+</sup> in the ZnS host. This produces localized levels (<sup>4</sup>T<sub>1</sub> and <sup>6</sup>A<sub>1</sub>) in the energy gap of the semiconductor ZnS particles due to crystal field effects [Bha94/2] similar to those in the bulk material [Gum81]. An electron can undergo photo excitation in the host ZnS lattice and subsequently decay via a nonradiative transition to the <sup>4</sup>T<sub>1</sub> level from which it then makes a radiative transition to the <sup>6</sup>A<sub>1</sub>

level which results in an emission at about 580-600 nm. This is the same transition as in the bulk material, and it has been reported by several groups [Bha94/2, Bol00], that the transition does not seem to be much influenced by the particle size. However, the energy gap is larger in nanocrystals and an excitonic peak is observed in the optical absorption spectrum.

But the quantum size effect does influence the lifetime and fluorescence efficiency of the ZnS:Mn particles. To account for the phenomena Bhargava and Gallagher [Bha94/2, Bha96] suggested that with decreasing particle size a strong hybridization of the s-p states of the ZnS host and the d states of the  $\text{Mn}^{2+}$  impurity could occur. This hybridization results in a faster energy transfer between the ZnS host and the  $\text{Mn}^{2+}$  impurity. Due to this fast energy transfer, the radiative recombination at the  $\text{Mn}^{2+}$  impurity, which competes with nonradiative decay at the surface, becomes more efficient. This results in increased quantum efficiency.

In figure 3.4 it can be seen that a second emission at about 390 nm exists which is due to the ZnS host. This blue emission has also been observed in the bulk material, and has been termed "self-activated" and is due to sulphur vacancies in the lattice. These vacancies produce localized donor sites which are ionized at room temperature to populate the conduction band [Bec83]. Thus in the bulk the emission seems to arise from band-gap or near band recombination. However, pure band gap emission from particles with a radius smaller than the exciton Bohr radius would lead to emission in the UV, and it is therefore suggested, that the emission is due to shallow electron traps acting as recombination centres for photogenerated charge carriers [Häs93].

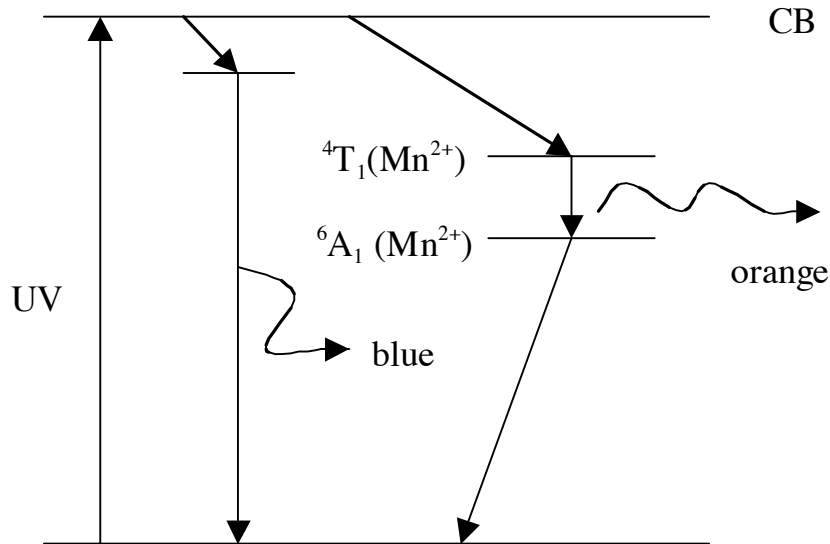


Figure 3.6: Recombination mechanism for the ZnS:Mn system.



Bhargava *et al* performed luminescence measurements on  $\text{Mn}^{2+}$  doped ZnS nanoparticles as powders and in an organic polymer matrix [Bha94/2]. An increase in the luminescence intensity on irradiation with UV light was reported and it was hypothesized that passivation of the surface of the nanoparticles by photo polymerization of the stabilizer (methacrylic acid) leads to a decrease in surface related nonradiative processes and therefore to an increase in luminescence intensity [Bha94/2, Gal94]. An activation of the luminescence in ZnS:Mn nanocrystals, stabilized with polymethylmethacrylate (PMMA) in ethanol was also detected by Jin *et al* after UV irradiation for 1h [Jin96].

To optimize the photoluminescence emission the  $\text{Mn}^{2+}$  content in the particles was varied (see figure 3.4) by several groups. It could be seen, that the luminescence intensity increases first with the  $\text{Mn}^{2+}$  content, but reaches a maximum and decreases afterwards. Different values for this maximum have been found such as 0.12 wt% [Kho95], 0.78 at% [Bol01], 2% (no additional information if it is wt%, mol% or at%) [Soo96], and 2 mol% [Soh98]  $\text{Mn}^{2+}$  related to  $\text{Zn}^{2+}$ . Possible reasons given for this behaviour are concentration quenching due to increasing crystal distortion [Bha94/2], an enrichment of  $\text{Mn}^{2+}$  at the surface of the ZnS particles or the formation of separate MnS particles [Soh98].

To determine the position of  $\text{Mn}^{2+}$  in the nanocrystals ESR measurements have been reported in literature. Generally, two distinct signals can be distinguished from ESR spectra of ZnS:Mn: a hyperfine structured spectrum and a broad background [Lev97, Ken95, Cou96]. The broad line has been assigned to the  $\text{Mn}^{2+}$  ions occupying the  $\text{Zn}^{2+}$  sites in ZnS [Lev97, Ken95, Cou96]. The broadening is attributed to the Mn-Mn dipolar interactions in the aggregated nanoparticles [Ken95]. The hyperfine structured signal is associated with isolated  $\text{Mn}^{2+}$  ions near the surface of a nanoparticle ( $\text{Mn}^{2+}$  ions at the near-surface sites) [Ken95, Cou96].

### 3.3.2 Lifetime measurements

In 1994 Bhargava and Gallagher [Bha94/2] reported that doped nanocrystals of semiconductors can yield both high luminescence efficiencies and lifetime shortening from ms to ns at the same time (lifetime of the orange bulk ZnS:Mn is 1.8 ms [Gum81]). To account for this phenomenon they suggested [Bha94/2, Bha96] that the hybridization of the d orbitals involved in the spin forbidden  ${}^4T_1 - {}^6A_1$  transition of the  $\text{Mn}^{2+}$  impurity, with the p orbitals of the ZnS host leads to shorter decay times.

Besides the group of Bhargava, a few other groups also reported the observation of lifetime shortening of the  $\text{Mn}^{2+}$  emission due to quantum confinement effects. Sooklal *et al* [Soo96] observed ns decay times for the  $\text{Mn}^{2+}$  in nanoclusters of ZnS:Mn, while Ito *et al* [Ito97] reported lifetime shortening to  $\mu\text{s}$  in two dimensional ZnTe:Mn quantum wells.

Unfortunately these articles on short lifetimes for the  $\text{Mn}^{2+}$  emission [Bha94/2,

Soo96, Yu97] do not describe experiments to verify the absence of a ms decay time in nanocrystalline ZnS:Mn, so it could not be excluded that there was still a ms decay present for the measured samples.

In 1998 Bol *et al* [Bol98] measured both the lifetimes of the  $\text{Mn}^{2+}$  and the blue ZnS emission. They reported a multi-exponential decay with a fast initial decay ( $\tau \cong 50$  ns) and a slower tail ( $\tau \cong 200$  ns) for the blue ZnS emission. Their set up did not allow for accurate determination of the short decay times.

For the orange emission they observed a fast multi-exponential decay ( $\tau \cong 40, 250$  ns). This fast decay is similar to the fast decay reported by Bhargava and Gallagher [Bha94/2] for the orange  $\text{Mn}^{2+}$  emission. Decay time measurements for the  $\text{Mn}^{2+}$  emission in the ms regime showed that, after an initial fast decay ( $\tau \cong 0.4$  ms), a slow single exponential decay with a decay time of 1.9 ms is present. The long decay time of 1.9 ms at 600 nm is, within the experimental error, identical to the decay time of the  $\text{Mn}^{2+}$  emission reported for Bulk ZnS:Mn (1.8 ms [Gum81]).

Murase *et al* [Mur99] observed also a ms lifetime for the  $\text{Mn}^{2+}$  emission, but could, with their set up, determine the decay of the blue emission to be in the range of 10 ns.

The described lifetime measurements observed all a shortening of the  $\text{Mn}^{2+}$  emission, but only Bol et Murase reported the presence of a second, longer ms lifetime. Since the way in which the measurements were taken out was not described in the respective articles, it is not clear if there was no ms lifetime present in the samples of the other authors or if they did not check on it.

Only Bol and Murase worked with set ups powerful enough to measure the blue ZnS emission for which they report both lifetimes in the ns region, Murase down to 10 ns.

### 3.4 Biological application

One of the most fascinating capabilities of many biological molecules is that of molecular recognition [Spi93, Fri00, Liu00]. Certain biological molecules can bind to other molecules with extremely high selectivity and specificity. This is similar to a lock-and-key system, but on a molecular level. This principle is used to visualize e.g. structural units in cells, that due to a lack of contrast or resolution, cannot be distinguished by just recording an image. In these cases fluorescence labels are attached specifically to a compartment in a cell. The idea is to chemically link a fluorescent dye to receptor molecules that specifically and selectively bind to the desired compartment in the cell. This receptor molecule typically is an antibody against the molecule to be labelled. Another very popular receptor is avidin or streptavidin: first, the molecule to be labelled is incubated with a biotinylated antibody, which is then recognized by the dye-avidin construct [Par03]. To use nanoparticles as fluorescent markers they have to be biofunc-

tionalized. Several strategies for the conjugation of water-soluble semiconductor nanocrystals with biological molecules have been reported. They include adsorption [Lak00, Mah00], linkage via mercapto groups [Mit99, Wil01], electrostatic interactions [Mat00, Mat01] and covalent linkage [Bru98, Cha98, Mam01]. For reasons of stability, covalent linkage seems to be the most desirable method. Alivisatos group in Berkley [Bru98] and Chan and Nie at Indiana University [Cha98] have exploited the narrow luminescence spectra of semiconductor nanocrystals for fluorescence studies of biological cells. Bruchez *et al* functionalized the surface of CdS-CdSe nanocrystals with tri-methoxysilylpropyl urea and acetate groups which promoted strong binding of the nanocrystals with the nuclei of fibroblast cells. Chan *et al* labelled ZnS-CdSe nanocrystals with the protein transferrin (via mercaptoacetic acid linkers). These nanocrystal bioconjugates were subsequently transported into cultured living cells and imaged using an epifluorescence microscope. Furthermore Chan and Nie [Cha98] have investigated the efficacy of nanocrystals for immunoassays, demonstrating that CdS- CdSe nanocrystals functionalized with immunomolecules could recognize specific antibodies and antigens.

# Chapter 4

## Conclusions and goals

Semiconductor nanoparticles have shown in the last 15 years that they can be an alternative to common organic dyes used in biological and medical analytics, and as tags for biomolecules. The most investigated systems are CdSe, CdTe and CdS nanocrystals. CdSe and CdTe are mostly synthesized with the TOP/TOPO synthesis, developed by Bawendi [Mur93]. CdS are most often synthesized in aqueous media with sodium hexametaphosphate as stabilizing agent [Foj84]. To increase the photoluminescence efficiency the particles have to be coated with higher band gap materials and SiO<sub>2</sub> shells have been applied to transfer particles synthesized in organic solvents into aqueous media [Ger01]. For these semiconductors different colours are obtained for different particle sizes, so control of the particle size is very important for these systems. Size selective methods such as size exclusion chromatography [Fis86, Fis89] and size selective precipitation [Mur93] have been applied after particle synthesis, or monodispersed particles were directly synthesized by controlling reaction kinetics [Kat94]. Doped ZnS particles have been synthesized in aqueous and organic medium by coprecipitation of the host and the dopant. First attempts to synthesize core/shell systems are in progress. The results for the optical properties of the system are still controversy especially where fluorescence lifetimes are concerned.

For all nanoparticle systems less work has been made to determine the chemical composition of the crystals. Fluorescence quantum yields are rarely measured and it is never explicitly explained how these measurements, when carried out, were done or by which parameters they are influenced. To determine particle sizes TEM and HRTEM images are the most current methods. Crystallite sizes are calculated with Scherer's equation from x-ray diffraction spectra. But to our knowledge real particle size distribution measurements with methods such as e.g. photon correlation spectroscopy (PCS) have never been made.

The goal of this work is the synthesis of colloidal nanoparticles for biological and medical analytics. They should be attachable to a waveguide to form a bioassay system for the detection of biomolecules (see figure 1.1). For this we

concentrated on doped ZnS nanocrystals. This system is less toxic compared to CdSe and CdTe, it is less investigated and there are no size selective methods or control of kinetics necessary to exactly control the size to obtain different emission colours, because this can be obtained with different doping metals independent of particle size. Another advantage of this system is the large stokes shift between excitation and emission. Since the luminescence excitation takes place over the band gap, but the emission comes from electronic states within the d-orbitals of the dopant, excitation and emission are well separated which facilitates the detection (see figures 3.4 and 3.6 for the ZnS:Mn system).

The goal was to directly synthesize small, doped ZnS particles with a relatively narrow size distribution in water. They should have a biofunctionalized surface for immobilization on waveguides. We chose ZnS:Mn as a model system because the bulk system is well investigated for its optical properties, so sufficient references for comparison of bulk and nanoparticle properties are available. The system should be characterized for its optical properties such as, quantum yield, luminescence lifetimes and influence of the doping on the photoluminescence. A detail particle size investigation and studies on the chemical properties should be carried out, to obtain a well characterized system apt to be used in medical and biological fluorescence detection. To do multicolour experiments the particles should also be doped with different metals such as Cu, Ag, Eu if possible.

# Chapter 5

## Characterization methods

### 5.1 Fractionating hydrodynamic methods

#### 5.1.1 Analytical ultra centrifugation

Analytical ultra centrifugation (AUC) is a classical technique for polymer- and colloid analytics. It was established in the 20's by Svedberg who was interested in the observation of the sedimentation process itself [Sve23]. Initially, AUC was used for particle size analysis but was also quickly used for the characterization of biopolymers [Sch00].

In an AUC, rotational speeds up to 60000 rpm (270000 fold gravitational force) can be realized. For measurement the sample is placed in a sector shaped measuring cell inside the rotor. The cells are sector shaped to prevent convection. The sedimentation process can then be observed by different computer based on-line detection systems such as UV/Vis absorption or Raleigh interference optics (see figure 5.1). The Lamm differential equation is the basic equation for the analysis of the AUC results [Sch00]:

$$\left(\frac{\partial c}{\partial t}\right) = -\frac{\partial}{r_r \partial r_r} \left( c \cdot s \cdot \omega^2 \cdot r_r^2 - D \cdot r_r \left( \frac{\partial c}{\partial r_r} \right) \right) \quad (5.1)$$

It describes the concentration changes in the ultracentrifuge cell with time  $\frac{\partial c}{\partial t}$  where  $r_r$  represents the radial position,  $s$  the sedimentation coefficient,  $\omega$  the centrifugal velocity and  $D$  the diffusion coefficient. The Lamm equation cannot be exactly solved. However, different approximative solutions exist. The Lamm equation defines the four different basic experiments with the analytical ultracentrifuge:

- Sedimentation velocity
- Synthetic boundary

- Sedimentation equilibrium
- Density gradient

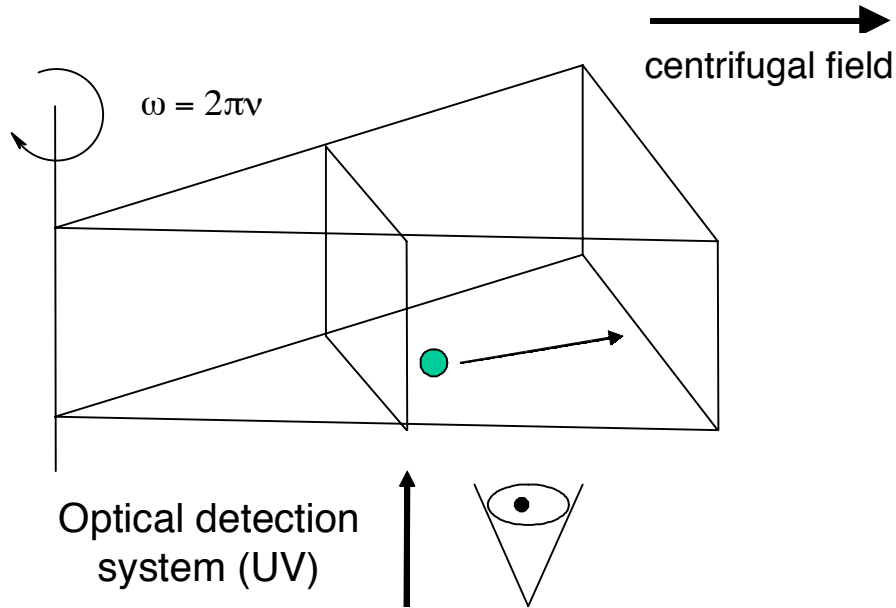


Figure 5.1: Experimental setup for analytical ultra centrifugation measurement

### Sedimentation velocity experiment

In a sedimentation velocity experiment, high centrifugal fields are generated by high rotational speed so that sedimentation prevails over back diffusion. The observation of the movement of the sedimenting boundary with time allows direct conclusions about sample homogeneity. A monodisperse sample would have a step-like radial concentration profile when diffusion is neglected. Furthermore, sedimentation velocity experiments yield sedimentation- and diffusion coefficients, hydrodynamic radii and molar masses  $M$  or particle size distributions.

For particles in a centrifugal field one can write:

Buoyancy force:

$$F_B = -m \cdot \bar{v} \cdot \rho_S \cdot \omega^2 \cdot r_r = -\frac{M}{N_A} \cdot \bar{v} \cdot \rho_S \cdot \omega^2 \cdot r_r \quad (5.2)$$

with  $m$  the mass of the particle,  $\bar{v}$  the partial specific volume and  $\rho_S$  the density of the dispersing medium.

Frictional force:

$$F_F = -f \cdot u \quad (5.3)$$

where  $f$  is a concentration and shape dependent frictional coefficient and  $u$  the sedimentation velocity.

Centrifugal force:

$$F_C = m \cdot \omega^2 \cdot r_r = \frac{M}{N_A} \cdot \omega^2 \cdot r_r \quad (5.4)$$

After a short period of time the particle velocity is constant and force equilibrium is achieved:

$$F_B + F_F + F_C = 0 \quad (5.5)$$

The sedimentation coefficient  $s$  is defined as:

$$s \equiv \frac{u}{\omega^2 \cdot r_r} = \frac{M(1 - \bar{v} \cdot \rho_S)}{N_A \cdot D} \quad (5.6)$$

$s$  is given in Svedberg units ( $1S = 10^{-13}s$ ).

With the Stokes - Einstein equation

$$f = \frac{R \cdot T}{N_A \cdot D} \quad (5.7)$$

where  $R$  is the gas constant, the Svedberg equation can be derived:

$$M = \frac{s \cdot R \cdot T}{D \cdot (1 - \bar{v} \cdot \rho_S)} \quad (5.8)$$

During a sedimentation velocity experiment for every  $r_r$  the  $s_r$  is determined and so the  $s$  - distribution  $g(s)$  can be derived [Sta97]. The  $s$ -distributions do not allow conclusions about the particle size, but direct conclusions about the sample homogeneity are possible. With equation 5.9 the particle size distribution can be calculated, but in addition to the viscosity of the dispersing medium  $\eta_S$  one has to know the particle density  $\rho_P$ .

$$d_r = \sqrt{\frac{18 \cdot \eta_S \cdot s_r}{\rho_P - \rho_S}} \quad (5.9)$$



### 5.1.2 Field flow fractionation

Field flow fractionation is a family of flexible analytical fractionating techniques which have the great advantage that separation is achieved solely through the interaction of the sample with an external physical field and without a stationary phase. This has the advantage of avoiding the large variety of problems due to non specific sample interactions with column materials associated with other chromatographic techniques [Cöl00]. The fundamental principle of FFF is illustrated in figure 5.2. The separation of the sample takes place inside a narrow ribbon-like channel. This channel is composed of a thin piece of sheet material (usually 70-300  $\mu\text{m}$  thick Mylar or polyimide) in which a channel is cut and which is usually clamped between two walls of highly polished plane parallel surfaces through which a force can be applied. A carrier fluid is pumped through this channel from the inlet, where the sample is injected, to the outlet, to which a detector is connected.

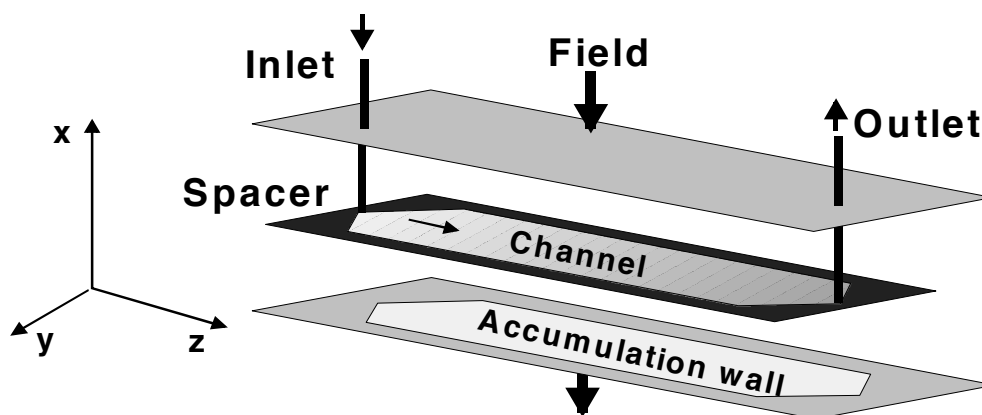


Figure 5.2: Experimental setup for a FFF experiment; from reference [Cöl00]

Inside the channel, a parabolic flow profile (laminar Newtonian flow) is established as in a capillary tube. Thus, flow velocities vary from zero at the walls to a maximum in the centre of the channel. While the carrier liquid with the sample is flowing through the channel, an effective physical or chemical field is applied across the channel perpendicular to the flow direction of the carrier liquid. Interaction with the field concentrates the solute at one of the channel walls, called the accumulation wall. The centre of gravity of the solute zones lies very near to the wall, usually extending only a few micrometers. Due to the established concentration gradient, a diffusion flux in the reverse direction is induced according to Fick's law. After a short time a steady state is reached, and the exponential distribution of the solute cloud across the channel can be described by a mean

layer thickness.

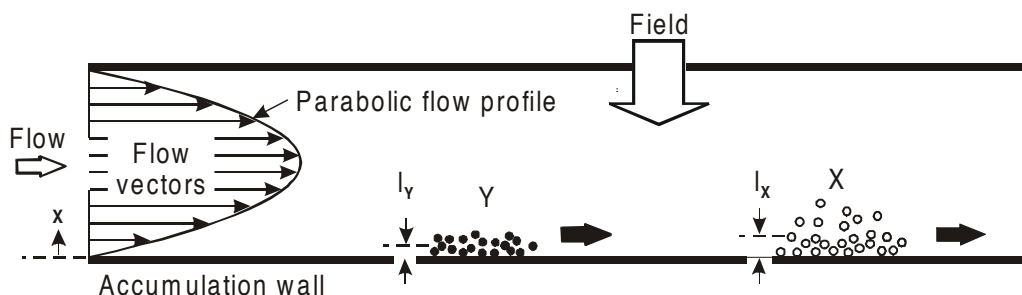


Figure 5.3: Flow profile and separation in the FFF channel; from reference [Cöl00]

Due to the parabolic flow velocity profile, the solutes are transported in the direction of the longitudinal channel axis at varying velocities, depending on their distance from the channel walls. The nearer the solute is located to the accumulation wall, the later it will elute. Since smaller molecules (X) diffuse faster than larger ones (Y) and so establish a higher layer thickness  $l$ , the elution sequence proceeds from the smaller solutes to the largest ones (see figure 5.3). Hence, the flow velocity profile of the carrier liquid amplifies very little distance differences between the solute clouds in the  $x$ -direction, leading to the separation.

Because of the different external fields possible, one distinguishes between different FFF techniques:

- Sedimentation FFF
- Thermal FFF
- Electrical FFF
- Flow FFF
- Steric FFF
- Magnetic FFF
- Concentration FFF

In this work asymmetric flow field flow fractionation (aF-FFF) was applied. In this technique a secondary cross-flow  $V_c$  of the solvent, perpendicular to the flow of the solvent in the channel, creates the external field. AF-FFF is notable for a channel which has only one permeable wall so that the solvent can leave the channel only via the accumulation wall and thus generates the cross-flow. The continuous loss of carrier fluid through the membrane as it flows down the channel

leads to a gradual fall in volumetric flow rate between the inlet and outlet leading to a gradient in the mean channel flow velocity in channels with constant breadth. To compensate for this undesired effect, a trapezoidal channel was introduced, and is almost exclusively applied now. When the channel geometry is known, the diffusion coefficient of the eluted species can be calculated with the help of the measured retention time  $t_r$ , the void time  $t_0$  and the channel volume  $V_0$ :

$$t_r = \frac{t_0 \cdot \dot{V}_c \cdot w^2}{6 \cdot D \cdot V_0} \quad (5.10)$$

Combining this equation with the Stokes-Einstein relation leads to the hydrodynamic diameter:

$$d_H = \frac{2 \cdot k_B \cdot T \cdot V_0}{\pi \cdot \eta_S \cdot \dot{V}_c \cdot w^2 \cdot t_0} \cdot t_r \quad (5.11)$$

If the channel width is known the particle diameter can be determined. Unfortunately the channel width is not constant because the membrane swells with time. So one has to regularly measure a reference substance of which the diameter is known. The most common molecule for these reference measurements is Ferritin which has a diameter of 12 nm [Cöl00].

## 5.2 Photon correlation spectroscopy

A little over a hundred years ago J. W. Strutt answered the question of what causes light scattering, and, in doing so, also answered the age old question of why the sky is blue. Strutt became Lord Raleigh, and the basics of light scattering were laid.

Light may be treated as an electro-magnetic wave. The oscillating electro-magnetic field induces oscillations in the electrons in a particle. Over the years many features of the scattered light have been used to determine particle size. These include:

- Changes in the average intensity as a function of angle
- Changes in the polarization
- Changes in the wavelength
- Fluctuations about the average intensity

This later phenomenon is the basis of QELS (Quasi elastic light scattering), the technique employed by the Brookhaven 90Plus/BI-MAS particle sizing option. The motion of small particles in a liquid gives rise to fluctuations in the time intensity of the scattered light. The fluctuation signal is processed by forming

the autocorrelation function,  $C(t)$ ,  $t$  being the time of the delay. As  $t$  increases correlation is lost, and the function approaches the constant background term  $B$ . For short times the correlation is high. In between these two limits the function decays exponentially for monodisperse suspensions of rigid, globular particles and is given by

$$C(t) = A \cdot e^{-2 \cdot D \cdot q^2 \cdot t} + B \quad (5.12)$$

where  $q$  is

$$q = \frac{2 \cdot \pi \cdot n_L}{\lambda_0} \cdot 2 \sin \frac{\Theta}{2}, \quad (5.13)$$

with  $n_L$  the refractive index of the suspending liquid,  $\lambda_0$  the laser wavelength and  $\Theta$  the detection angle. The translational diffusion coefficient,  $D$ , is the principle quantity measured by QELS. It is related to the particle size via the Stokes-Einstein equation

$$D = \frac{k_B \cdot T}{3 \cdot \pi \cdot \eta_L \cdot d} \quad (5.14)$$

This equation assumes that the particles are moving independently from one another [Bro95].

### 5.3 X-ray diffraction

The characterization of powders by X-ray diffraction is based on the periodic arrangement of the atoms in the crystals. Therefore, only crystalline materials can be characterized by this method. The periodicities in different directions within a crystal are described by position vectors which define the so-called lattice. Any three lattice points define a lattice plan. The orientation of the plane with respect to a selected coordinate system is given by the indices  $hkl$ . The condition for in-phase scattering by a series of identical, parallel planes with the distance  $d_{hkl}$  is described by Bragg's law:

$$\lambda = 2 \cdot d_{hkl} \cdot \sin \theta_B \quad (5.15)$$

Where  $\theta_B$  is the Bragg angle. The Bragg law requires implicitly that the incident beam with the wavelength  $\lambda$ , the diffracted beam and the normal to the set of lattice planes under consideration are coplanar. Therefore, a particular set of lattice planes  $hkl$  of a single crystal can only diffract in one direction. A crystalline powder consists of a very large number of small single crystals, which, in the ideal case, are absolutely randomly oriented. For each crystal, the orientation of a specific set of lattice planes  $hkl$  will be different and Bragg's law will be satisfied by all crystals for which this specific set of lattice planes  $hkl$  forms

the Bragg angle  $\theta_B$  with the incident beam. Consequently the beams diffracted by an ideally random oriented powder sample form a cone around the incident beam direction. The angle between incident and diffracted beam is always  $2\theta_B$ . As in general, the absolute intensity of the incident beam is not known, the intensities of the diffracted reflections are always expressed in relative values. That is, the most intense peak is set to 100 and the intensities of the remaining peaks are expressed in percent of this peak.

The following information can be extracted from a diffraction spectrum. From the peak position (diffraction angles) together with their relative intensities the crystalline phase in the sample can be identified. The intensities of the diffracted peaks allow to quantify the phases, to detect preferred orientations of the crystals in the sample (texture) or to determine the atomic arrangement in the crystal (structure). The profile of the diffracted lines contains information on the size and on non homogeneous strain within the crystals due to stresses and defects, whereas homogeneous strain give rise to a shift of the diffracted lines with respect to an unstrained sample [Kit99, Moe00].

### 5.3.1 Size determination

It must be underlined, that the size determined by diffraction methods corresponds to the magnitude of the so-called coherent crystal regions, that is, to regions where the periodic arrangement of the atoms is perfect and contiguous. Even a monocrystal can be composed of several crystallites (so called mosaic crystal), the size determined by diffraction can in general not simply be compared to the sizes determined by other methods, e.g. PCS or TEM.

According to Bragg's law all beams scattered under the angle  $2\theta_B$  with respect to the incident beam will be in phase, that means, the distance covered by the waves scattered by different planes will defer by an integer factor  $A \cdot n$  of the wavelength. If the incidence angle  $\theta_B$  is changed by a small value  $\pm\delta\Theta$ , the differences in the distances covered by the different waves will be  $A \cdot n(\lambda \pm \Delta x)$ , where  $\Delta x$  ( $\ll \lambda$ ) is proportional to  $\delta\Theta_B$ . For a certain value  $A_1$ , we get  $A_1 \cdot n \mid \Delta x \mid = \frac{\lambda}{2}$ . That is, the waves scattered by the first plane and the plane number  $A_1$  will be completely out of phase and cancel each other. As a consequence, if the series of lattice planes consists of  $A_1$  planes, the intensity diffracted under the angle  $(\Theta_B \pm \delta\Theta)$  will be zero. As  $\Delta x$  is proportional to  $\delta\Theta$  and as  $A_1 \cdot n \mid \Delta x \mid = \frac{\lambda}{2}$ ,  $\mid \delta\Theta \mid$  will decrease as  $A_1$  increases. Thus, for lattice planes series consisting of a low number of planes, the deviation  $\pm\delta\Theta$  from the Bragg angle at which the intensity will be zero will increase. Unfortunately the line width is also influenced by the acquisition conditions and distortions of the elementary cell [Cul78, Moe00].

### Size determination according to Scherrer

This method uses as a measure for the size the width of the peak and avoids thus the determination of the full peak profile which is necessary for other methods. The full width at half maximum (FWHM) is generally used as it is rather easily measured.

Using Gaussian type profiles for the size distribution and for the instrumental effects, Scherrer derived a formula which allows the determination of the crystallite size from the line width of Debye-Scherrer patterns. Based on the assumption, that the form and the symmetry of the crystallites were cubic and no strain contributed to the profile, he found the following relation between the FWHM  $\beta_{\frac{1}{2}}$ , the x-ray wavelength  $\lambda$  and the crystallite size  $d$ :

$$\beta_{\frac{1}{2}} = \frac{0.94 \cdot \lambda}{d \cdot \cos\Theta} \quad (5.16)$$

Strictly speaking, the method due to Scherrer is only valid for crystals of cubic symmetry and if the peak broadening is only due to the crystallite size. Besides this, it applies to line widths measured on Debye-Scherrer patterns and assumes Gaussian like profiles. So, if these assumptions are not satisfied, the obtained values have to be considered as approximations [Cul78, Moe00].

### 5.3.2 The Rietveld method

X-ray diffraction of single crystals using relatively large crystals of the material, gives a set of separate data from which the structure can be obtained. However, most materials of technical interest cannot grow large crystals, so one has to resort to the powder diffraction technique using material in the form of very small crystallites. In a polycrystalline sample it is inevitable that certain information is lost as a result of the random orientation of the crystallites. A further, and in practice more serious, loss of information is a result of the overlap of independent diffraction peaks in the powder diagram. The method of using the total integrated intensities of the separate groups of overlapping peaks in the least-square refinement of structures, leads to a loss of all the information contained in the often detailed profile of these composite peaks.

The Rietveld method uses these profile intensities instead of the integrated quantities in the refinement procedure, to overcome this difficulty and to extract the maximum information possible from the powder diagram. For this a pattern is calculated from a series of structural and peak shape and width parameters, and compared with the observed data. Then the parameters are adjusted with a least-square process to obtain the most information possible from a pattern [Rie69, Rie88].

# Chapter 6

## Particle synthesis and properties

### 6.1 Experimental section

All chemicals were analytical reagent grade and used without further purification. Ultra-pure deionised water (Seralpur delta UV/UF setting, 0.055 mS/cm) was used in all synthesis steps. D-9527 Sigma cellulose membrane dialysis tubing with a molecular weight cut off at 12'000 was used in all dialysis steps.

**Synthesis of the particles** Fluorescent, L-cysteine coated ZnS:Mn<sup>2+</sup> nanoparticles were prepared by precipitation of the sulphide from aqueous solution of Zn<sup>2+</sup> and Mn<sup>2+</sup> salts in the presence of the surfactant L-cysteine. The following paragraph is describing the synthesis steps.

Solutions of ZnSO<sub>4</sub>·7H<sub>2</sub>O (1M, in 0.01 M HCl, pH 2.7), L-cysteine (0.25M, pH 5.5) and MnCl<sub>2</sub>·4H<sub>2</sub>O (0.01 M, 0.05-0.55 mol%) were mixed and precipitated with a Na<sub>2</sub>S·xH<sub>2</sub>O (pH 13.5, 1 M, S<sup>2-</sup>/Zn<sup>2+</sup> ratio of 2.0) solution in a N<sub>2</sub> atmosphere without stirring. After the Na<sub>2</sub>S injection a white, voluminous precipitate appears. It slowly dissolves under formation of ZnS:Mn<sup>2+</sup> nanoparticles during incubation under N<sub>2</sub> for 30 min and a 50°C thermal treatment for one hour. During the incubation time the pH slowly increases from 3.7 to 8.5. The obtained dispersions looked transparent and were purified by dialysis against demineralised water or NaOH (0.01M) leading to dispersions with a pH of either 8.5 or 12.

To isolate nanoparticles in the solid state they were either isolated by addition of cold ethanol and recovered by centrifugation at 4500 rpm or by freeze drying. Isolated nanoparticles obtained by precipitation with cold ethanol could be re-dispersed in water, while this was not possible with the freeze dried powders.

The phenomenon that powders isolated with ethanol are redispersable and those isolated by freeze drying not, can be explained by the enormous capillary forces that act on the particles during the freeze drying process. These forces nearly weld the particles together what makes a redispersion impossible. To prevent this, water soluble salts are normally added to the dispersions. They crystallize

between the particles and make the powders dispersible. In our case this is not possible since the particles flocculate when salts, even at low concentrations, are added to the dispersions.

**Synthesis of the Shell** To further stabilize the particles and to increase their fluorescence they were coated with a SiO<sub>2</sub> shell. To do this a 1 mM solution of 3-(mercaptopropyl)trimethoxysilane (MPS) was added to the particle dispersion and the dispersion agitated for 24 hours under N<sub>2</sub> at room temperature. After the addition of SiO<sub>2</sub>·NaOH solution it was agitated for another five days, again under N<sub>2</sub> at room temperature. For purification the dispersion was dialysed against NaOH (0,01 M).

### 6.1.1 Sample preparation

#### ICP measurements

For ICP measurements about 0.1 g of powder have been dissolved in 0.8 M HNO<sub>3</sub> to a final volume of 25 ml under the addition of H<sub>2</sub>O<sub>2</sub> to prevent the precipitation of sulphur. For determination of the Zn<sup>2+</sup> content the solution was then diluted by a factor of 10000 with 0.8 M HNO<sub>3</sub>. To determine the Mn<sup>2+</sup> for samples with different Mn<sup>2+</sup> contents, the solution was diluted by a factor 5-100 depending on the initial Mn<sup>2+</sup> addition.

#### Titration

For titration 0.1 g of powder has been dissolved in 5 M HCl to a volume of 25 ml. Then 1 ml of this solution was mixed with 10 ml of water, 4 ml of a NH<sub>4</sub>Cl/NH<sub>3</sub> buffer solution (pH 11, 1.3M) and a drop of eriochrome black T solution ( 0.1 g of erichrome black T in 15 ml of ethanolamine and 5 ml ethanol). This mixture was then titrated with a 0.01 M EDTA solution. The titter of this solution was determined with a 0.01 M solution of dry CaCO<sub>3</sub>.

### 6.1.2 Surfactants

Table 6.1: Characteristic constants for L-(+)-cysteine.

Isoelectric point	
pH <sub>iso</sub>	5.1
pK <sub>a</sub> (-COOH)	1.7
pK <sub>a</sub> (-NH <sub>3</sub> <sup>+</sup> )	8.2
pK <sub>a</sub> (-SH)	10.3



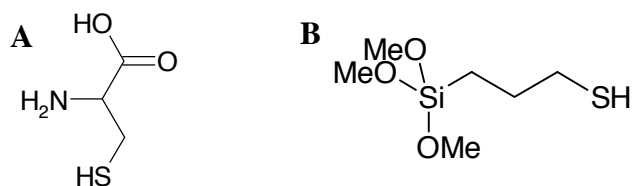


Figure 6.1: (A) Amino acid L-cysteine, (B) 3-(mercaptopropyl)trimethoxysilane (MPS)

For the development of this synthesis a screening of different surfactants (see table 6.2) has been carried out to obtain stable dispersions with high fluorescence intensities. The synthesis described above provides dispersions with average powder content of 8 g/l at a pH of 8.5 when dialysed against ultra pure water and a pH of 12 when dialysed against NaOH 0.01 M. They are stable from pH 8-14. The amino acid L-cysteine at the particle surface opens the possibility for a further functionalization of the surface with biomolecules.

Table 6.2: Used surfactants for particle synthesis

Surfactant	Comment
Alginate acid	Low concentration, particles cannot be isolated
Cysteine	High concentrations, dispersions stable for 3-4 weeks particles can be isolated
Dextran	At low concentrations no particle formation, at high concentrations dispersions not stable
Hexametaphosphat	Stable for 2-3 days
Hydroxypropyl cellulose	Stable dispersions, but poor fluorescence
Mercaptopropionic acid	Corrodes plastic parts
Polymethacrylic acid	Particles precipitate embedded in polymer matrix, cannot be dispersed
Polyvinyl alcohol	Stable for 2-3 days
Polyvinyl pyrrolidone	Stable dispersions, low concentrations, particles cannot be isolated
Thioglycerole	Basic pH needed for stabilization leads to Mn(OH) <sub>2</sub> and Zn(OH) <sub>2</sub> precipitation before addition of Na <sub>2</sub> S
TWEEN 80	Poor fluorescence

Zeta- potential measurements gave a value of about -55 mV for particles at a pH of 8.5. So the particles are negatively charged. At this pH the -COOH and the -NH<sub>3</sub><sup>+</sup> group of the cysteine at the particle surface are deprotonated, which explains the negative zeta potential.

For the shell synthesis 3-(mercaptopropyl)trimethoxysilane is added to the dispersion. This is a silane with a free SH-group linked by a propyl rest (see figure 6.1). The SH-group with its high affinity to the ZnS surface should attach additionally to the surface or partially replace cysteine already attached to the surface and so create a point of attack for the sodium silicate solution to precipitate on the particle surface instead of forming separate SiO<sub>2</sub> particles. The results for the shell synthesis are presented in chapter 6.6 and 8.1.4.

### 6.1.3 Dispersion stability

As noted in section 2.2 colloidal particles can either be stabilized electrostatically by surface charges or sterically by adsorption of a polymer or surfactant on the particle surface.

In the case of electrostatic stabilization the stability depends strongly on the ionic strength. Like it can be seen in equation 2.23 in section 2.2.2 the thickness of the double layer, and with this the stability of the dispersion, decreases with increasing ionic strength.

The particles synthesized with the method described above show a strong sensitivity on the ionic strength. Even the addition of small amounts of salts lead to flocculation of the particles. This indicates an electrostatic stabilization of the particles. For the synthesized particles a negative zeta potential was measured due to the at pH 8.5 negatively charged cysteine at the particle surface. The salt screens the charges at the particle surface and leads to an decrease of the thickness of the double layer which then leads to agglomeration.

The stability via the cysteine can also be seen when the dispersions are dialysed. When the dispersions are dialysed more than 24 hours particle agglomeration is observed. Since the cysteine attached at the surface is in equilibrium with the cysteine in solution, removal of the cysteine in solution via dialysis leads to the removal of cysteine from the particle surface until the surface charge is no longer sufficient to stabilize the particles (see section 2.2.2)

New studies of small particles with sizes below 10 nm, show that these nanoparticles do often show no electrostatic stabilization. De Gennes *et al* think that this is due to their low surface charge [Gen98]. Kallay *et al* analyzed the kinetics of aggregation of nanoparticles based on the Brønsted theory, which was developed for the salt effect on the kinetics of ionic reactions. They came to the conclusion that the classic DVLO approach cannot be used since the particles are small with respect to the thickness of the electrical diffuse layer, so that in the course of the collision of two nanoparticles a complete overlap of two diffuse layers takes place. According to the Gouy-Chapman theory (see equation 2.23) at the ionic strength of  $10^{-2} \frac{\text{mol}}{\text{l}}$  the diffuse layer is extended up to 6 nm from the surface. For particles with a radius of 3 nm this leads to a practically complete overlap of the respective double layers. In the case of ordinary colloid particles (particles with  $d > 10$  nm) the overlap is partial so that the DVLO theory is applicable [Kal02].

The theory of Kallay *et al* bases on the assumption that the particles are stabilized due to their surface charges without the adsorption of a small molecules or ions. Since we obtain particle dispersion stable for 3-4 weeks, other effects have to be taken into account. The cysteine adsorption cannot lead to a steric stabilization, it is too small for this, but it puts the charges about one nanometre above the particle surface, this can lead to an increase and a shift of the energy barrier responsible for electrostatic stabilization to higher distances (see figure 2.5). These changes will be small, but can already be sufficient to achieve stability at least for 3-4 weeks.

But the effects of Kallay *et al* still have to be proven. In our case the particles are electrostatically stabilized due to negative charges from the cysteine adsorbed on the particle surface. Steric contributions can be excluded since the cysteine is smaller than the double layer.

#### 6.1.4 Crystal structure

The reference spectra cited here can be found in the *Powder Diffraction File* Version 2000 data base or in the cited literature. The powders used for the X-ray diffraction (XRD) analysis were synthesized as described in the experimental section. The particles were isolated and washed with cold ethanol and dried at room temperature, or obtained by freeze drying from dialysed dispersions. The XRD pattern shown in figure 6.2 is typical for the powders regardless their way of isolation. The pattern is well matched with the cubic ZnS sphalerite structure, no second phase can be observed. The peak broadening clearly indicates that small nanocrystals are present in the sample.

In literature there is still some discussion concerning the crystal structure, Kho *et al* [Kho00] report for example the wurtzite structure for a x-ray pattern that has its peaks at the same positions as the pattern shown in figure 6.2. Their argument for the wurtzite structure is the absence of the (200) reflex at  $2.7 \text{ \AA}$ , which corresponds to a  $2\theta$  value of  $33^\circ$ . In table 6.3 one can see that this peak is present with an intensity of 10 % with respect to the most intense, the (111) peak. With the peak broadening, observable in the x-ray pattern in figure 6.2, it will not be possible to observe a peak with this intensity beside the peak for the (111) reflex.

Furthermore, the only reference pattern, found by the author, for ZnS with the wurtzite structure, with its three most intense peaks at the positions in figure 6.2, is for ZnS samples from a mine in North Joplin, USA [Eva59]. These are samples in which the zinc blende structure is present as a second phase and which contains 1.4 % of iron. The other patterns found for wurtzite structure have their most intense peak at  $3.3 \text{ \AA}$ , which should be visible in the x-ray pattern.

Table 6.3: Reflexions for  $2\theta = 10\text{-}80^\circ$  of the cubic zinc blende structure of ZnS, using  $\text{CuK}\alpha_1$  radiation [Swa53].

d [Å]	Int	hkl	$2\theta$
<b>3.123</b>	<b>100</b>	<b>111</b>	<b>28.5</b>
2.705	10	200	33
<b>1.92</b>	<b>51</b>	<b>220</b>	<b>47.5</b>
<b>1.633</b>	<b>30</b>	<b>311</b>	<b>56</b>
1.561	2	222	59
1.351	6	400	69.5
1.24	2	331	77

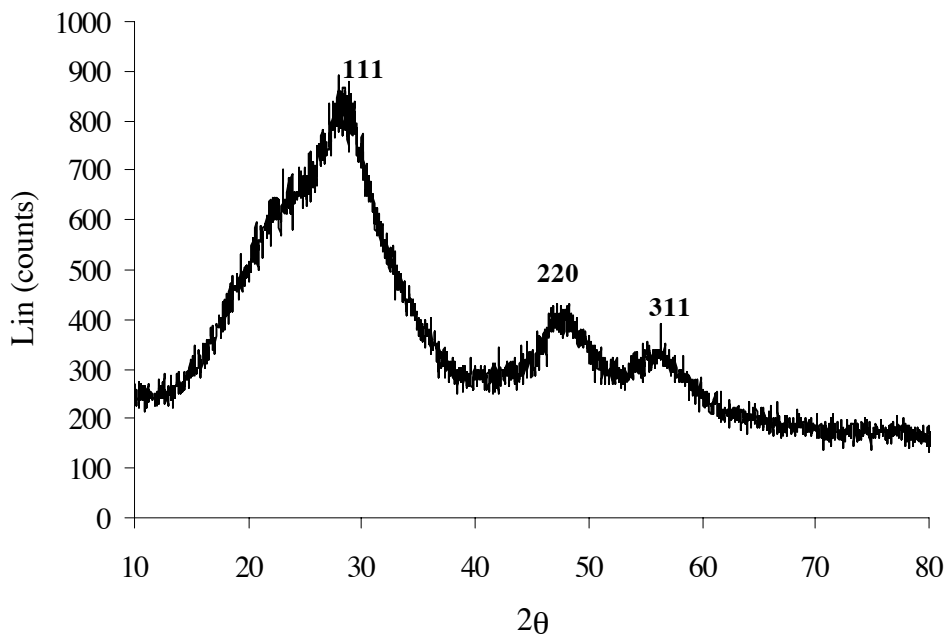


Figure 6.2: X-ray diffraction pattern of ZnS:Mn nanoparticles

To be sure of the crystal phase of the synthesized particles, Rietveld calculations were made at Ilford in Fribourg, which confirmed the cubic zinc blende structure. Here the obtained data are compared with a spectrum calculated from structural, peak shape and width parameters (see 5.3.2 [Rie69, Rie88]).

The measured and corrected spectrum can be seen in figure 6.3. It also shows

the cubic zinc blende structure. The spectra have been measured with the  $\text{CoK}_{\alpha 1}$  radiation which explains the shift for the peak positions compared with the spectra measured with the  $\text{CuK}_{\alpha 1}$  radiation. The calculated spectrum can be seen in annex C.

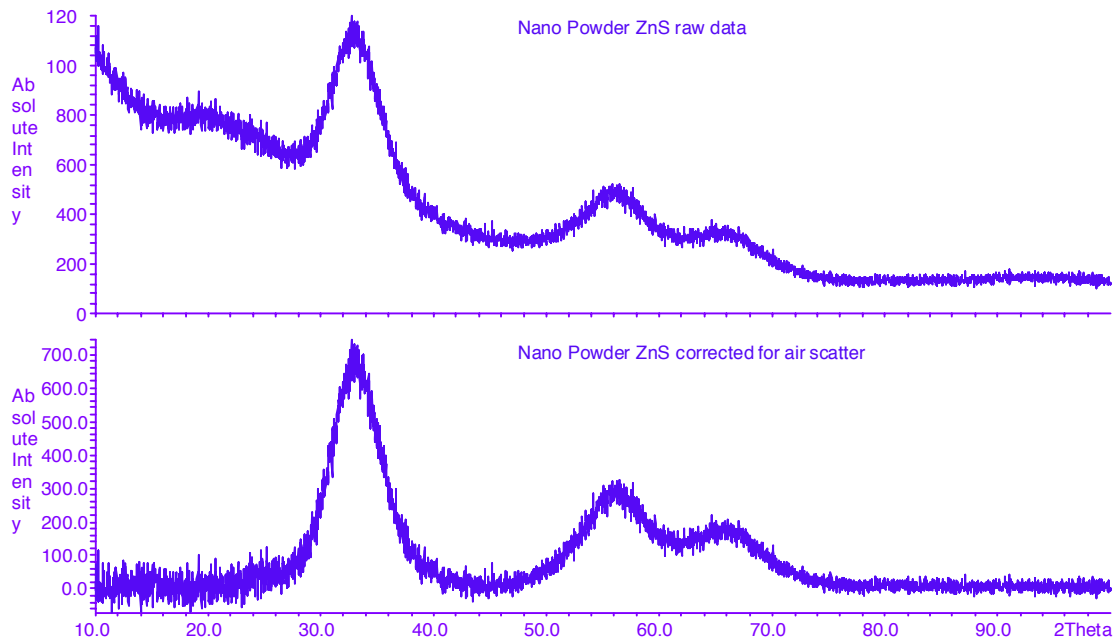


Figure 6.3: XRD pattern for ZnS:Mn nanoparticles measured with the  $\text{CoK}_{\alpha 1}$  radiation. Upper spectrum without background correction, lower spectrum with background correction.

### 6.1.5 Investigation of the precipitate

As noted above during particle synthesis, first a white, voluminous precipitate is observed floating in the reaction mixture, that slowly dissolves to form ZnS nanoparticles accompanied by a slow increase in pH from 3.5 to 8.5. It was further observed that agitation during synthesis leads to the formation of a white precipitate that sediments when agitation is stopped and does not dissolve afterwards. XRD measurements showed that this powder is cubic ZnS. When we tried to isolate the precipitate which forms without agitation prior to ZnS formation via centrifugation or filtration, XRD spectra always showed ZnS structure. To investigate this further, solutions of  $\text{ZnSO}_4$ ,  $\text{MnCl}_2$  and cysteine have been mixed as described in section 6.1. But instead of adding a  $\text{Na}_2\text{S}$  solution at pH 13.5 a 0.3M NaOH solution (pH 13.5) was added. The formation of the same white, voluminous precipitate as for the synthesis described in section 6.1 was observed. But the pH did not go up to pH 8.5, but only to a value of 4.5. After one hour a pH of 4.1 was measured. The precipitate did not dissolve and was so isolated, washed with demineralised water and dried at room temperature for further examination. In a second step the same procedure was carried out but this time in addition the cysteine solution was replaced by the same quantity of water. Also here a precipitate was formed, but this time it was not white but nearly transparent and gel-like. The pH increased directly to a value of 7 after NaOH addition, to then decrease to 6.5. The precipitate did not dissolve. For a last experiment the cysteine solution was kept and the  $\text{ZnSO}_4$  solution was replaced by water. No precipitate was formed after NaOH addition. The pH directly increased to 8.2. These observations lead to the following conclusions:

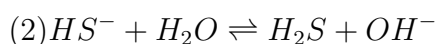
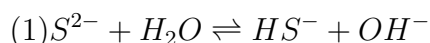
1. The  $\text{Na}_2\text{S}$  is not directly involved in the precipitation of the first white precipitate, but precipitation is induced by the pH of the injected solution.
2. ZnS precipitation starts only at a certain pH and dissolves the first precipitate, which indicates that  $\text{Zn}^{2+}$  ions are involved in the first precipitate. This is confirmed by the fact, that no precipitation follows on NaOH addition when  $\text{Zn}^{2+}$  is replaced by water.
3. The slow increase of the pH during synthesis is due to the  $\text{Na}_2\text{S}$ .
4. The gel-like precipitate that follows the NaOH addition to a  $\text{Zn}^{2+}$  solution must be  $\text{Zn}(\text{OH})_2$  which can precipitate at a pH of 7 but not at a pH of 3.5

Table 6.4: Observations for precipitation from different reaction mixtures

Conditions	Observations	pH
Reaction as described in section 6.1	white precipitate, dissolves slowly	increases slowly from 3.5 to 8.5
Na <sub>2</sub> S replaced by NaOH	white precipitate, does not dissolve	quickly up to 4.6, then stable at 4.1
Na <sub>2</sub> S replaced by NaOH, cysteine replaced by water	transparent, gel-like precipitate	quickly up to 7 then stable at 6.5
Na <sub>2</sub> S replaced by NaOH, ZnSO <sub>4</sub> replaced by water	no precipitation	pH goes directly up to 8.2

An IR spectrum of the precipitate obtained for NaOH injection in a mixture of cysteine, ZnSO<sub>4</sub> and MnCl<sub>2</sub> solutions is shown in picture 6.4. To simplify comparison a spectrum of pure cysteine is added to the graph. The region between 1800 and 300 cm<sup>-1</sup> clearly shows that cysteine is present in this precipitate. At 1581 and 1531 cm<sup>-1</sup> we have the bands for the COO<sup>-</sup> stretch and NH<sub>3</sub><sup>+</sup> deformation bands, and also other bands at lower wavenumbers correspond well to the pure cysteine spectrum. At wavenumbers higher than 1800 cm<sup>-1</sup> there are deviations from the reference spectrum. The NH<sub>3</sub><sup>+</sup> stretch (2090 cm<sup>-1</sup>) band can only be anticipated, and the SH stretch band (2559 cm<sup>-1</sup>) does not exist at all. The large band from 2300 to 3300 cm<sup>-1</sup> is shifted to higher wavenumbers (see figure 6.4). Cysteine is known to form highly stable complexes with Zn<sup>2+</sup> [Shi65]. This could explain the changes at higher wavenumber. The broad band centred at 3250 cm<sup>-1</sup> corresponds to the region where the asymmetric and symmetric stretching modes for a coordinated NH<sub>2</sub> group appear [His91] but it is also the region where strong water bands appear. So the shift of this large band and the only weak NH<sub>3</sub><sup>+</sup> stretch band could be due to a Zn<sup>2+</sup> cysteine complex that precipitates. But we have to take into account that we precipitated from aqueous solution and so the band could also be due to water.

The reaction mechanism is getting clearer when the pH dependency of the S<sup>2-</sup> concentration in aqueous solution is taken into account. H<sub>2</sub>S is a feeble acid. So S<sup>2-</sup> will act as a base in aqueous solution. This can be observed by the pH of S<sup>2-</sup> solutions which is 13.5 for a 1M Na<sub>2</sub>S solution [Hol95]. One obtains the following two equilibria in solution:



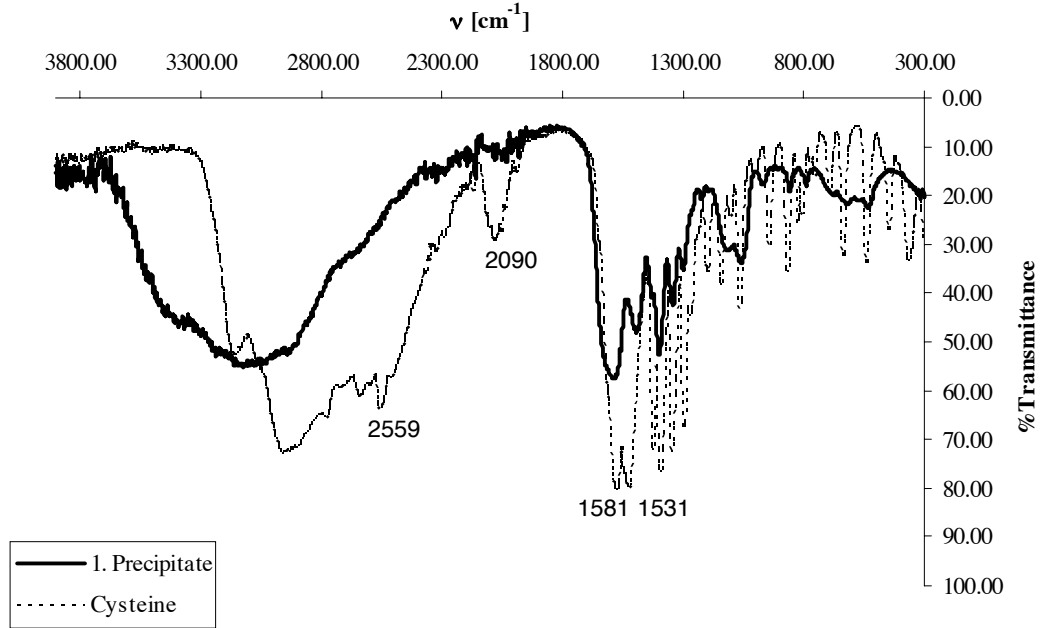


Figure 6.4: IR spectra of pure cysteine and the first precipitate.

These two equilibria have two dissociation constants to describe the total dissociation:

$$K_1 = \frac{[OH^-] \cdot [HS^-]}{[S^{2-}]} = 10^{-7} [mol/l] \quad (6.1)$$

$$K_2 = \frac{[OH^-] \cdot [H_2S]}{[HS^-]} = 10^{-1} [mol/l] \quad (6.2)$$

So the pH dependence of the  $S^{2-}$  concentration can be formulated as follows if  $[OH^-]$  is transferred to  $[H_3O^+]$  via  $[OH^-] \cdot [H_3O^+] = 10^{-14}$ :

$$[S^{2-}] = \frac{[H_2S] \cdot K}{[H_3O^+]} \quad (6.3)$$

with  $K = K_1 \cdot K_2 = 10^{-20} [mol^2/l^2]$  [Ger95]. This indicates that at high  $H_3O^+$  concentration or low pH the  $S^{2-}$  ion concentration in solution is low. In our case we have a pH of 3.5 of the reaction mixture before the addition of  $Na_2S$ , after  $Na_2S$  injection it goes up to a value of 8.5

in about half an hour. For a pH of 3.5 and a 1 M  $Na_2S$  solution we calculate with equation 6.3 a free  $S^{2-}$  concentration of  $10^{-13} \frac{mol}{l}$ . But  $ZnS$  has a solubility product of  $10^{-24}$  so this  $S^{2-}$  concentration is not sufficient to precipitate  $ZnS$ .  $ZnS$  precipitation starts at a pH of 4 under the given reaction conditions. So after the



$\text{Na}_2\text{S}$  injection no ZnS precipitation takes place. From a pH of 4 upwards ZnS precipitation starts. Since the Zn ions are incorporated in the cysteine complex there is not a pronounced supersaturation present in the solution part of the reaction mixture. This should normally lead to the formation of a small amount of germs during nucleation which then grow. In reaction mixtures with a high supersaturation more germs are formed during nucleation, they grow to form smaller particles than the ones obtained with small supersaturation. The fact that we obtain dispersions with small particle sizes can be explained by a reaction mechanism where the particle growth takes place close to or in the precipitated complex, where we have a high supersaturation. The so formed particles can than directly be stabilized by the cysteine.

## 6.2 Absorption, excitation and emission spectra

It is well established that when the particle size of a semiconductor becomes comparable to the de Broglie wavelength of an electron or hole, three dimensional quantum confinement, imposed by the dimensions of the nanocrystal, occurs.

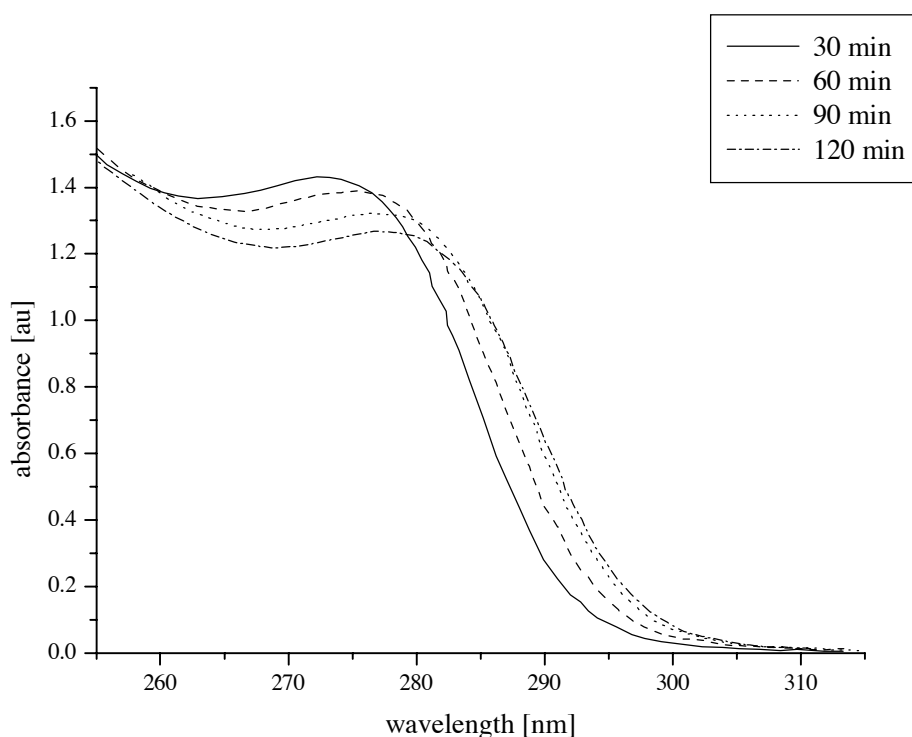


Figure 6.5: Absorption spectra recorded after 30, 60, 90 and 120 minutes after  $\text{Na}_2\text{S}$  injection. Red shift of the exciton peaks indicates particle growth.

The shift of the absorption edge, which corresponds to the band gap energy, of the semiconductor to higher energy provides experimental evidence for such quantum confinement and corresponds to an increase of the energy gap between the valence band and the conduction band of the semiconductor (see section 2.3). In figure 6.5 one can see that the band edge is shifted to about 310 nm. The shoulder present in the spectrum is assigned to the optical transition of the first excitonic state [Wel93]. The quantum size effect was used to observe particle growth during synthesis. To do so, samples of the dispersion have been taken after 30, 60, 90, and 120 minutes after  $\text{Na}_2\text{S}$  injection and examined for their absorption properties. For a better observation of the red shift with reaction time, we observed the shift of the shoulder rather than the shift of the onset of absorption. Figure 6.5 shows the respective absorption spectra. For all four spectra the onset of absorption is clearly blue shifted compared with the bulk value of 342 nm [Gum81]. With reaction time the maximum shifts to higher wavelengths indicating particle growth and a decrease in band gap energy (see equation 2.29 in chapter 2.3).

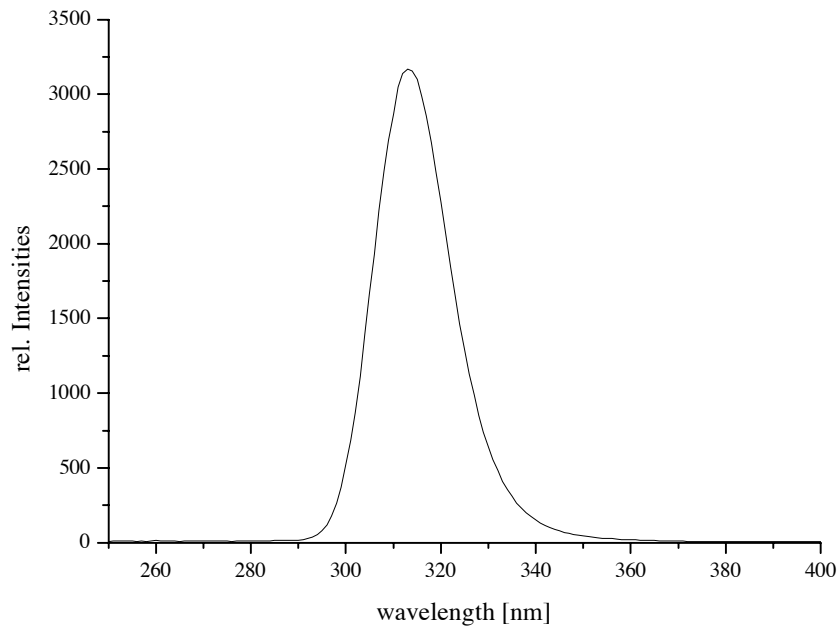


Figure 6.6: Excitation spectrum of the ZnS:Mn nanoparticle dispersion after 90 minutes. The maximum at about 310 nm clearly indicates quantum size effect.  $\lambda_{em} = 585$  nm

In figure 6.6 the excitation spectrum of the particle dispersion after 90 minutes is shown. It's a peak that centres at about 310 nm, the wavelength of the absorption onset in the absorption spectrum. That the excitation spectrum has its maximum at a wavelength where there is nearly no absorption observable in

the absorption spectrum, could be due to the fact, that the two measurements have been made on different machines and that there is a calibration problem. The difference in recording the spectra for absorption and excitation spectra is that for absorption spectra one measures the absorption over a range of wavelengths in comparison with a reference in our case a cuvette with pure water. For an excitation spectrum one enters the emission wavelength one wants to observe and measures for which excitation wavelength this emission reaches its maximum intensity. For the spectrum in figure 6.6 the emission was set to 585 nm being the manganese emission wavelength. With excitation spectra no exciton peak is observable, but one sees very well the value for the band gap which is 310 nm in our case, and which clearly shows the quantum size effect.

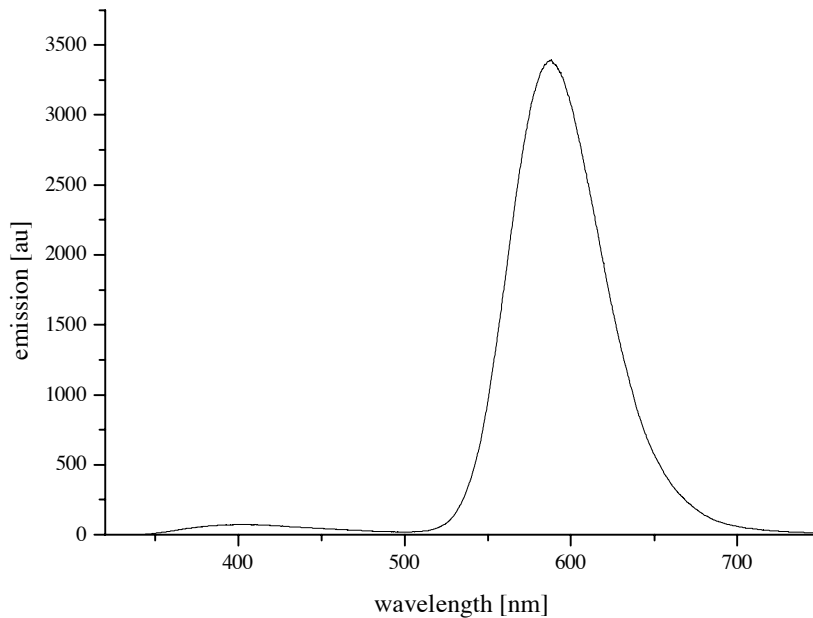


Figure 6.7: Emission spectrum for ZnS:Mn nanoparticles after a reaction time of 90 minutes. Peak at about 390 nm arises from recombination from surface defect states (see figure 3.6), peak at about 585 nm from transition within the manganese d-orbitals.

Figure 6.7 shows the photoluminescence spectrum of ZnS:Mn nanoparticles after a reaction time of 90 minutes. The sample was excited at 310 nm and shows an orange luminescence with a maximum at 585 nm which is characteristic for the  ${}^4T_1 \rightarrow {}^6A_1$  transition of  $Mn^{2+}$  ions in a crystalline ZnS-matrix [Gum81]. This orange emission can be seen with the bare eye when the sample is under excitation. Furthermore we observe a blue emission at about 390 nm. As pure band gap emission in our nanoparticles should be in the ultra violet, we suggest

in analogy with Murphy et al. [Soo96], that the emission is due to shallow electron traps acting as recombination centres for photogenerated charge carriers (see figure 3.6).

### 6.3 Synthesis parameters and particle size

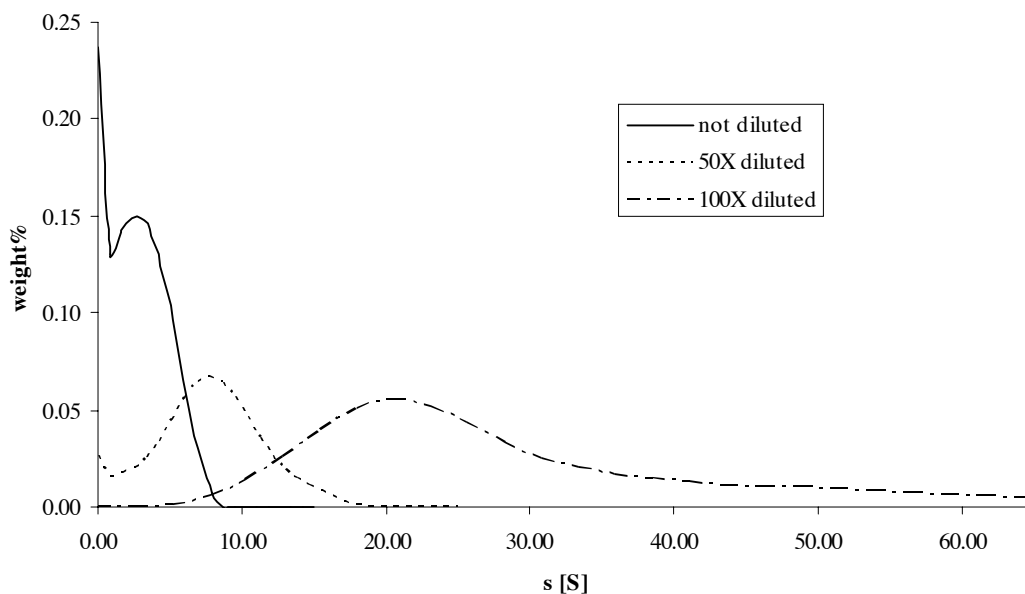


Figure 6.8:  $s$ -Distributions for different dilutions of the same sample showing how concentration influences the  $s$ -distributions in AUC measurements.

The influence of the synthesis parameters temperature, precursor ratio and concentration on the particle size distribution have been investigated using AUC and UV/vis absorption measurements. The AUC allows no direct conclusion on the size of the particle when the particle density is not known, but changes in the  $s$ -distribution correspond to changes in the particle size distribution (see section 5.1.1). The sedimentation coefficient  $s$  is a concentration dependant quantity [Bör00]. The concentration dependence from the increased viscosity of the dispersion at higher concentration [Ral93] and the fact that particles that are charged in the same way repel one another and thus produce a higher back diffusion and a shift to lower  $s$ - values for higher concentrations. This is shown in figure 6.8 where one can observe the shift of the  $s$ -distribution to lower  $s$  values with increasing particle concentration. Working at low concentrations where the particles do not "feel" the repulsion of one another, prevents this. Therefore, to obtain comparable results for different samples one has to work at the same concentration. To do this we diluted the samples to a value for the absorption of

the maximum of the exciton peak of 1.4, since the absorption between 0.5 and 1.5 is proportional to the concentration.

Shifts in the UV/vis spectra, like shifts in the s-distribution, indicate changes in particle size, but unlike the s-value the absorption does not shift due to particle agglomeration.

So for the investigations of the influence of the reaction parameters on the particle size, all parameters besides one were kept constant. The results for both the AUC and UV/vis measurements are shown in table 6.5. The values represent the maxima of the s-distributions from AUC measurements and the maxima of the absorption measurements.

Table 6.5: Influence of synthesis parameters on s-distribution and UV/vis spectrum

<b>Parameter</b>	<b>UV/vis</b>	<b>AUC</b>
<b>Temperature</b>		
RT	276 nm	13 S
40 °C	278 nm	16 S
50 °C	278 nm	15 S
60 °C	280 nm	22 S
<b>Zn<sup>2+</sup>/cysteine ratio</b>		
1:1	279 nm	20 S
1:1.25	279 nm	15 S
1:1.5	278 nm	15 S
1:1.75	277 nm	12 S
1:2	277 nm	13 S
<b>Concentration</b>		
1M	278 nm	15 S
0.5 M	278 nm	14 S
0.1 M	no particle formation	

For the UV-measurements we estimated an error of 0.5 nm from ten measurements performed on the same sample. For the AUC measurements 0.5 S. Even though these errors are big (see figure 6.9), the measurements allow still a statement on the development of the particle size with varying synthesis conditions. In figure 6.9 the UV and AUC values from table 6.5 are plotted. One can observe an increase of the UV values with increasing S-values, but there are large differences of the s-values for the same absorption wavelength. For example for 279 nm there is a s-value of 20 S and of 15 S, which represents a difference of 25 %. This is to a great part due to the fact that shifts to higher s-values represent not only the growth of bigger particles compared with smaller s-values, but also

agglomeration of the particles. So the values of 20 S and 22 S for 279 nm and 280 nm respectively indicate that in these cases there is particle agglomeration in addition to the growth of bigger particles, due to reaction conditions, present in the dispersion.

The values for different synthesis temperatures displayed in table 6.5, show an increase of particle size with reaction temperature. When the reaction mixture is not heated but held at room temperature, the maximum value for the s-distribution and the absorption spectra are the smallest. But without heating the white precipitate which precipitates first does not dissolve completely. This is also the case for 40 °C. From 50 °C on one hour of heating is sufficient to dissolve the precipitate and the values for s-distribution and absorption are the same as for 40 °C, but slightly higher as for the synthesis at room temperature.

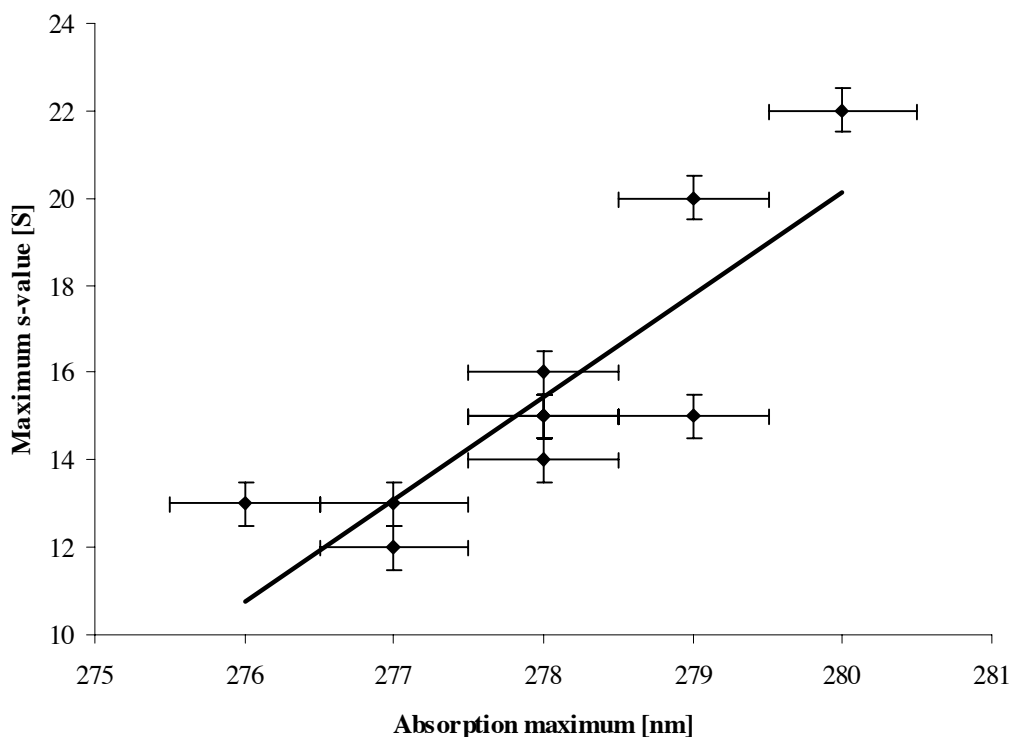


Figure 6.9: Plot of the maximum absorption wavelength and the corresponding S-values from AUC measurements. The values are represented in table 6.5.

From 60 °C on a shift to higher s- and absorptions values is observable. The shift of the absorbance maximum to higher wavelengths compared with lower temperatures indicates that the dispersions obtained at 60 °C consist of particles bigger than the one obtained with the synthesis carried out at lower temperatures. In picture 6.10 the s-distributions for room temperature, 40 °C and 60 °C can be seen. What is interesting to observe is the increased tailing of the

s-distributions, especially for the one at 60 °C. This indicates, that besides the growth of bigger particles, there is also a contribution to the increased s-value from particle agglomeration. The s value of 22 S for 280 nm for the maximum absorption, is high compared with a s-value of 15 S for a maximum absorption of 279 nm, this also indicates particle agglomeration like already mentioned above. It was explained in section 2.2.2 that it is difficult to electrostatically stabilize nanoparticle systems with sizes smaller than 10 nm. For these, in most cases metastable systems a small amount of energy is sufficient to overcome the energy barrier that stabilizes them. So the temperature difference between 50 and 60 °C can be sufficient to overcome the barrier and produce particle agglomeration. For the variation of the  $\text{Zn}^{2+}$  to cysteine ratio and with this the  $\text{S}^{2-}$  to cysteine ratio, one can see that a ratio of 1:1 is the lower limiting value. Already for this ratio of cysteine to  $\text{Zn}^{2+}$  in the reaction mixture agglomeration starts. This can be seen in figure 6.11 where the s-distribution for 1:1 is shifted to higher s-values compared with the two graphs for higher cysteine contents. That it is a matter of agglomeration and not particle growth can be seen in the fact, that the s-value increases but not the value for the absorption (see table 6.5 and figure 6.11).

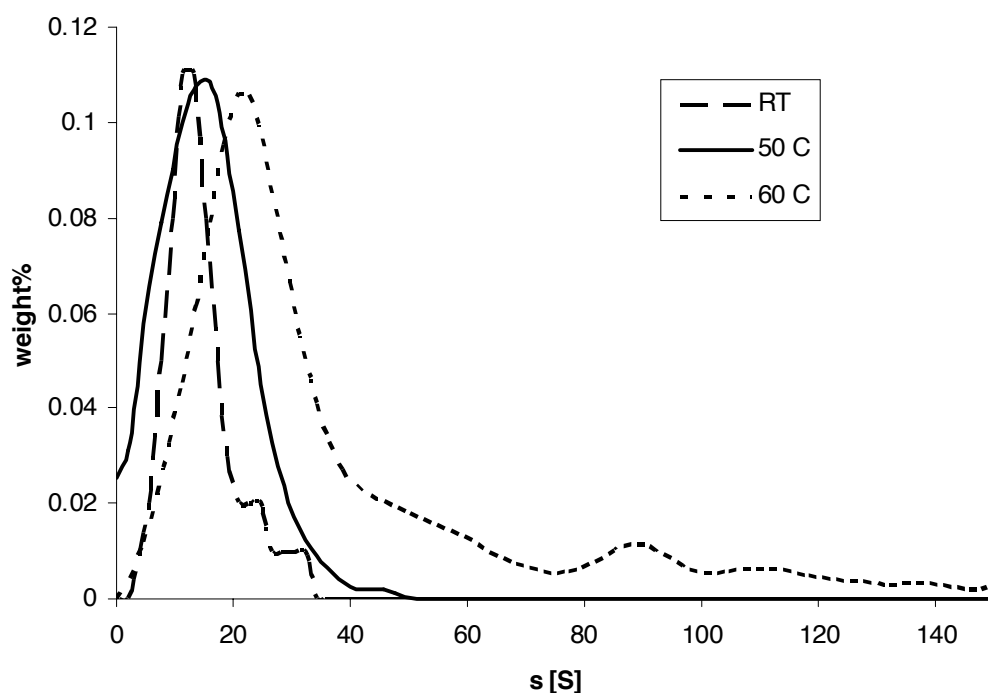


Figure 6.10: Variation of the s-distribution with reaction temperature.

For the ratios 1:1.25, 1.5, 1.75 and 2 there is not a lot of difference observable. But for 1:1.75 and 1:2 it gets difficult to dissolve the cysteine and cysteine precipitation in the dispersions can be observed after 2-3 days after particle synthesis.

The synthesis has also been carried out at three different concentrations. 1M, 0.5M and 0.1M with respect to the  $\text{ZnSO}_4$  and  $\text{Na}_2\text{S}$  concentrations. For the reaction at  $0.1 \frac{\text{mol}}{\text{l}}$  no particle formation was observable. For the reactions with 1M and 0.5M solutions no differences within the limits of the measuring techniques are observable (see table 6.5), so that we can conclude that the concentrations when changed for all reactants in the same order do not influence the particle size.

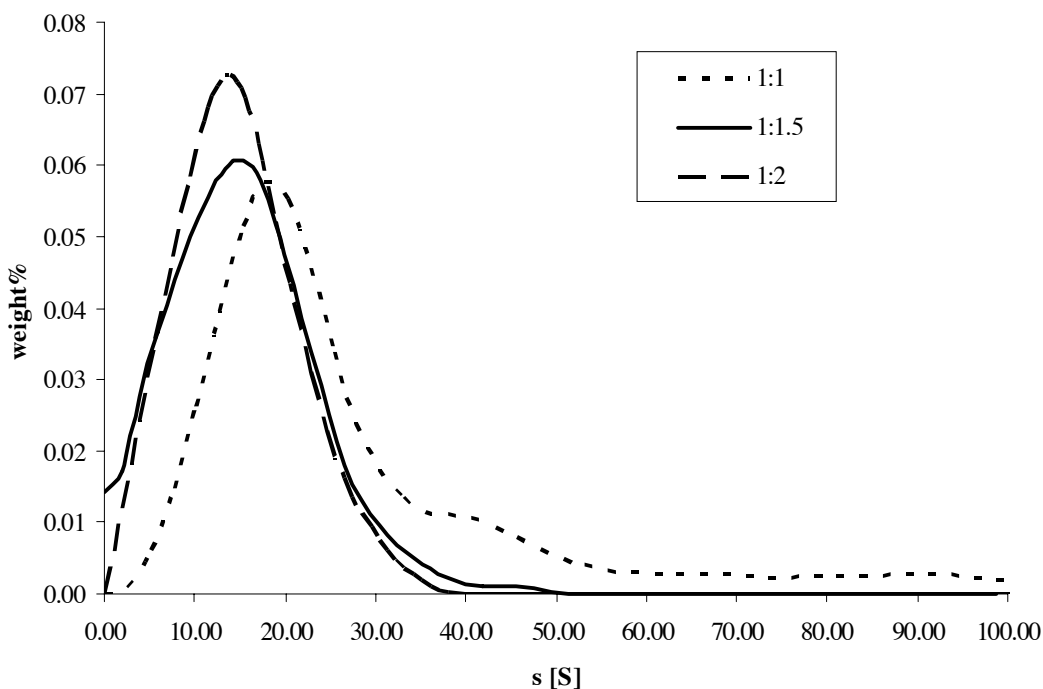


Figure 6.11: variation of the  $s$ -distribution with the  $\text{Zn}^{2+}$  to cysteine ratio

### 6.3.1 Stability over time

One of the goals of this work was the synthesis of dispersions stable for at least 2-3 weeks. Like it was already explained in section 6.1 the particles are not stable when the ionic strength is increased, since already small amounts of salt screen the stabilizing carboxylic groups at the particle surface. To get an idea of stability over time, AUC and absorption measurements were made over a period of 5 weeks.

In table 6.6 one can see the  $s$ - and absorption values for the suspension after two days, two weeks and five weeks. Further measurements were not possible because the particles flocculated. In figure 6.12 one can see the corresponding  $s$ -distributions. They show a shift to higher  $s$ -values with time, but the maximum



values for the corresponding UV/vis absorption spectra only show a shift of two nanometres. This indicates that particle growth in form of Ostwald ripening, where bigger particles grow at the expense of smaller ones, attributes only a small part to the shift in the s-distribution, and that we mainly observe particle agglomeration.

Table 6.6: Stability over time for a ZnS:Mn nanoparticle suspension.

Parameter	UV/vis	AUC
Stability		
2 days	276 nm	15 S
2 weeks	278 nm	20 S
5 weeks	278 nm	30 S

Since the particle growth with time indicated by the UV/vis maxima is only small, the increase of the sedimentation coefficients must mainly be due to agglomeration of the particles. The dispersions are electrostatically stabilized due to the surface charges of the cysteine.

It has been observed, that cysteine reprecipitates from solution after 3-4 days after solution preparation, that is the reason why the cysteine solutions were always freshly prepared for particle synthesis. A formation of the same needle shaped precipitate was observed for the dispersions after 1-2 weeks. This indicates, that the cysteine precipitates from the dispersion which leads a shift of the equilibrium between cysteine attached at the particle surface and free cysteine in solution. When free cysteine precipitates more attached cysteine goes in solution to balance the equilibrium. This leads to a smaller surface charge and so to agglomeration of the particles (see sections 2.2.2 and 6.1.3).

## 6.4 Cysteine adsorption

The stabilization of the particles in aqueous dispersion is achieved with L-cysteine (HOOC-CHNH<sub>2</sub>-CH<sub>2</sub>-SH) as surfactant. To investigate its attachment to the particle surface IR-spectroscopy and thermo gravimetric analysis (TGA) have been applied. The IR spectra of pure L-cysteine and L-cysteine adsorbed on the particle surface are shown in figure 6.13.

The most prominent peaks in the pure L-cysteine spectrum are listed in table 6.7. The presence of the bands for NH<sub>3</sub><sup>+</sup> and COO<sup>-</sup> indicates the zwitter ionic form for the dry cysteine powder. In the spectrum of cysteine adsorbed on the particle surface (powder freeze dried from dispersion at pH 11) no S-H stretching mode can be observed. At pH 11 the SH group is deprotonated (see table 6.1) but the SH band was not observed for powders isolated from dispersions at pH 8.5

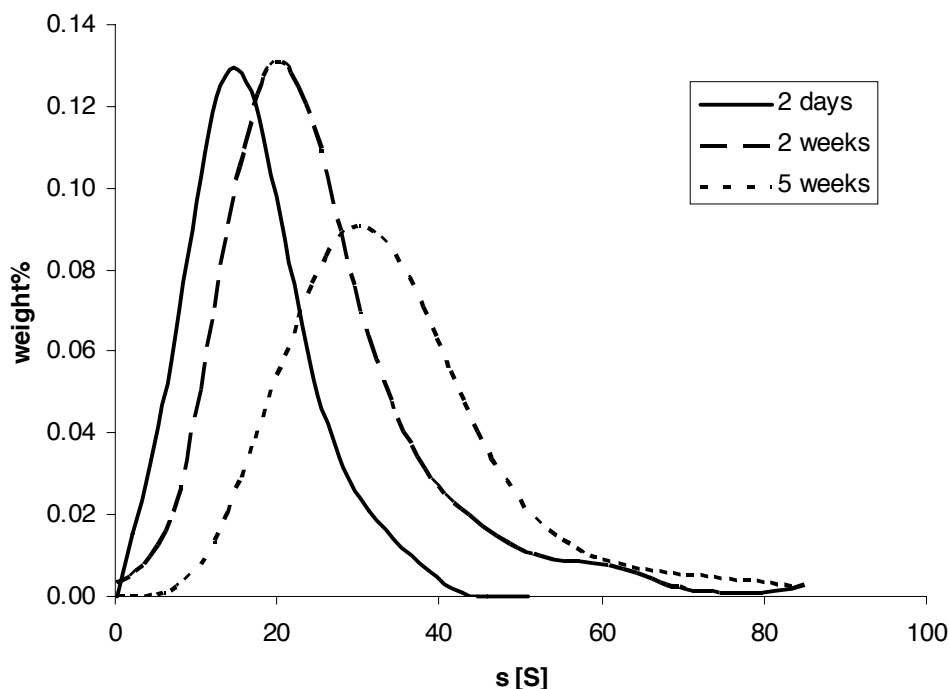


Figure 6.12: Variation of the  $s$ -distribution over time.

either. This in combination with the high affinity of the sulphur to ZnS indicates that bonding to the particle surface occurs through the mercapto group as has been observed for metal particle dispersion stabilized with mercapto surfactants. However, formation of disulphides cannot be excluded, since the formation of cysteine complexes with transition metal ions such as, for example, Cu (II) and Fe(II) is known to be complicated by the rapid oxidation of cysteine to cystine [Cav69, Gur56]. In the high frequency region of the IR-spectrum there is a broad absorption band around  $3250\text{ cm}^{-1}$ . This is where the asymmetric and symmetric stretching modes for a coordinated  $\text{NH}_2$  group are expected to absorb [His91]. This could indicate that the  $\text{NH}_2$  group does also interact with the particle surface, but one has to take into account that water also has a strong band in this region. In any case an interaction with the particle surface via the sulphur and the amino group would be favourable since this would lead to the formation of a chelate complex which is energetically very stable.

A TGA investigation of the powders showed, that the cysteine does not desorb in a single step but that a decomposition of the molecule takes place at the surface. To observe the decomposition and to see which molecule evaporates at which temperature, a TGA apparatus was coupled with an IR-spectrometer to take spectra of the evaporated molecules. The corresponding spectra can be seen in annex D. The assignments of the bands to the respective molecules are shown in table 6.8 [Wei88]. The first molecule detected is water which is adsorbed at the particle surface since the powders had been isolated from aqueous suspension. It

already evaporated at temperatures smaller than 100 °C. CO<sub>2</sub> can be observed in every spectrum. It can originate from the carboxylic group of the cysteine or from CO<sub>2</sub> adsorbed at the particle surface. At temperatures between 185-300 °C NH<sub>3</sub> evaporates and at the end between 560-915 °C SO<sub>2</sub>. Here one has to take into account that the SO<sub>2</sub> originates from the cysteine and the ZnS.

Table 6.7: Bands and their position for L-(+)-cysteine [Dal97]

Band	Position [cm <sup>-1</sup> ]
S-H stretch	2559
NH <sub>3</sub> <sup>+</sup> stretch	2090
COO <sup>-</sup> stretch	1581
NH <sub>3</sub> <sup>+</sup> deformation	1531

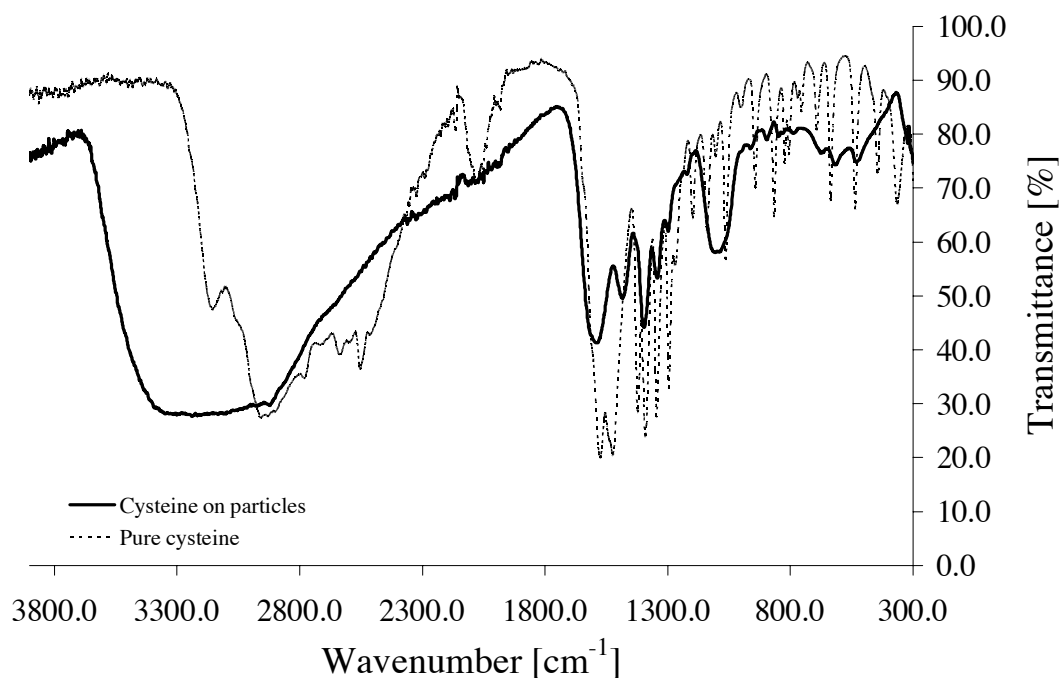


Figure 6.13: IR spectra of cysteine and cysteine adsorbed on the particle surface

Table 6.8: Detected molecules during TGA temperature program.

<b>t [min]</b>	<b>T [°C]</b>	<b>Molecule</b>
5-30	30-130	H <sub>2</sub> O (1600 cm <sup>-1</sup> , 3800 cm <sup>-1</sup> ) CO <sub>2</sub> (2350 cm <sup>-1</sup> , 677 cm <sup>-1</sup> )
30-36	150-180	CO <sub>2</sub> (2350 cm <sup>-1</sup> , 677 cm <sup>-1</sup> )
37-60	185-300	CO <sub>2</sub> (2350 cm <sup>-1</sup> , 677 cm <sup>-1</sup> ) NH <sub>3</sub> (944 cm <sup>-1</sup> )
60-110	300-550	CO <sub>2</sub> (2350 cm <sup>-1</sup> , 677 cm <sup>-1</sup> )
111-183	560-915	CO <sub>2</sub> (2350 cm <sup>-1</sup> , 677 cm <sup>-1</sup> ) SO <sub>2</sub> (1316 cm <sup>-1</sup> , 1150 cm <sup>-1</sup> , 528 cm <sup>-1</sup> )

The fact that the molecule decomposes rather than desorbs as a whole and the temperatures which are necessary for this indicate that the cysteine is covalently bound to the particle surface. The fact, that the SO<sub>2</sub> molecule evaporates last at temperatures higher than 500 °C confirms the assumption that the cysteine is attached to the surface via the sulphur atom. This could also explain why the dispersions are only stable in the pH range from 8-14. When the pH gets smaller the mercapto group of the cysteine is protonated and the cysteine can no longer stabilize the particles and flocculation starts.

## 6.5 Composition of the particles

Like already pointed out in chapter 4 no detailed investigation of nanoparticle composition has been carried out until now. In this work interest was concentrated on the ZnS to cysteine ratio in the samples. From 100 ml of dispersion 0.8 g of powder can be isolated, but this is not only ZnS but also the surfactant cysteine. To obtain this information, direct investigations of the Zn<sup>2+</sup> content via ICP and titration have been carried out. With CHNS analysis one can draw conclusion on the cysteine content in the sample.

To investigate the powder samples by means of ICP and titration, they are dissolved in acid (0,8 M HNO<sub>3</sub> for ICP measurements, and 5 M HCl for titration, see chapter 6.1.1) to obtain determinable ions. For the ICP measurements the sample solutions are compared with a 1 ppm Zn<sup>2+</sup> standard. The titration is a complex titration with EDTA as complexing agent, because the EDTA forms strong complexes with Zn<sup>2+</sup>. For measurement, first a eriochrome black T indicator solution is added to the Zn<sup>2+</sup> solution forming a red to violet complex with Zn<sup>2+</sup> and other metal ions. On the addition of EDTA first the free Zn<sup>2+</sup> is complexed by EDTA, then the Zn<sup>2+</sup> in the eriochrome complex is released to form the more stable, colourless EDTA complex. This can be observed by a change of colour from red/violet for the indicator with metal ion, to blue for

the free indicator. When the sample solution was completely blue the titration was finished and the  $\text{Zn}^{2+}$  content could be calculated with the amount of EDTA solution used.

The manganese content being very low compared to ZnS in the samples was not taken into account in these measurements, but will be determined in chapter 8.1. For the cysteine content CHNS analysis was applied. Here the sample is heated, and the amount of C, H, N and S leaving the sample is determined. The results for these methods are displayed in the following tables for powders precipitated with ethanol and powders from freeze drying. All represented values are average values over measurements for 7 powders.

Table 6.9:  $\text{Zn}^{2+}$  and ZnS content determined with ICP measurements and titration, *eth* indication powders isolated by ethanol separation and *fd* freeze dried powders.

Method	$\text{Zn}_{eth}^{2+}$ [wt%]	$\text{ZnS}_{eth}$ [wt%]	$\text{Zn}_{fd}^{2+}$ [wt%]	$\text{ZnS}_{fd}$ [wt%]
ICP	25	37	46	69
Titration	21	31	40	59

The results for titration and ICP measurements are displayed in table 6.9 with the index *eth* for powders isolated with ethanol and the index *fd* for the powders obtained by freeze drying. For both powders the titration results are lower than the results obtained with ICP measurements. This is probably due to the fact, that it is difficult to exactly determine the end point of the titration, because the colour changes not abruptly but gradually from violet to blue. ICP measurements are highly sensitive and are used for the determination of traces of elements in the region of ppm, so the ICP results are more reliable than the results obtained with titration. The ZnS content of freeze dried samples is higher than the one for the samples isolated with ethanol. The ethanol samples have not been dialysed for purification as the freeze dried ones, but isolated with ethanol and redispersed in water several times. So that there is less ZnS found in the ethanol samples indicating that there are more impurities left in the sample.

In tables 6.10 and 6.11 one can see the results of the CHNS analysis. Since the sum formula of cysteine is  $\text{C}_3\text{H}_7\text{O}_2\text{NS}$  there should be 3 mols of carbon for one mol of nitrogen, for seven mols of hydrogen, and so on. For the ethanol isolated powders the ratio between C and N is near to 3 (0.48 mol to 0.17 mol). The S and H values are too high related to N and C. Since the synthesis was made in water the H excess is probably due to water adsorbed at the particle surface.

Table 6.10: Results for CHNS analysis for ethanol isolated powders

	[wt%]	[mol%]	molar ratio with respect to N [mol]
<b>C</b>	5.7	0.48	2.9
<b>H</b>	1.6	1.6	9.1
<b>N</b>	2.4	0.17	1
<b>S</b>	21	0.66	4.1

Table 6.11: Results for CHNS analysis for freeze dried powders

	[wt%]	[mol%]	molar ratio with respect to N [mol]
<b>C</b>	6.5	0.54	3.6
<b>H</b>	0.8	0.8	5.3
<b>N</b>	2.1	0.15	1
<b>S</b>	20.7	0.64	4.2

Table 6.12: Water content calculated from hydrogen excess

<b>excess H</b>	
[mol%]	0.4
<b>H<sub>2</sub>O [mol%]</b>	0.2
<b>H<sub>2</sub>O [wt%]</b>	3.3

For the freeze dried powders no H excess is observable which is not surprising since the water is removed with a vacuum pump. The difference for the N to C ratio is higher than for the other powders (1 to 3.6 mol) and there is also more sulphur detected than is possible for the cysteine molecule.

During synthesis a excess of Na<sub>2</sub>S is used, so it is possible that this excess is still present in the sample, e.g. as S<sup>2-</sup> ions also adsorbed at the particle surface. With the H excess obtained with CHNS analysis assuming a sum formula of C<sub>3</sub>H<sub>7</sub>O<sub>2</sub>NS for cysteine, the weight percent of water present in the sample can be calculated to be an average of 3.3 wt% for the measured samples (see table 6.12).

Table 6.13: S excess calculated from CHNS analysis and ICP measurements

	<b>Ethanol</b>	<b>Freeze dried</b>
	<b>[wt%]</b>	<b>[wt%]</b>
<b>S in powder</b>	21	20.7
<b>S in cysteine</b>	5.4	4.8
<b>S in ZnS</b>	12 (ICP)	23
	10 (titr.)	19
<b>Excess S</b>	3.3 (ICP)	-7.1
	5.6 (titr.)	-3.1

The excess of S in the ethanol samples is 3.3 wt% when the value of S in ZnS is determined with the  $Zn^{2+}$  content obtained with ICP measurements and 5.4 wt% when determined with the results for titration (see table 6.13). For the freeze dried samples we see that there is not enough S in the sample. To calculate the S excess we take the wt% measured and subtract the S amount found for ICP and titration and the S for cysteine. So we assume that we oxidize the whole ZnS to ZnO and  $SO_2$ . If this is not the case, and after the CHNS analysis there is still some ZnS left and there is no S excess present in the sample, this would explain the negative results for the freeze dried S excess and suggest an even higher excess for the ethanol samples.

Table 6.14: Results for elemental analysis, ICP measurements and titration for the ethanol isolated powders

<b>ZnS</b>	<b>cysteine</b>	<b>H<sub>2</sub>O</b>	<b>S excess</b>
37 wt% (ICP)	20 wt%	3.3 wt%	3.3 wt% (ICP)
31 wt% (titr.)			5.4 wt% (titr.)
	64 wt%	36 wt%	unknown
	60 wt%	40 wt%	unknown

To investigate the cysteine content with another method, TGA measurements were carried out. Here the powder is heated from 30 to 900 °C. The weight loss observed during heating can be related to the cysteine evaporating from the surface. The TGA has also been coupled to an IR spectrometer and so IR spectra of the evaporating molecules could be recorded, clearly indicating that the weight loss is actually due to the cysteine evaporation. For TGA analysis we obtain an average weight loss of 28 wt% for ethanol isolated and freeze dried powders. This is higher than the result for the CHNS analysis (see table 6.14 and 6.15), but it cannot be excluded, that the  $SO_2$  evaporation at the end of the TGA is not only due to S in the cysteine but also to S coming from the ZnS when it starts to get oxidized.

Table 6.15: Results for elemental analysis, ICP measurements and titration for freeze dried powders

ZnS	cysteine	H <sub>2</sub> O	S excess
69 wt% (ICP)	18 wt%	0 wt%	0 wt% (ICP)
59 wt% (titr.)			0 wt% (titr.)
	87 wt%	13 wt%	unknown
	77 wt%	23 wt%	unknown

The elemental analysis combined with ICP measurements and titration can not fully explain the composition of the isolated powders. The addition of ZnS, cysteine, water and excess S for the ethanol powder only leads to 64 wt% for ICP measurements and 60 wt% for titration (see table 6.14). The unknown part of about 40 wt% is big and already indicates that other substances than the ones taken into account are present in the sample, and that isolation and redispersion is not sufficient to clean the dispersions. When the isolated powders are held into a flame, it gets fully orange, this indicates the presence of high amounts of sodium. Other contaminations could be sulphate and chloride ions.

For the freeze dried powder the results are better, there is no excess water and sulphur in the sample, but still there have to be impurities such as indicated above, present in the sample to explain the unknown rest of 13 and 23 wt% (see table 6.15).

Therefore, from the 8 g/l of powder that can be averagely isolated from the dispersions, one has to subtract up to 37 % of the weight to obtain the ZnS content, depending on the isolation method.

These results show that there are fewer impurities in freeze dried powders than in the one separated by ethanol addition. The freeze dried powders were dialysed prior to freeze drying, the ethanol powders have been purified by repeated washing with ethanol and redispersion in water. So dialysis is the more effective way to clean the dispersion and thou the powders. But even when dialysed there still rest considerable rests of impurities, so that other purification techniques, such as chromatographic methods, should be applied additionally to dialysis.



## 6.6 $\text{SiO}_2$ coated particles

To increase the fluorescence quantum yield and the stability of the particles a shell was synthesised around the particles. For the shell to be effective it has to consist of a higher band gap material, otherwise the shell and not the core would be excited. Another problem is the refractive index of the shell material. ZnS has a refractive index of 2.3 [Crc87], so any shell material with a refractive index higher than the one of ZnS would lead to a diffraction of the excitation light out of the particle. So a shell material with a refractive index lower than the one of ZnS is necessary.  $\text{SiO}_2$  as an insulator and with its refractive index of 1.5 is an ideal shell. Furthermore the  $\text{SiO}_2$  chemistry is well investigated which would be useful for a functionalization of the particles. Furthermore,  $\text{SiO}_2$  is known to form particles stable in the hole pH range.

When a shell is formed around the particles, the particle diameter should increase which should be observable in AUC measurements. In figure 6.15 one can see the s-distribution for the initial not coated particles and the dispersion after the coating step. What can be observed is, that the s-distribution for the coated particles is bimodal. There is one maximum for the s- values as for the initial dispersion, and then we have a long tail indicating big particle with a broad size distribution.

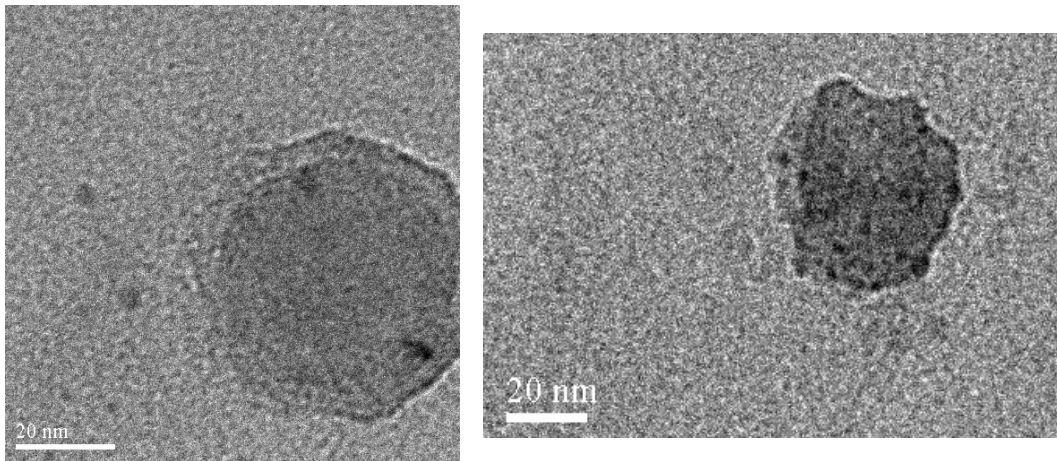


Figure 6.14: TEM micrograph of ZnS:Mn particles after coating step. Bar corresponds to 20 nm.

TEM micrographs (see figure 6.14) show the same fact. There are still free particles present in the sample, leading to the first peak in the s-distribution for the coated particles (see left picture in figure 6.14).

What can than be observed is that we do not have single particles coated by a  $\text{SiO}_2$  shell, but beads, that means several particles in one big  $\text{SiO}_2$  particle. The formed  $\text{SiO}_2$  particles have sizes from 20 to 80 nm.

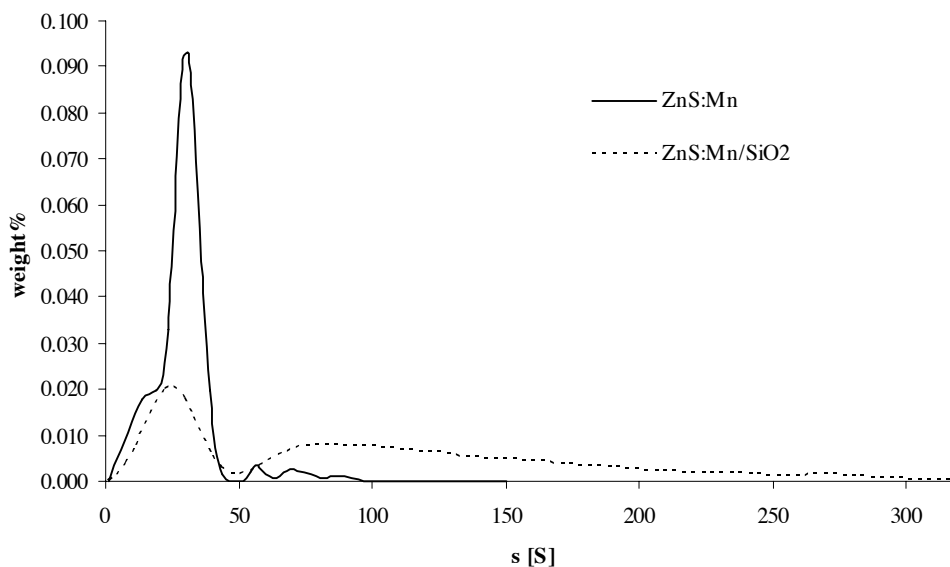


Figure 6.15: AUC measurements of the coated and not coated particles

When salts are added to dispersions of coated particles they still agglomerate. When the dispersions are freeze dried, the IR spectra still show the cysteine bands. This is probably due to the particles that are still free in the dispersion and cysteine in solution in the initial dispersion before the shell synthesis. In contrast to the sensibility to changes in the ionic strength, the shell does influence the stability over time. Not coated dispersions are normally stable 4-5 weeks, the coated dispersion have shown stability over a time of 6 month without showing flocculation and without altering their optical properties.

It was already mentioned, that the not coated particles have a zeta potential of about -55 mV. For the coated ones the value varies more for different batches but is between -55 mV and -60 mV. So the coating does not change the zeta potential significantly. So it is understandable, that small amounts of salt still lead to flocculation of the particles. What changes actually is the size of the particles. When it was said (see chapter 2.2.2) that particles of 5 nm and smaller are difficult to stabilize electrostatically because of a full overlapping of the double layers on contact, this is no longer the case, since we deal now with particles of sizes up to 80 nm. Therefore, there will only be a partial overlap of the double layers on contact. So the DVLO theory applies and the increased long term stability can be explained. The changes in the optical properties due to shell synthesis are discussed in chapter 8.1.4.

## 6.7 Conclusions and discussion

In this chapter the synthesis of ZnS:Mn nanoparticles and their coating with a SiO<sub>2</sub> shell has been described. Their surface characteristics, composition and the influence of the reaction parameters on the particle size have then been investigated. The reaction for the particle formation passes via an cysteine-Zn<sup>2+</sup> intermediate that precipitates first and then slowly dissolves with a change of pH, to form small ZnS:Mn nanoparticles in a controlled way. It has been shown, that the particle size is dependant on synthesis time and temperature, agglomeration is prevented by the cysteine and the concentration does not influence the particle size, when the concentrations are changed by the same factor for all reactants. Unlike the particle synthesis, the coating with a SiO<sub>2</sub> shell can not be controlled and instead of obtaining coated single particles, beads of particles in SiO<sub>2</sub> were obtained, with still not coated particles also present in the sample.

In the goals formulated for this work, it was asked to synthesize stable dispersions of doped ZnS nanoparticles with the possibility to functionalize the surface in a way to attach biomolecules, and to check on their composition.

For the stability we have to differentiate between the stability of the dispersion over time (the so called aging), and the stability due to changes in the ionic strength. Not coated particles are stable for 4-5 weeks before flocculation of the particles starts, but they are highly sensible to changes in the ionic strength, and immediately agglomerate, even by the addition of small amounts of a salt to the dispersion. This indicates electrostatic stabilization of the particles. The cysteine is negatively charged and so the particles repel each another. There is no steric stabilization possible since the cysteine is smaller then the electric double layer. The SiO<sub>2</sub> coating stabilizes the particles with respect to the stability over time. The zeta potential does not change due to shell formation, and so the particles show the same sensibility to changes in ionic strength like the not coated particles. That they are more stable over time can have to reasons. It was reported that it is difficult to stabilize particles smaller than 10 nm electrostatically since there should be a complete overlap of the double layers when two particles collide. The synthesized particles show stability over 3-4 weeks, so it is possible to stabilize the particles at least for that time, but the fact that they are only 3-4 weeks stable could be due to this total overlap. So that the coated particles are between 20-80 nm could add to their increased stability over time. Another reason could be that the cysteine coated particles are stabilized due to charges that come from a molecule at the surface that can be removed from the surface and precipitate with time, whereas the SiO<sub>2</sub> coated particles are stabilized due to real surface charges that come from the SiO<sub>2</sub>.

To know the composition of the particles, is first of all important to know the cysteine to ZnS ratio, because only when this is know the ZnS content in the dispersion can be estimated. This was determined with ICP measurements and titration for the ZnS and CHNS analysis for the cysteine for two different sets

of samples. One has been dialysed and freeze dried, the other powders were isolated by addition of ethanol to the samples and following centrifugation. This step was repeated several times to purify the so isolated samples. It has been seen that in addition to ZnS and cysteine, there must be water adsorbed on the particle surface, and that there is a sulphur excess present in the ethanol samples, but the complete composition of the precipitated powders could not be clarified. There is an unknown rest which is probably due to impurities like  $\text{Na}^+$ ,  $\text{Cl}^-$ , and  $\text{SO}_4^{2-}$ . That these impurities cannot completely be removed by dialysis and washing of the powders with water and ethanol, advises to look for other or additional possibilities to purify the samples, like e.g. chromatographic methods. The synthesized particles should be biocompatible. For this they need a surface that can be functionalized in a way to attach biomolecules. It was shown with IR spectroscopy that the cysteine is attached with the sulphur atom to the particle surface, and that the  $\text{NH}_2$  group also plays a role in the attachment, but that the carboxylic group is free and can be derivatized. Carboxylic groups react readily with a lot of molecules and are so ideal starting points for a biofunctionalization. What causes problems here is the instability of particles to salt addition. For a lot of reaction the pH has to be buffered, which leads to flocculation of the particles because of the high salt concentration in these buffers. Often the pH has to be acidic. This is not possible because the particles are only stable until pH 8, when the pH goes down further they agglomerate, either due to the change in ionic strength or the protonation of the mercapto group of the cysteine, or both. From a pH of 4 the ZnS starts to dissolve.

For the synthesized particles the surfactant cysteine opens the possibility for a biomodification of the particles, but the instability of the particles for small pH values and salt concentration makes this modification difficult, so ways have to be found to further stabilize them. The ratio of ZnS to cysteine in the powders could be determined, but the complete composition could not be clarified.

# Chapter 7

## Particle size measurements

One of the goals of this work was the synthesis of particle dispersion with a narrow size distribution. Since the quantum size effect is not used to obtain particles that emit at different wavelengths like for CdSe and CdTe, but different colours should be achieved by variation of the doping metal, an absolute control of the particle size is not necessary for this work.

On a bioassay there can be up to 400 detection spots on a area of 1 cm<sup>2</sup>. So detection is made on a spot in the micrometer range. A typical dye molecule like for example rhodamine or fluoresceine have diameters between 5 and 10 nm. So to replace these molecules by inorganic particles without changing the assay the particles should also be in this size range. Since it cannot be excluded that the particle size influences the attachment to the assay and the reaction with biomolecules, the size distribution should be narrow to guarantee comparable reaction conditions for every particle in the sample.

So the synthesized particles were investigated for their particle size. Since a lot of particle size measurements methods come to their detection limits for particles in the size region below 10 nm, different methods were used to get a correct image of the particle size.

### 7.1 Transmission electron microscopy

TEM and HRTEM images are surely the easiest way to get a first idea of the particle size. For this the samples were diluted by a factor of 200 and then a drop deposited on a copper grid. After evaporation of the solvent the particles were observable in the microscope. In figure 7.1 a TEM and high resolution TEM image can be seen. The TEM image at the left hand side shows several ZnS:Mn nanoparticles among these single particles and agglomerates. During the drying step for sample preparation the particles tend to agglomerate which makes it difficult to determine the size afterwards because it is often difficult to distinguish between a single particle and an agglomerate of two or three particles.

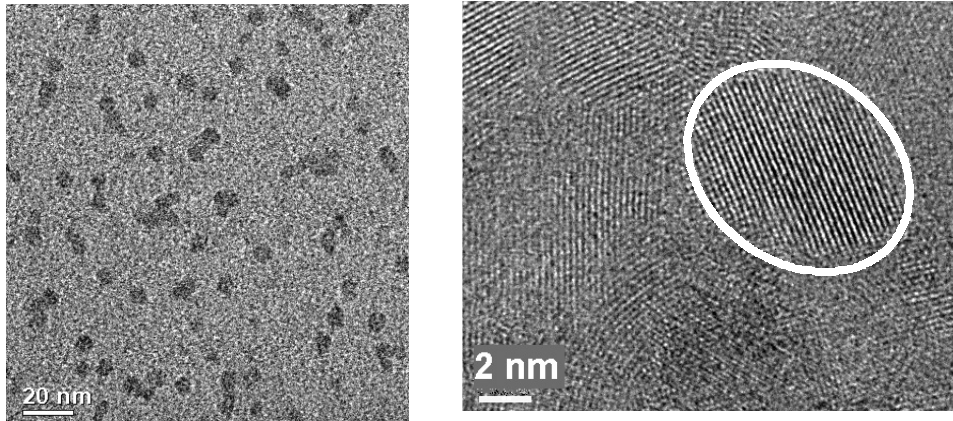


Figure 7.1: TEM and HRTEM of ZnS:Mn nanoparticles

Furthermore, it was observed that bigger particles are often placed at the outer rim of the sample and the smaller ones in the middle. This is also an artefact of the drying process. During drying the diameter of the drop gets smaller and at its edges the particles are deposited on the grid, with the biggest particles depositing first on the grid because of their higher mass. On the HRTEM image one can see a well defined particle with its lattice planes clearly visible.

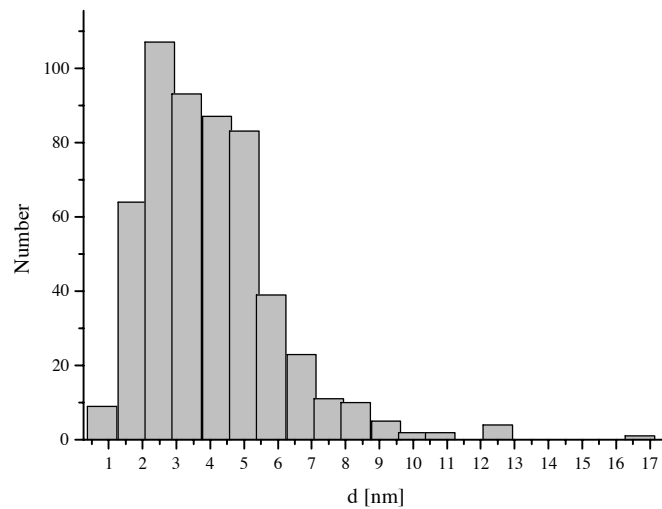


Figure 7.2: Particle size distributions for 540 particles from TEM images, represented in number.

In figure 7.2 and 7.3 one can see the particle size distributions for 540 counted and measured particles represented in number and volume. When there was a doubt about a particle being a single particle or agglomerate it was counted to be a single particle. The number weighted distribution goes from 1 to 17 nm with

92 % of the particles between 2 and 7 nm and the maximum at 2.5 nm.

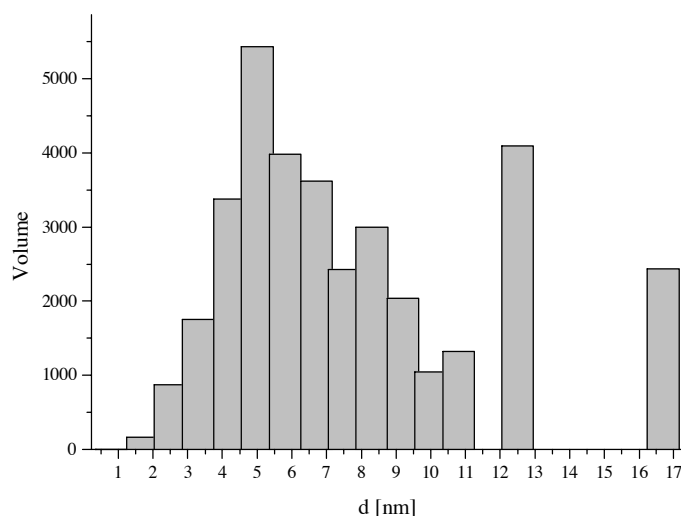


Figure 7.3: Particle size distributions for 540 particles from TEM images, represented in volume.

The volume weighted distribution goes from 2 to 17 nm with the two maxima at 5 and 12 nm and only 54 % of the particle volume between 2 and 7 nm. These two distributions are related by the relation  $V = \frac{3}{4} \cdot \pi \cdot \left(\frac{d}{2}\right)^3$ . The  $d^3$  dependence of the volume leads to the pronunciation of bigger particles in the volume weighted distribution. In which way particle size distribution measurements are presented normally depends on how they are measured. This example shows clearly that one has to pay attention when comparing particle size distributions measured with different methods, since the way of presentation influences the result.

## 7.2 X-ray diffraction

Like it has already been pointed out in section 5.3.1 the peak broadening of x-ray patterns can be used to calculate the crystallite size with Scherers equation. But this size corresponds to the size of perfect crystallites, so it cannot be compared to particle sizes obtained with other methods, but gives an idea of the size of the smallest unit of the crystals.

To calculate the crystal size with Scherers equation one needs the full width at half maximum of the diffraction peaks. One can do this manually with a ruler or use a software program. In this work the program *PowderCell for Windows Version 2.4* was used. First it calculates the background of the pattern and subtract from the spectrum, than it measures the full width at half maximum and calculates the crystal diameter with Scherers equation. The average value

for these calculations for diffraction patterns such as 6.2, gave a result of  $3.6 \pm 0.4$  nm.

### 7.3 Field flow fractionation

The field flow fractionation techniques are chromatographic techniques to determine the sizes of polymers, biomolecules or colloidal systems (see chapter 5.1.2). So the results obtained are chromatograms with retention times like it can be seen in figure 7.4. There is a first little peak at about 404 s and the main peak at about 520 s. The technique applied with our samples was the asymmetric flow FFF. For the measurement the sample is first focused in the channel, than the cross flow is started and the sample pressed to the accumulation wall without solvent flow. The start point of the measurement is when the solvent flow is started.

To get the particle size distribution out of the chromatogram, one has to know the channel symmetry, where the channel thickness is measured with ferritin as reference substance, the flow and cross flow rate and the retention time for a substance that is not retarded  $t_0$  (see equation 5.11). For this retention time  $t_0$  one uses the void time, that is the time the sample solvent needs to be eluted. The void peak is present in every chromatogram. In figure 7.4 it is the small peak at about 404 s, the main peak represents the eluted particles.

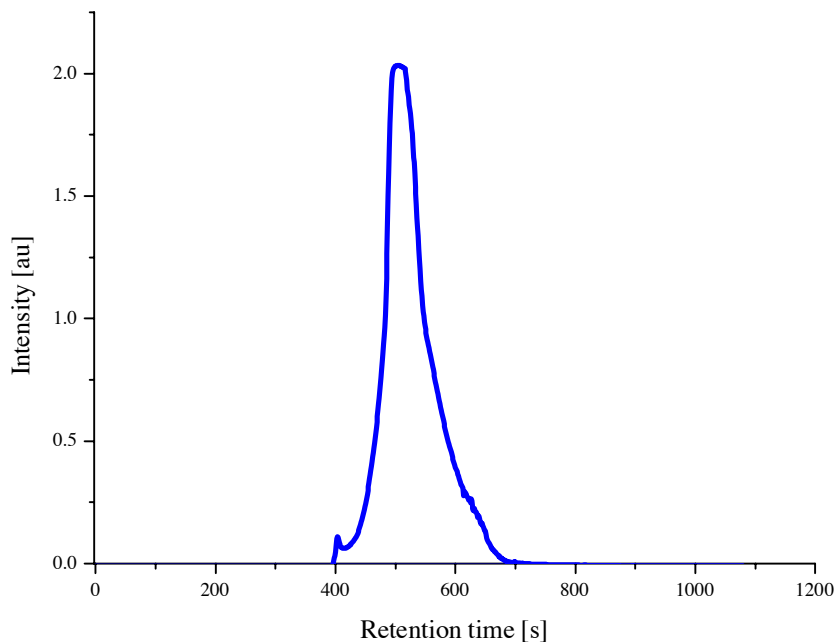


Figure 7.4: AF-FFF chromatogram of manganese doped ZnS nanoparticles



The particle size distribution obtained for the chromatogram in figure 7.4 can be seen in figure 7.5. The maximum of the distribution is at about 3.5 nm. Like for AUC measurements the surface charge of the particles can influence the result of the measurement. Since the particles are charged in the same way they repel one another when they get close. This is not a problem for low concentrations and for the AUC measurements this problem was solved by working at low and constant concentrations (see section 6.3). For aF-FFF measurements the sample is pressed with a solvent cross flow to the accumulation wall, so the particles get close and repel one another which pushes them in regions of the channel where the solvent flow is faster. This addition to the diffusion which normally is responsible for separation of sizes for this method, leads to particle size distributions shifted to smaller particle sizes compared to the actual particle size. To prevent this NaCl and TWEEN are normally added to the sample to be measured. The salt to screen the surface charges, the TWEEN to prevent agglomeration induced by the salt addition. Since our particles are already sensitive to very small changes in the ionic strength the TWEEN was not sufficient to stabilize the dispersions afterwards, so they were measured without NaCl.

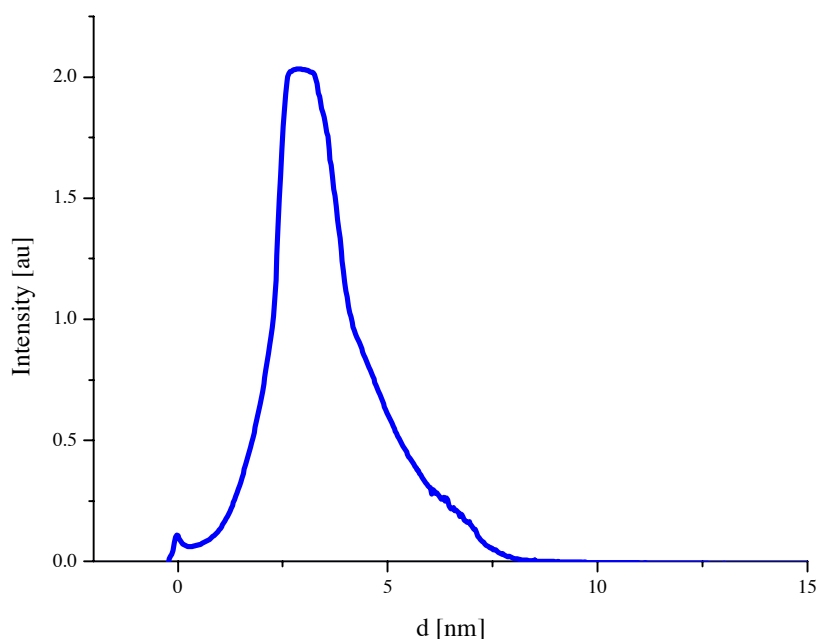


Figure 7.5: Particle size distribution obtained with aF-FFF.

The aF-FFF is a fast method to determine sizes of biomolecules, polymers and colloids, but surface charges can alter the sizes which has to be taken into account when comparing the results with sizes obtained with other techniques.

## 7.4 Photon correlation spectroscopy

The photon correlation spectroscopy or dynamic light scattering is a method which depends on the interaction of light with particles. The light scattered by colloidal particles in suspension, which undergo Brownian motion due to thermal agitation, will fluctuate with time and can be related to the diffusion coefficient  $D$  of the particle. This diffusion coefficient can then be related to a hydrodynamic diameter  $d_h$  by the Stokes - Einstein relation (see section 5.2). The hydrodynamic diameter is the diameter of the particle plus two times the double layer thickness. To think in terms of hydrodynamic diameters is especially important for small (2-300 nm) and highly charged particles where the electrical double layer will give a larger assigned diameter than measured by microscopy.

The method is particularly well suited for the measurement of narrow particle size distributions in the range of 2-500 nm. PCS is capable of measuring particle sizes down to 2-3 nm, but not with a low intensity laser and the preclusion of dust is imperative.

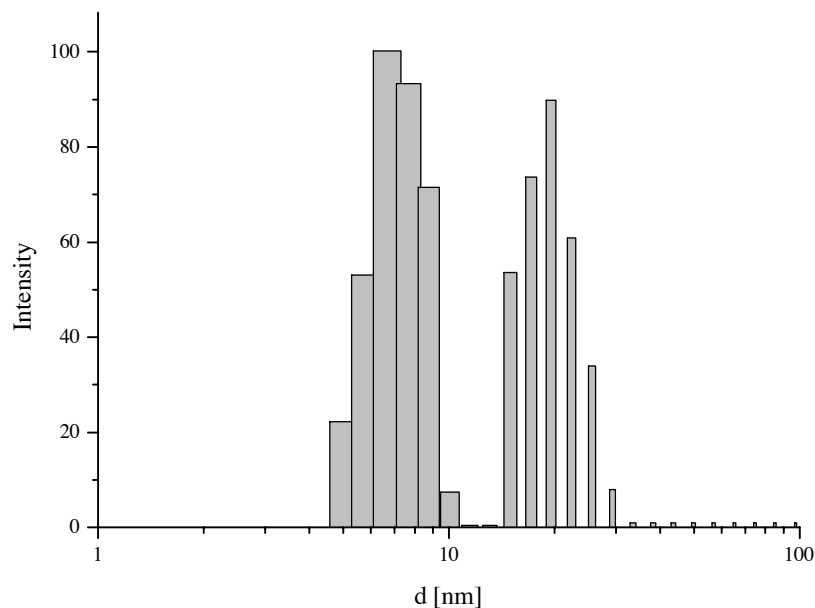


Figure 7.6: Intensity weighted particle size distribution of ZnS:Mn nanoparticles

The dependence of the scattered intensity on particle size is shown in equation 7.1, where  $I_0$  is the incident intensity,  $n_{rel} = \frac{n_p}{n_L}$  the relative index of refraction of a system of particles with the refractive index  $n_p$  in the suspending medium with the the refractive index  $n_L$ ,  $d$  is the particle diameter,  $\lambda$  the wavelength of light in the medium and  $H_{pd}$  the distance between the particle and the detector:

$$I_S = \frac{I_0 18\pi^4 d^6 ((n^2 - 1)(n^2 + 2))^2}{H_{pd}^2 \lambda^4} \quad (7.1)$$

This  $d^6$  dependence leads to an enhancement of the Intensity for bigger particles. A particle only twice the size will give 64 times the intensity. Consequently for systems where dust and agglomerates may be present one must be very careful about interpreting PCS results.

Two different set ups have been used to measure the synthesized particles. One was the Brookhaven zetaPALS zeta potential analyser and the other was a house made set up of the group of Scheffold at the University of Fribourg. With the Brookhaven apparatus it is possible to obtain particle size distributions. For this the average diffusion coefficient and the polydispersity index obtained from the auto correlation function must undergo a Laplace transformation. With the Brookhaven instrument it was difficult to measure the synthesized dispersions. Dust and probably also agglomerates present in the sample made data acquisition difficult and often the software was not able to calculate a distribution.

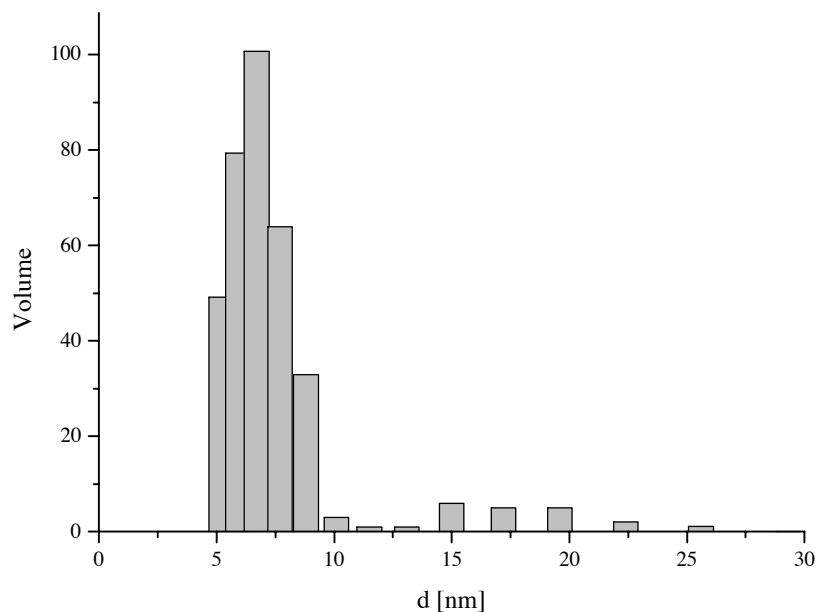


Figure 7.7: Volume weighted particle size distribution of ZnS:Mn nanoparticles

To overcome this problem, and to obtain at least an idea of the size of the primary particles, the dispersions were centrifuged for 15 min at 5000 rpm to get rid of dust present in the sample. Of course this will also eliminate big agglomerates and thus alter the initial particle size distribution.

In figure 7.6, 7.8 and 7.7 one can see three different ways of presentation of the

obtained particle size distribution. Intensity, volume and number weighted. One can see that the particle sizes between 10 and 30 nm in figure 7.7 which represents the volume weighted distribution is more pronounced in the intensity weighted one of figure 7.6. They even present intensity as high as the one for the particles between 2 and 10 nm. In the number weighted distribution (figure 7.8) they are almost not observable. This clearly shows the importance to take note of the way of presentation of such distributions.

For the dispersions measured the results presented here are representative. We obtain maxima of the PDS (particle size distribution) of 7 nm for the first and 20 nm for the second maximum for the intensity weighted, 7 nm and 15 nm for the volume weighted and 6 nm for the number weighted distribution (see also table 7.2).

The apparatus used at the University of Fribourg uses an analysis method that is known as cumulant method, that means no Laplace transformation is made but the method delivers an average value for the diffusion coefficient and with that for the particle size, and a value for the polydispersity index. The measurements were taken out at angles from  $20^\circ$  to  $90^\circ$ , which does not alter the result which is expected for Raleigh scatterers, that means particles much smaller than the wavelength of the incident light. Also here the dispersions were centrifuged. The measurements resulted in an average of 5 nm for the particles measured.

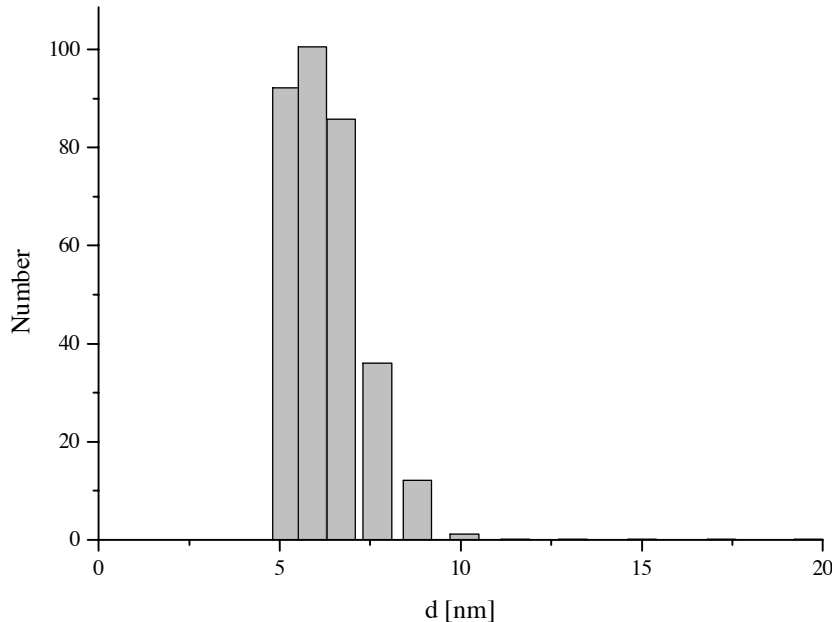


Figure 7.8: Number weighted particle size distribution of ZnS:Mn nanoparticles

PCS is a rapid analysis method which is ideal for narrow distributions. If a certain polydispersity is registered the cumulant method is no longer applicable, and a method that can display the actual distribution must be used. But also there one has to pay attention on the way of presentation, and the results should be compared with other methods such as microscopy.

## 7.5 Analytical ultra centrifugation

Analytical ultra centrifugation is a separation technique where the separation takes place in a centrifugal field and is due to the particle size and the density difference between particles and solvent (section 5.1.1). As a result of such a measurement one obtains a sedimentation coefficient distribution that can be transformed into a particle size distribution when the viscosity and density of the dispersing medium and the density of the particles is known (see equation 5.9). Since the dispersions measured consist not only of pure ZnS particles dispersed in water, but of cysteine stabilized particles, the bulk value for the density cannot be used to calculate the size distribution. Furthermore, it is unlikely that the density of nanoparticles in water, even without a stabilizing agent, is the same as for the bulk solid (4.1 kg/l [Crc87]).

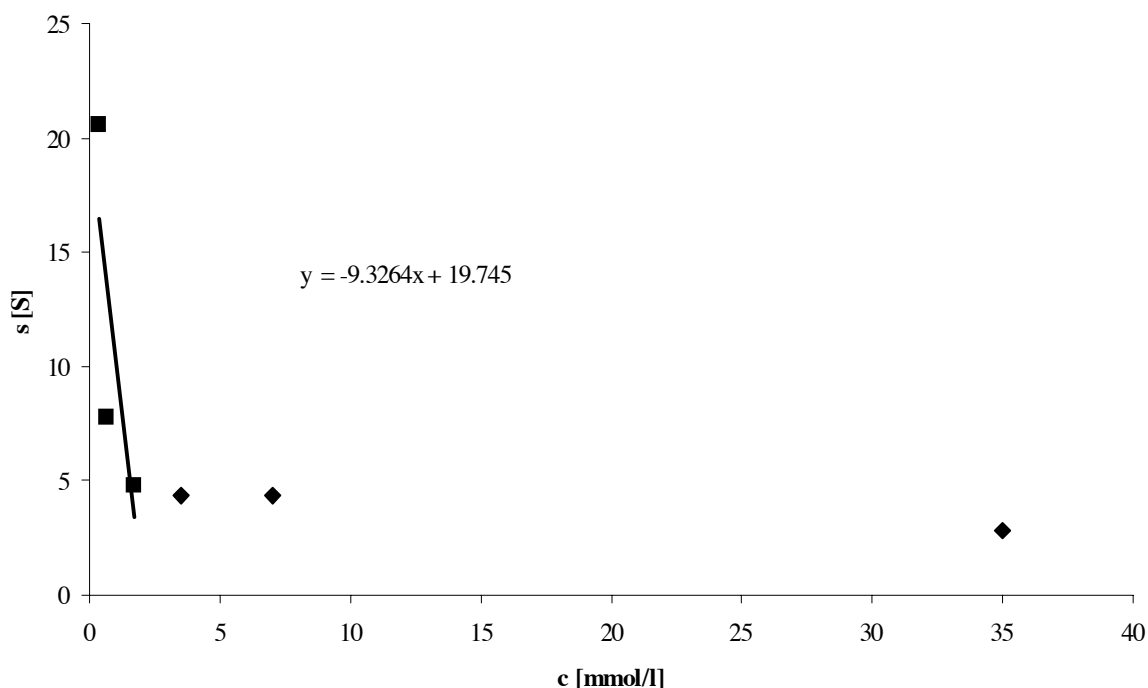


Figure 7.9: Plot according to equation 7.3. The extrapolation to obtain  $s^0$  was made for the three most diluted values.

To already see the influence of the surfactant on the powder density, density measurements with a helium pycnometer have been taken out for the freeze dried powders and the powders precipitated with ethanol.

This resulted in an average density of 3.6 kg/l for the freeze dried and 3.2 kg/l for the ethanol powders. One can observe in the density difference the effect due to freeze drying described in section 6.1.2, that the high capillary forces weld the particles together and lead to non dispersible powders, and, like it can be seen now, also to powders with higher densities compared with the powders isolated with ethanol.

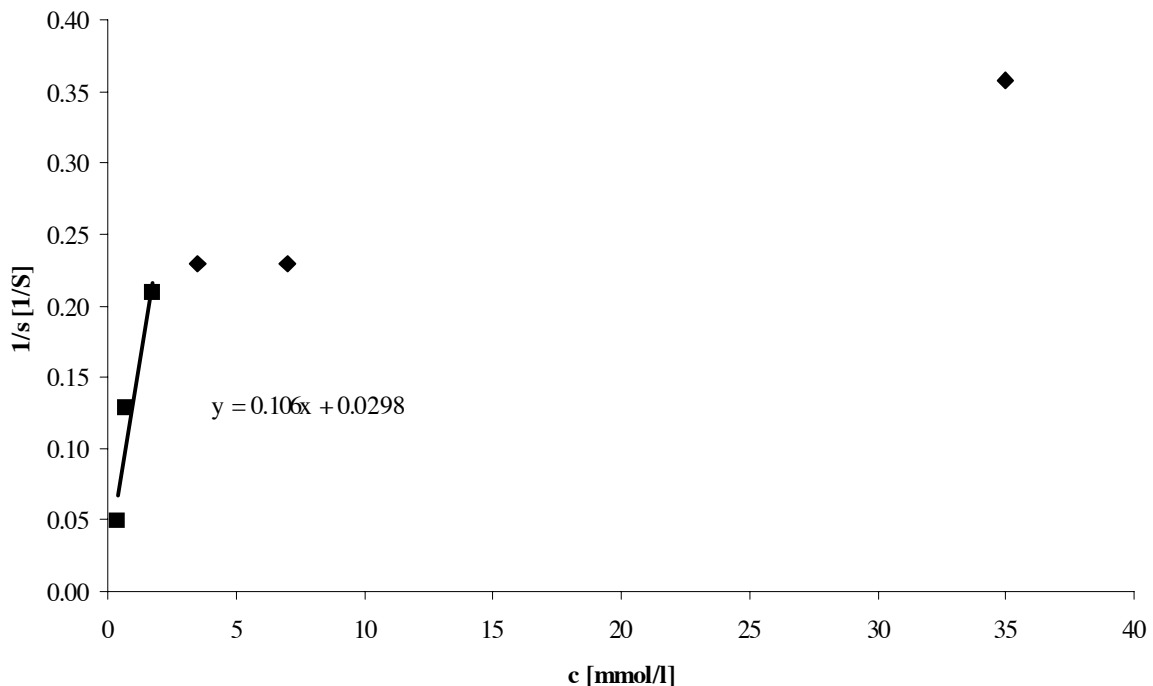


Figure 7.10: Plot according to equation 7.4. The extrapolation to obtain  $s^0$  was made for the three most diluted values.

As it has already been pointed out in section 6.3 and as it can be seen in figure 6.8 the sedimentation is concentration dependent. For comparative measurements it is sufficient to always work at the same concentration to obtain comparable results and so eliminate the concentration dependence, but this is not the case when one changes to particle size distributions. When the concentration is not small enough we will still have the concentration effect, that will shift our particle size to smaller values compared with lower concentrations. This shift will always be the same when one works at constant concentrations, but one does not obtain the real particle size.

From this problem follows the custom for AUC measurements to extrapolate  $s$ -values, measured of necessity at finite concentration, to infinite dilution to give

the extrapolated value  $s^0$ . The concentration dependence has been determined to be [Ral93]

$$s = \frac{s^0}{(1 + k_s \cdot c)}. \quad (7.2)$$

It has been seen experimentally that at least for monodispersed, non-interacting solutes, the approach to the  $c=0$  ordinate is not asymptotic. For the purpose of extrapolation it has been assumed that for small concentrations either

$$s = s^0(1 - k_s \cdot c) \quad (7.3)$$

or

$$\frac{1}{s} = \frac{1}{s^0}(1 + k_s \cdot c) \quad (7.4)$$

is linear to an adequate extent in  $c$  [Har92].

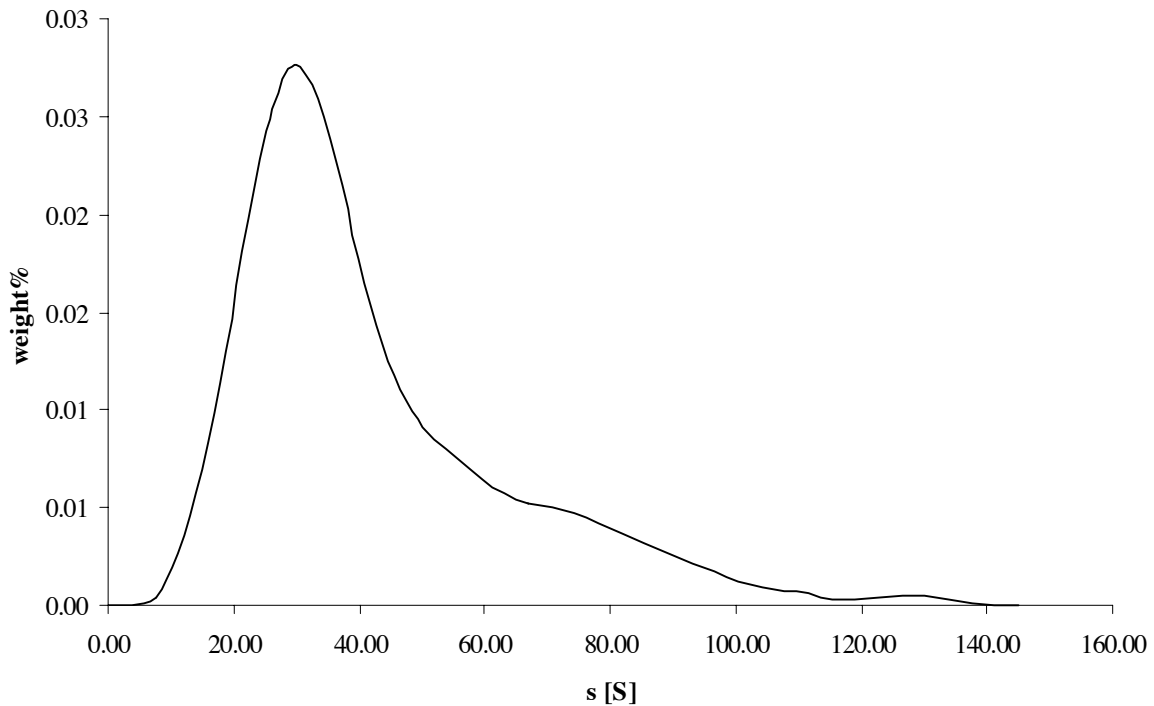


Figure 7.11:  $s$ -distribution of a ZnS:Mn nanoparticle dispersion.

From the point of view of laboratory practice, it is accepted that especially for solutes of high particle asymmetry the reciprocal plot (see equation 7.4 and figure 7.10) is linear in a wider range in  $c$  than the direct plot (see equation 7.3), but for compact, near-spherical particles this linear plot (see equation 7.3 and

figure 7.9) is as good and may be preferable [Har93].

Measurements for different particle concentrations for the same dispersion have been made and the sedimentation coefficients been plotted according to equation 7.3 and 7.4. In figure 7.9 one can see the direct plot according to equation 7.3. The extrapolation was made for the three smallest concentrations, which seem sufficiently linear to extrapolate. This leads to a value of  $s^0=18$  S. For the reciprocal plot (figure 7.10) the extrapolation leads to a value of  $s^0=33.5$  S.

The  $s$  value obtained for the maximum dilution is 23 S so already higher than the  $s^0$  value for infinite dilution obtained with the extrapolation for the direct plot (see figure 7.9). So the extrapolation for the reciprocal plot seems to be better for our system. The  $s$ -distribution for the highest dilution and thus lowest concentration has its maximum at 23 S. We multiplied the  $s$  values for this distribution by a factor of 1.45 to obtain a  $s$ -distribution with its maximum at 33.5 S, but the same form as the original one. This "extrapolated" distribution can be seen in figure 7.11.

To calculate a particle size distribution from this one has to know the particle density. The results of 3.6 and 3.2 g/ml obtained for the isolated powders show already that the density is smaller than the bulk value. Since these densities correspond to the powders we suppose, that the actual particle density in dispersion where the particles are additionally hydrated should be smaller than the values obtained for the powders. The result for a calculated particle size distribution with the value of 3.2 g/ml for the ethanol separated powders can be seen in figure 7.12. The distribution has its maximum at about 5 nm. If we assume that the actual particle density in dispersion is smaller than 3.2 g/ml, the distribution is shifted to higher particles sizes. To shift it by 1 nm one has to calculate with a density of 2.5 g/ml.

The particle sizes obtained after extrapolation of AUC measurements at different concentrations are dependent on the particle density used for the size calculation. Since we suppose the density to be smaller than the values measured for the synthesized powder and since for a shift of 1 nm for the particle size it needs a difference in density of 0.7 g/ml, we think that a maximum value for the particle size distribution of 5-6 nm is realistic. This is also a value which is in good accordance with the results from the other measurements.

AUC measurements are a fast method to first of all observe changes in the  $s$ -distribution and with this in the particle size distribution, but if a good estimation of the size is wanted several measurements at different concentrations have to be carried out and extrapolated to infinite dilution. To finally get a size one also has to have at least a range of the particle density in dispersion.

The advantages of this method are that the UV detector detects selectively the particles and that the results are so not influenced by impurities present in the samples.



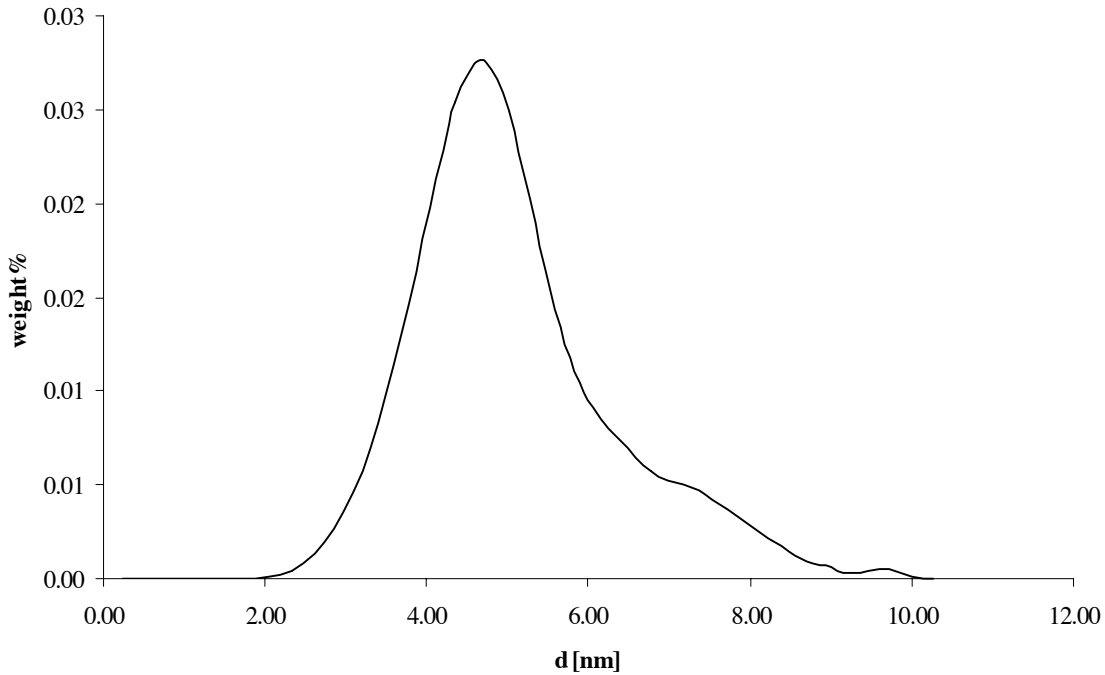


Figure 7.12: Particle size distribution obtained with s distribution in figure 7.11

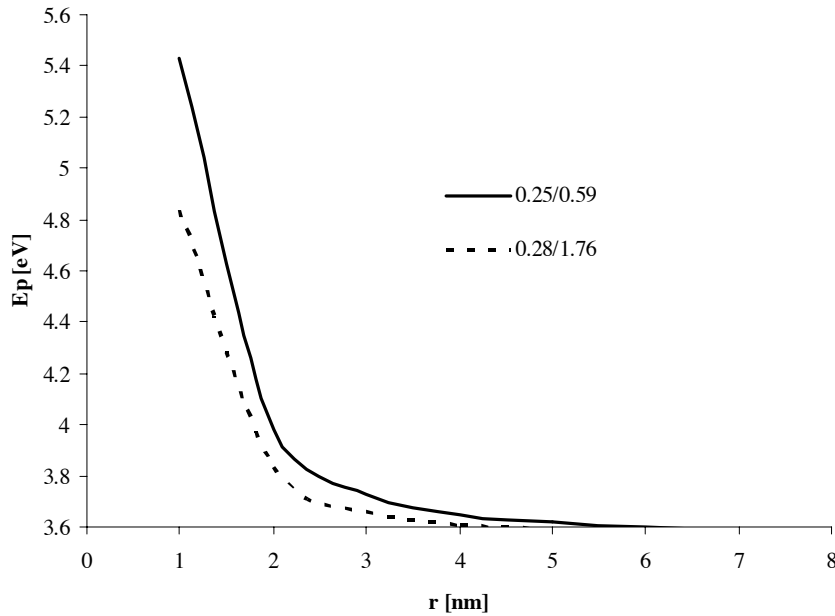
## 7.6 Optical diameter

Since the band gap of semiconductor nanocrystals shift to higher energies with decreasing size and this can be quantized with equation 2.29 it is possible to calculate the optical particle size with the band gap absorption from absorption spectra. To do this, one has to know the bulk band gap, the relative permittivity (relative dielectric constant) of the semiconductor and the values for the effective masses of the electron and the hole. The bulk band gap is known to be 342 nm or 3.6 eV [Gum81], values for the relative permittivity of ZnS found in literature vary from 8.3 to 8.7 [Soo96, Sun99, Ber63, Ate03]. This variation of the relative permittivity does not much influence the plot particle radius versus band gap energy, so we just calculated with a value of 8.5. The values for the effective masses of the electron and the hole found in literature are also very different. In table 7.1 the found values are listed with their references. For better clarity not  $m_e^*$  and  $m_h^*$  but  $m_e$  and  $m_h$  ( $m_{e/h}^* = m_{e/h} \cdot m_0$ ) values are given.

When different values for the masses of the electron and the hole are introduced in equation 2.29, a shift of the particle radius for which the band gap becomes the bulk band gap, is observable. This is demonstrated in figure 7.13 for the pairs  $m_e/m_h = 0.25/0.59$  and  $0.28/1.76$ .

Table 7.1: Literature values for the effective masses of the electron and the hole for ZnS.

$m_e$	$m_h$	$a_B$ [nm]	Reference
0.42	0.61	1.8	[Lip89]
0.25	0.59	2.6	[Bru83, Ros84, Soo96]
0.34	0.58	2.1	[Wan91]
0.28	1.76	1.9	[Ave67]
0.39			[Law71]

Figure 7.13: Plot of equation 2.29 for two  $m_e/m_h$  pairs

The values for the exciton Bohr radius found in literature vary from 2.2 to 2.5 nm [Buh03, Ros85, Bha94/2]. It is related with the effective masses via equation 2.26. With this relation the exciton Bohr radii shown in table 7.1 have been calculated. The values of 2.1 and 2.6 nm are closest to the values cited in literature. It is interesting to see that the exciton Bohr radii calculated with the effective mass approximation do not represent the values where the plots in figure 7.13 get to the bulk value of the band gap, but the point when the plot have a knee from a first slow increase to a steeper slope. So with the effective mass approximation the band gap already shifts when the particle radius gets near the Bohr radii but is not yet smaller. The value at which the band gap begins to widen is surly not a discreet one, but it will start when the particle size

gets in the region of the exciton Bohr radius, that means when the exciton starts to feel the spatial confinement. Nevertheless, one should not forget that we talk about a mathematical approximation that has its limitations [Lip89]. So it can for example not be excluded, that the values for  $m_e^*$ ,  $m_h^*$  and  $\varepsilon_r$  also change with particle size [Hen89, Wan87].

To estimate the particle size of our particles from absorption spectra we chose the values of 0.25/0.59 for the electron/hole pair. The onset of absorption of our absorption spectra and the maximum of the excitation spectra is at 310 nm which corresponds to 4 eV. With equation 2.29 we obtain a particle radius of 2 nm so a diameter of 4 nm which corresponds rather well with the results obtained with the other methods applied.

## 7.7 Conclusions and discussion

Table 7.2: Summary of the results obtained for the different particle sizing methods applied. The error for TEM corresponds to the accuracy possible for the size determination with a ruler, the error for AUC measurements corresponds to the error introduced by the unknown particle density, the error for the XRD was calculated by the software used.

Particle size [nm]				
	Intensity	Volume	Number	Weight
<b>TEM</b>		1. Max. $5.5 \pm 2$ , 2. Max $17 \pm 2$	1. Max. $2.5 \pm 2$	
<b>XRD</b>			$3.6 \pm 0.4$	
<b>PCS</b>	1. Max. 7, 2. Max. 20	1. Max. 7 2. Max. 15	6	
<b>aF-FFF</b>		3.5		
<b>AUC</b>				$5 \pm 2$
<b>opt. diameter</b>			4	

In the last chapter different methods to measure particle size distributions and estimate particle sizes have been presented. The results for these methods can be seen in table 7.2.

TEM images have the advantage that one actually sees the particles but, because of the resolution of the microscope it is sometimes difficult to differentiate between single particles and small agglomerates. To obtain a particle size distribution with TEM micrographs the particles have been measured with a ruler, so this is also a source of error for the result obtained by TEM.

With the hydrodynamic methods like aF-FFF and AUC the charge of the parti-

cles causes problems. For the aF-FFF measurements the repulsion between the particles add to the diffusion against the cross flow, leading to smaller sizes than the actual particle size. In the AUC this repulsion and the increase of dispersion viscosity lead to a slower sedimentation and so to a concentration dependence of the results for a certain concentration range. To overcome this an extrapolation to infinite dilutions has to be made. Another problem is the density of the particles. Since the AUC measures hydrodynamic diameters and the particles are coated with cysteine, the bulk density cannot be used to transform the  $s$ - to a  $d$ -distribution. So a density has to be estimated. For both, the aF-FFF and the AUC measurements, the particles were selectively detected with a UV/vis detector, so one can be sure that the results obtained are only due to the particles.

For the PCS this is not the case. Here everything that scatters the light is within the results, so this method demands very pure samples, because even dust adds to the measured variation in the intensity of the light. To overcome this problem the particle dispersion have been centrifuged to get rid of dust.

With the results from x-ray diffraction one has to pay attention, since there are a lot of restrictions for the results of these measurements. The measured crystallites do not represent the particles. A particle can consist of several crystallites and also amorphous parts can be present that cannot be detected with x-ray diffraction.

From the mentioned methods the AUC, aF-FFF and the PCS measure hydrodynamic particle sizes. Hydrodynamic diameter means, that the result corresponds to the particle size plus two times the double layer thickness. To check on this influence the dispersions have been dialysed against and diluted for measurement with 0.01M NaOH. This should result in a double layer with a thickness of 3 nm. So normally we should subtract 6 nm from our measured particle size. This would lead to negative or really small particle sizes. In any way this would lead to sizes considerably smaller than what was seen with TEM. This could be due to the fact that two times the double layer thickness equals or even exceeds the actual particle size. It is possible, that these hydrodynamic methods do measure the actual particle size since the double layer is too thick compared with the particles. So for all the applied measurements one has to be conscious of their limitations to estimate a particle size.

The highest particle size was obtained with PCS measurements. We will concentrate on the volume presentation of the results, because it is the most comparable with the results from other techniques. The distribution shows its first maximum at about 7 nm but has still observable signals for sizes up to 20 nm. To obtain a signal the samples have to be centrifuged to get rid of dust present in the sample, so it can not be excluded that agglomerates and particles bigger than 20 nm have been eliminated. Particle sizes up to 20 nm have also been observed with the TEM images but there it seems to be agglomerates rather than single particles. Since the PCS measurement are very sensible to impurities in the sample and since bigger particles are emphasized by a volume presentation compared to

number presentations, the PCS results have to be seen as an upper limit for the particle size.

With a maximum of the particle size distribution of 3.5 nm the distributions obtained with aF-FFF measurements represent the smallest value obtained for the particle size of the samples. Here we have the problem, that charged particles have the tendency to elute faster than they would without the charge, so that the particle size distributions obtained with this method are likely to be shifted to smaller sizes compared with the actual size we are looking for. In contrary to the PCS and TEM measurements no second maximum was observed. The channel width is normally in the range of 0.2 mm so it is not likely, that particles cannot pass it, but it is quite possible that we do not observe a second maximum because the measurements were stopped before they could elute. The measurements made were all stopped after retention times that correspond to sizes of 15-20 nm, so that it is possible, that agglomerates and bigger particles were cut from the distribution.

With the measurements made we draw the conclusion that the particle size distribution has its maximum between the PCS and the aF-FFF and x-ray maximal values. The signal for higher particle sizes obtained with PCS and TEM, can also be observed with AUC measurements. The particle size distribution shown in figure 7.12 has a tailing until 10 nm, but one has to keep in mind that we are talking of a particle size distribution obtained with a density for the particles in powder form and not in dispersion. So the tailing would shift to higher particle sizes with decreasing particle density. When there are agglomerates or particles present in the sample with sizes much bigger than the particles of the main distribution, it is likely, that they already sedimented during the acceleration of the centrifuge and the calibration of the detector which takes about 2-3 minutes.

Finally, the result obtained with the TEM micrographs, that show a maximum for the volume weighted distribution at 5 nm and a distribution from 2-10 nm with more peaks at about 13 and 17 nm, seems to be a good approximation for the actual particle size distribution of the dispersions.

As it can be seen in table 7.2, the results from the optical diameter and for the crystallite size from x-ray diffraction are in the same order of magnitude. The crystal size calculated from the XRD pattern corresponds to the size of so called coherent crystal regions (see chapter 5.3.1), and therefore not to the actual particle size. The optical diameter is calculated from the shift of the onset of absorption. That means starting from an electronic transition in the semiconductor. A particle will not be a simple crystal. It will either be composed of several crystals, or of crystals with different domains, smaller than the actual particle size, or of a crystalline domain embedded in an amorphous domain. The question is now if this influences the confinement effect. Is there only one exciton present in the particle, experiencing the spatial confinement due to the particle size of the whole particle, or experiences the exciton the spatial confinement arising from the size of the separate crystalline domains, and are there so, several

excitons possible in one particle?

It is said in literature, that to observe the quantum size effect the particle size must become smaller than the exciton Bohr radius. The onset of absorption of our particles is clearly blue shifted to 310 nm, so most of the particles must be smaller than 5 nm. But with the particle size measurements carried out it is more likely that the majority of the particles is 5 nm or bigger, so that the majority of the particles do not experience a quantum confinement. If this would be the case, one should observe an absorption spectrum where the absorption starts at 340 nm, the bulk value for ZnS. This is not the case. When the particles experience a confinement due to the crystallites or crystal domains in the particle and not due to the whole particle this would be clearer. This means that the optically active unit of the particles corresponds not to the particle itself but to a smaller unit within the particle. The presence of different domains within a crystal has for example been shown with HRTEM images for nanosized silicon powders [Hof96]. So no conclusions can be made about the widening of the band gap from particle size measurements like PCS, AUC, aF-FFF or TEM. The method that is most likely to determine the size of the optical diameter are calculations from XRD patterns.

# Chapter 8

## Optical properties

For the application as biosensors the optical properties of the synthesized particles are their most important feature. They are therefore investigated but a lot of these properties are still controversial and unclear.

Absorption und emission spectra are for example frequently measured, but not brought into a form where they can be compared with other measurements. To compare luminescence emissions measured with different spectrometers one has to transfer them into quantum yields, which is only rarely done.

Fluorescence quenching effects for nanoparticles in connection with dispersion concentration have to the authors knowledge not yet been reported, and so no work to explain this for nanocrystals has been done yet.

The lifetimes for  $\text{Mn}^{2+}$  emission in a ZnS nanoparticles have been measured with varying results. Bhargava *et al* for example reported a lifetime shortening for the  $\text{Mn}^{2+}$  emission in  $\text{Mn}^{2+}$  doped ZnS quantum dots down to ns [Bha94/2, Bha96], whereas Murase *et al* reported ms lifetimes for the  $\text{Mn}^{2+}$  emission [Mur99]. To the authors knowledge there have been only two groups that investigated the lifetimes of the blue ZnS emission. Bol *et al* reported lifetimes from 50 ns to 250 ns for this emission [Bol98], whereas Murase *et al* determined it to be in the region of 10 ns. This shows that the results of lifetime measurements are still controversial and worth a further investigation.

The effect of the dopant concentration on the luminescence efficiency has been investigated and reported, but the reasons for this quenching are still unclear.

In this chapter we investigated the synthesized particle for their fluorescence quantum yields, examined the changes of the quantum yield with dispersion and dopant concentration, and made lifetime measurements with different set ups.

## 8.1 Luminescence quantum yield

For applications as biosensors the luminescence intensity of the particles is important. Since the intensity is an apparatus depend value one has to talk in terms of quantum yields, when one wants to compare results obtained with different fluorescence spectrometers. A method to do this is described in section 2.1.2. Here the sample is compared with a reference substance of known quantum yield. We used quinine sulphate as reference substance.

### 8.1.1 Quinine sulphate

The reference substance for quantum yield measurements should have its absorption and emission in the same range as the sample. Since our particles have a large stokes shift and most organic dyes have the absorption and emission peak very close to one another, it was rather difficult to find such a substance. Quinine sulphate has two absorption maxima one at about 320 nm and the second at 350 nm. The emission peaks at a wavelength of about 460 nm. The absorption and emission spectra, as well as the structure of quinine sulphate can be seen in figure 8.1.

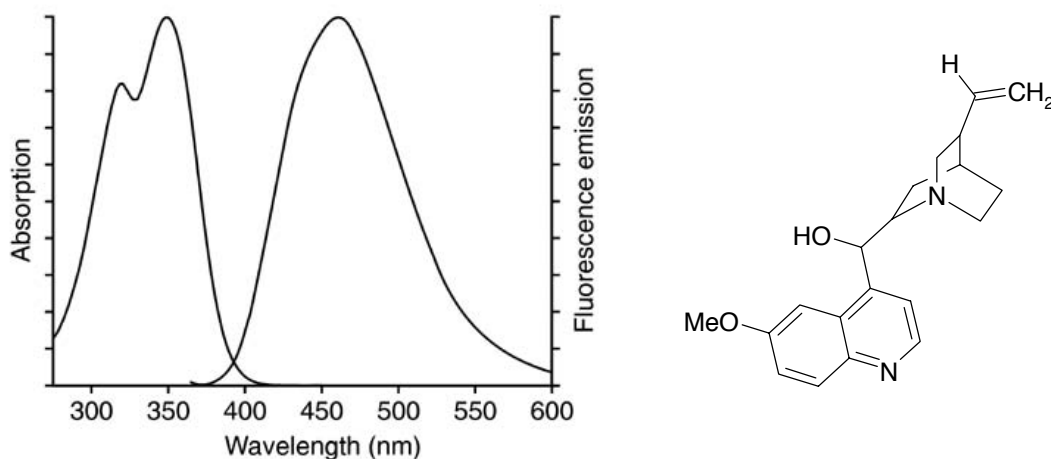


Figure 8.1: Absorption and emission spectra and structure of quinine sulphate

Quinine sulphate has a quantum yield of 50 % when dissolved in 0.5 M  $\text{H}_2\text{SO}_4$ . In section 2.1.2 it was explained that reference and sample should preferably be in the same solvent, otherwise corrections for the refractive indices should be made. We consider the differences for the refractive indices for 0.5 M  $\text{H}_2\text{SO}_4$  and water as small, and so made no correction.



### 8.1.2 Fluorescence quenching

The fluorescence quantum yields have been calculated with equation 2.5.

$$\Phi_S = \frac{A_R \cdot E_S \cdot n_S^2}{A_S \cdot E_R \cdot n_R^2} \cdot \Phi_R$$

It was observed during fluorescence measurements, that the luminescence intensity increases first with dilution before it then diminishes. So the quantum yield was determined for different dilutions of the sample resulting in the graph displayed in figure 8.2. To make the graphs more comprehensible and to show that the values for the quantum yield tend to a limit value, the inverse of the mass content was plotted versus the quantum yield. So that means that high values on the x-axis represent small mass contents.

The points in figure 8.2 represent the measured value, the curve added is a logarithmic fit of these points to guide the eye. The limit value the quantum yield is tending to, represents the quantum yield for infinite dilution, that means the quantum yield of a single particle. In figure 8.2 one can see that with our measurements we are not yet in the region where the quantum yield gets constant, but it was not possible to dilute any further, because with a dilution of a factor of 100 we reach the detection limit of the UV/vis spectrometer.

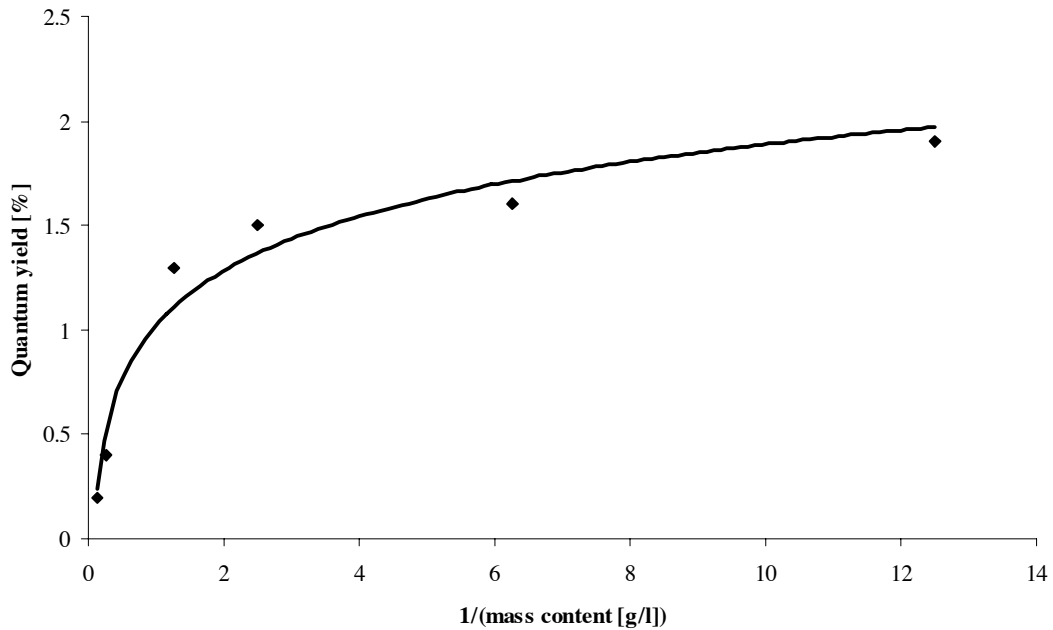


Figure 8.2: Plot of quantum yields of ZnS:Mn nanoparticles for different dilutions, showing concentration quenching

The maximum quantum yield measured with this method was about 2 % for the highest dilution. This is very small compared with the 50 % of quinine sulphate or the 100 % of rhodamine.

The effect when the quantum yield decreases with increasing concentration is called concentration or fluorescence quenching. The two most frequently processes leading to fluorescence quenching are dynamic and static quenching (see section 2.1.3). Dynamic quenching results from collisions between the fluorophore and the quencher. Static quenching is due to complex formation. In both cases quenching requires molecular contact between the fluorophore and the quencher. In case of the collisional quenching, the quencher must diffuse to the fluorophore during the lifetime of the excited state. Upon contact, the fluorophore returns to the ground state without emission of a photon. In the case of static quenching a nonfluorescent complex is formed between the fluorophore and the quencher [Lak83].

To distinguish between dynamic and static quenching, one can carry out measurements at different temperatures. Since the dynamic quenching depends upon diffusion, larger temperatures result in a larger diffusion coefficient and the bimolecular quenching constant is expected to increase. In contrast, increased temperature is likely to result in decreased stability of complexes, and thus lower values of static quenching constants. A plot for  $F/F_0$  versus  $[Q]$  leads to a linear Stern-Volmer plot for dynamic and static quenching. With increasing temperature the slope for dynamic quenching increases, that for static quenching decreases (see figure 8.3).

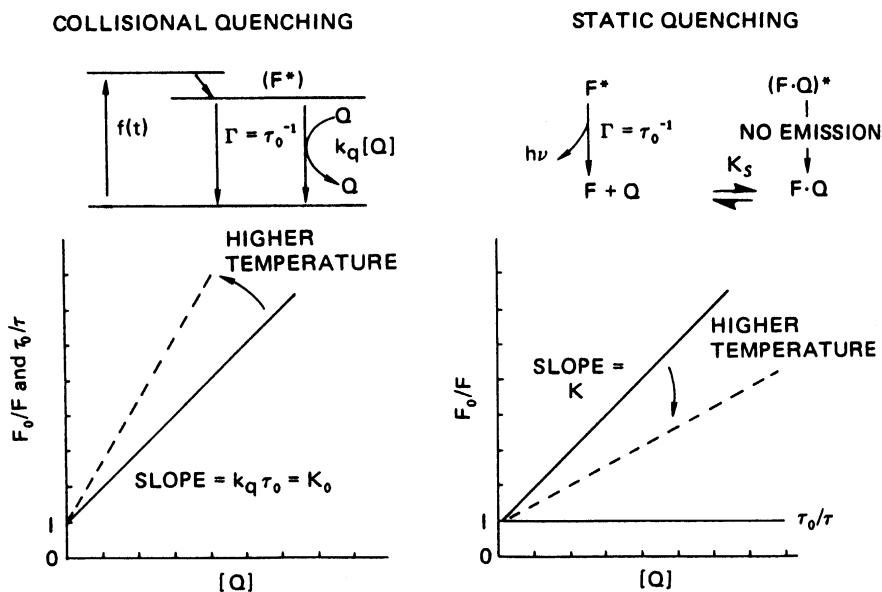


Figure 8.3: Stern-Volmer plot for dynamic and static fluorescence quenching

The quenching effects discussed are always dependent on the quencher concentration. The question is now what acts as quencher in our dispersions. Oxygen can for example act as a quencher. Another possibility would be that the particles quench themselves by colliding with one another. Instead of losing energy by emission of a photon, the electron could relax by losing the energy by colliding with other particles.

## Absorption

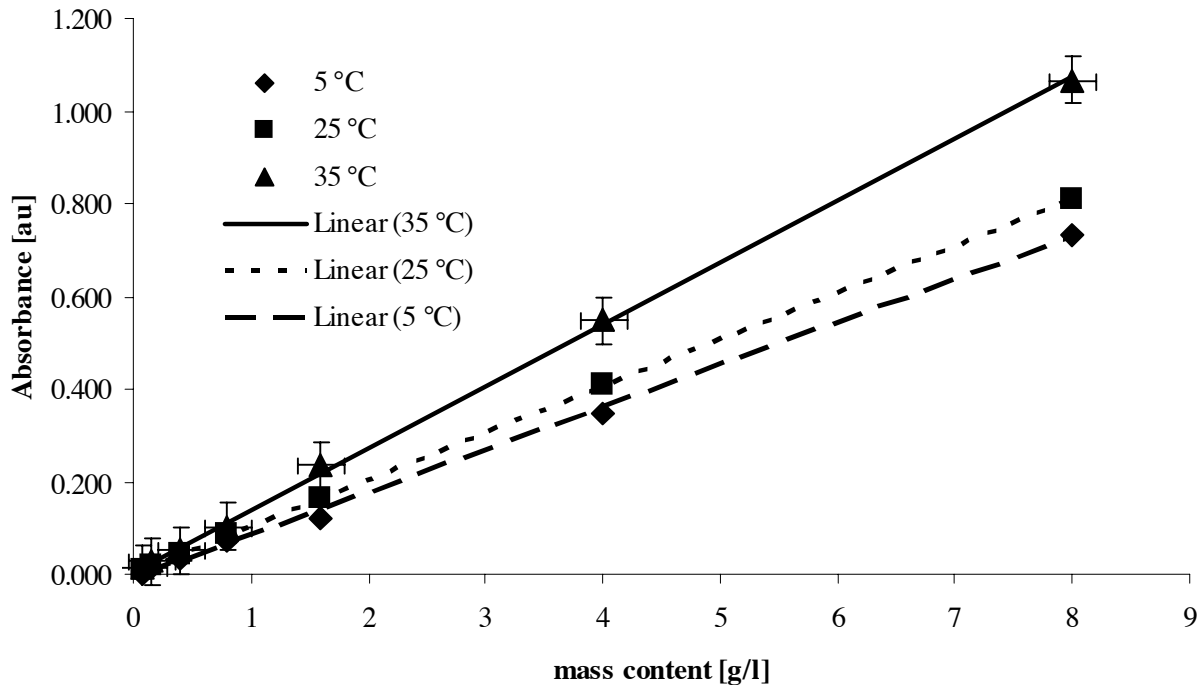


Figure 8.4: Absorption of ZnS:Mn nanoparticle dispersions for different mass contents and different temperatures.

To verify which kind of quenching is present in the case of our nanoparticles, and maybe to get an idea what acts as quencher, a particle dispersion was measured at different temperatures (5 °C, 25 °C, 35 °C). In figure 8.4 one can see the absorption of the dispersion for different dilutions at the three temperatures. In this figure one can see the linear increase in absorption with particle content in the dispersions. The slope of these straight lines corresponds, according to Lambert and Beer's law (equation 8.1), to the product of the path length  $l$  and the molar absorptivity or extinction coefficient of the sample [Hol95].

$$A = \lg\left(\frac{I_0}{I}\right) = \varepsilon_A \cdot l \cdot c \quad (8.1)$$

Since the path length is constant during the measurements the changes in the slope should only be due to changes in the extinction coefficient which is for solutions independent of the concentration, but is a function of wavelength, temperature and solvent [Bur81]. In figure 8.5 the extinction coefficients calculated from the slopes are plotted against the temperature. The increase could be described as linear, but it is difficult to make a statement on this with only three points.

Another point that adds to the change of the absorbance with temperature besides the temperature dependency of the extinction coefficient is the cysteine concentration in the dispersion. Since the cysteine is not covalently attached to the particle surface there is equilibrium between attached and free cysteine. This equilibrium is surely temperature dependant and so the concentration of free cysteine in the dispersion will change with temperature.

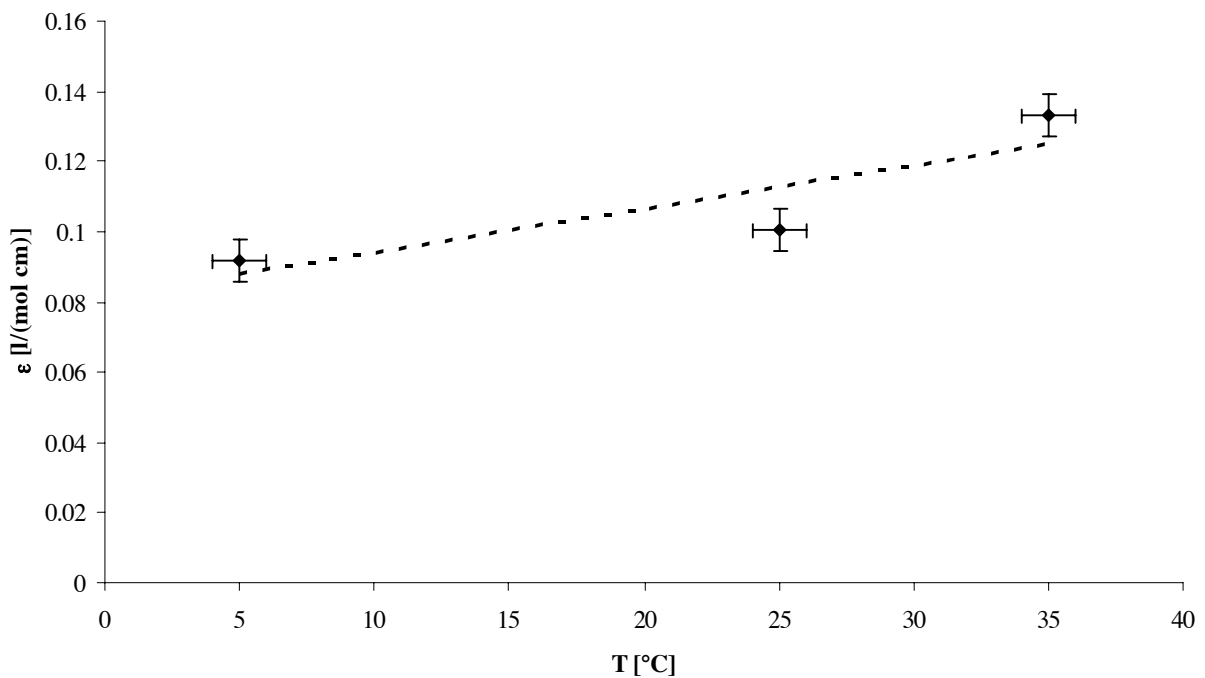


Figure 8.5: Extinction coefficients for ZnS:Mn nanoparticle dispersions at 5, 25 and 35 °C.

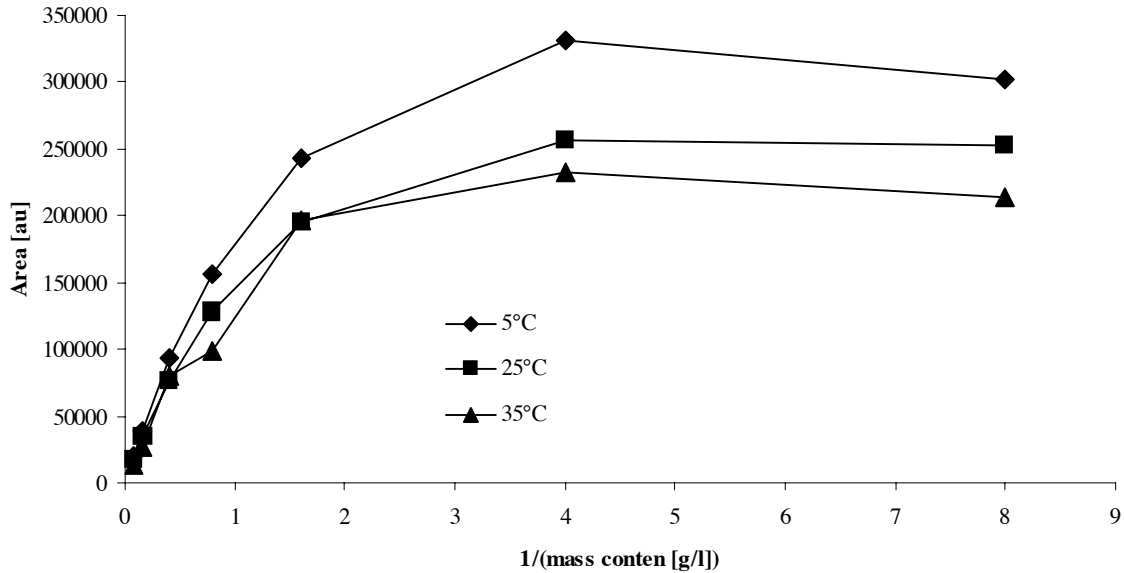
**Emission**

Figure 8.6: Emission of ZnS:Mn nanoparticle dispersions for different mass contents and different temperatures.

In figure 8.6 the area under the luminescence emission peak is plotted against the inverse of the mass content of the dispersions. The measuring points are connected to guide the eye and make the graph more comprehensible. One can observe a first increase of the emission with increasing dilution. For the last values one can then observe a decrease, which indicates that we are at dilutions where the concentration quenching is getting less effective. The emission, decreases with increasing temperature.

**Quantum yield**

Finally in figure 8.7 the quantum yields for different temperatures are plotted versus the inverse of the mass content. We obtain the same characteristics for the respective temperatures as for the measurements shown in figure 8.2, but here we can also see that the quantum yield increases with decreasing temperature.

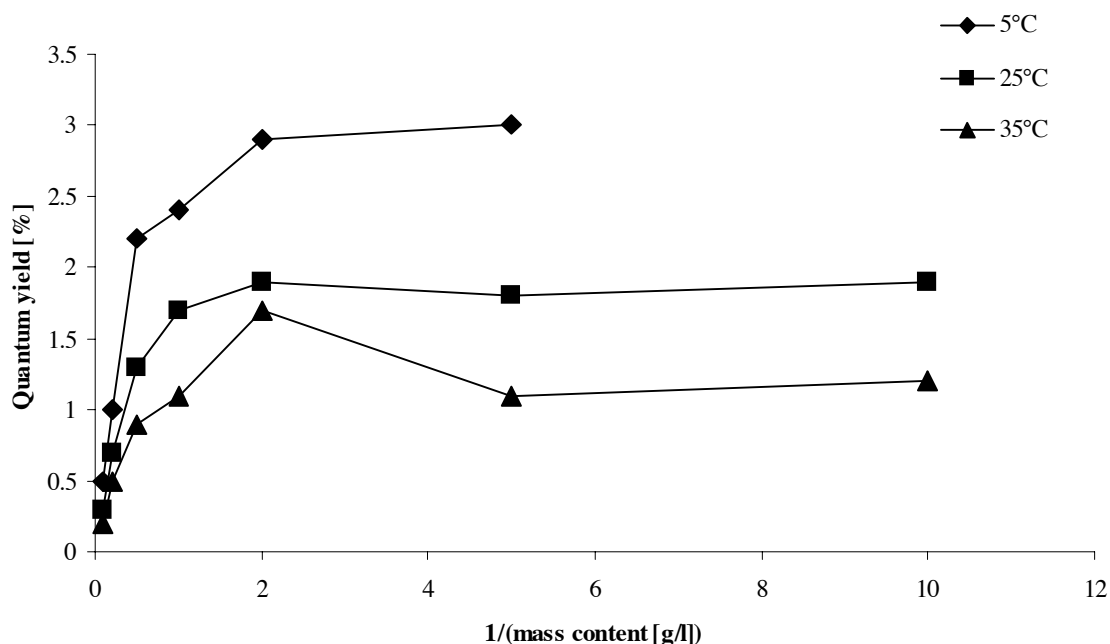


Figure 8.7: Quantum yield versus  $1/(\text{mass content})$  plot for different temperatures.

### Stern-Volmer plot

Like already mentioned above the quencher is present in the dispersions after sample preparation. The most likely cases are either that the particles quench themselves by colliding with one another, or that oxygen present in the sample, which is known to be a good quencher, does it. When we dilute the samples with water, the quantum yield increases. When the oxygen dissolved in the water is responsible for the quenching we would, by diluting, decrease the fluorophore concentration, but not the quencher concentration, since we add dissolved oxygen by adding water. So the fluorophore to quencher ratio would decrease, and so the quantum yield should also decrease.

When the particles quench themselves by collisions like mentioned above, by diluting, we change the concentration of the quencher and the fluorophore at the same time. So there is less fluorophore present in the sample but there are also fewer collisions so that it is possible that by diluting the emission first increases despite the fact that the fluorophore concentration decreases, because the decrease of quenching compensates this. But there will be a point when this is never possible and the emission will decrease due to dilution. This can be seen in figure 8.6 where the last data point shows a beginning decrease in luminescence emission. Since we have the quencher always present in the sample it is not possible to determine  $F_0$ , the luminescence intensity without quencher.

Furthermore, it is not possible to vary the quencher concentration independently from the fluorophore concentration.

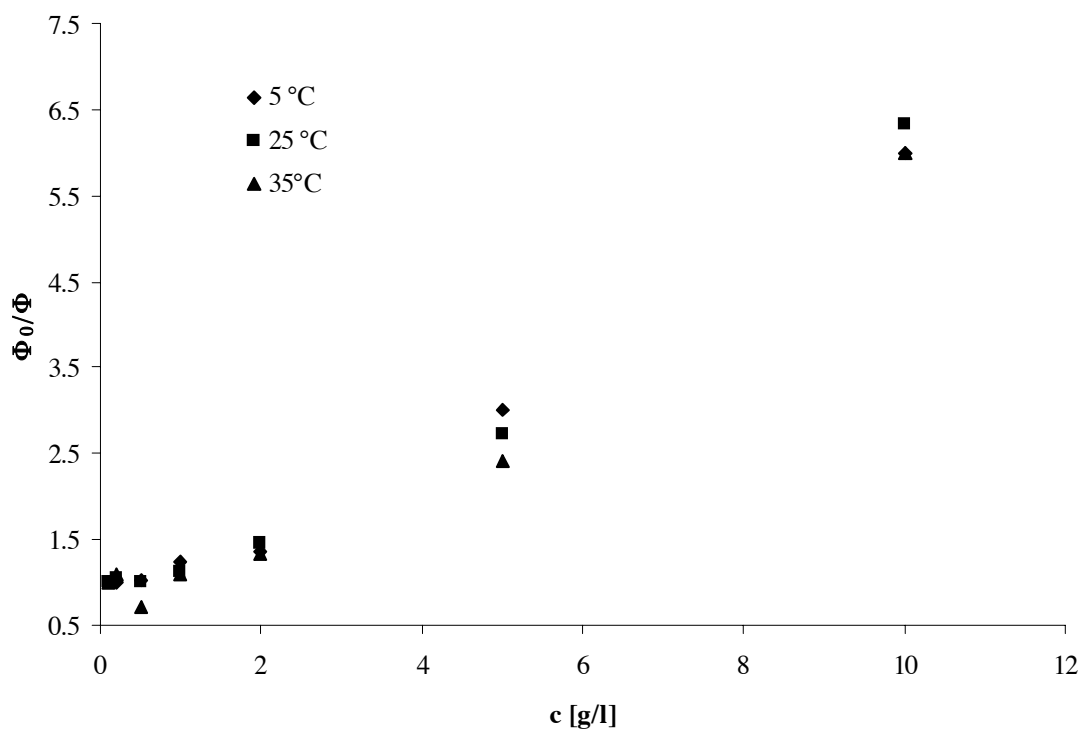


Figure 8.8: Stern-Volmer plot for ZnS:Mn nanoparticle dispersion.

When we assume that the luminescence for the highest dilution represents  $F_0$ , and we plot the quantum yield for the highest dilution versus the mass content, we obtained graph 8.8. In principle we obtain three linear plots starting at a value of one for  $\Phi_0/\Phi$  like for a Stern-Volmer plot, but the differences between the values are so small, that it is not possible to judge if we have a collisional quenching behaviour for these plots. Only the values for the a mass content of 5 g/l are clearly distinguishable from one another and show an increase of  $\Phi_0/\Phi$  for decreasing temperatures which would be characteristic for a collisional quenching. When the plots for the different temperatures coincide, this would mean that the quenching is not temperature dependant. So that our quenching mechanism can be described neither by collisional nor static quenching. Since with the temperature measurements no statement about the quenching mechanism is possible, other methods have to be applied.

Another possibility to distinguish between static and dynamic quenching is via the lifetimes of the excited state. The theoretical aspects for this are presented in section 2.1.3 and the lifetime measurements are described in section 8.2.2.

Another approached is to calculate the mean free path of the particles and then

determine the time they need to make this distance via the diffusion coefficient. This was made in the following chapter.

### 8.1.3 Mean free path

The number of collisions between particles in a certain time depends on the number of particles present in the sample and their velocity. The distance a particle can cover between two collisions is called the mean free path. We consider the position of all particles except one to be frozen [Atk98]. So when a particle travels through a dispersion with a relative velocity  $\bar{c}_{rel}$  for a time  $\Delta t$ , it sweeps out a tube of cross-sectional area

$$\sigma = \pi \cdot d^2 \quad (8.2)$$

and the length  $\Delta t \cdot \bar{c}_{rel}$ , and therefore the volume

$$V = \sigma \cdot \Delta t \cdot \bar{c}_{rel} \quad (8.3)$$

One counts a hit, whenever a stationary particle comes with its centre in this tube, so the number of collisions  $z$  per time interval  $\Delta t$  is

$$z = \sigma \cdot \bar{c}_{rel} \cdot N \quad (8.4)$$

with  $N$  being the number of particles per volume. If all particles move this changes to [Atk98]

$$Z = \sqrt{2} \cdot \sigma \cdot \bar{c}_{rel} \cdot N \quad (8.5)$$

With the collision frequency one can calculate the mean free path  $\bar{l}$ . If a particle collides with a frequency  $Z$ , it spends a time  $1/Z$  in free flight between collisions, and therefore travels the distance  $(1/Z)\bar{c}_{rel}$ . Therefore, the mean free path is

$$\bar{l} = \frac{\bar{c}_{rel}}{Z} \quad (8.6)$$

Substitution with equation 8.5 gives

$$\bar{l} = \frac{1}{\sqrt{2} \cdot \sigma \cdot N} = \frac{1}{\sqrt{2} \cdot \pi \cdot d^2 \cdot N} \quad (8.7)$$

The particle density  $N$  is given in particles per  $\text{m}^3$ , so with the concentration of 0.035 mmol/l for the dispersions calculated in annex F, we obtain a particle density of  $N = 2.57 \cdot 10^{22} \frac{1}{\text{m}^3}$ . The collision cross section for 5 nm particles is  $\sigma = 7.85 \cdot 10^{-17} \text{ m}^2$ .

This leads to the mean free path of



$$\bar{l} = 3.5 \cdot 10^{-7} m = 350 nm$$

Thus the mean free path corresponds to 70 times the particle diameter. The highest dilution applied for the quenching was a factor of 100, with this dilution one obtains a mean free path of 35  $\mu m$ .

The diffusion coefficient can be calculated with the Stokes-Einstein equation.

$$D = \frac{k_B \cdot T}{6 \cdot \pi \cdot \eta \cdot r} \quad (8.8)$$

For a temperature  $T = 298$  K, and the viscosity of water being  $\eta = 1$  mPa  $\cdot$  s one obtains a diffusion coefficient of

$$D = 8.73 \cdot 10^{-11} \frac{m^2}{s}$$

Thou in 1 s a particle can travel the mean distance  $\bar{x}$  of

$$\bar{x} = \sqrt{D \cdot t} = 9.3 \cdot 10^{-6} m, \quad (8.9)$$

which corresponds to the mean velocity for the particle of

$$\bar{v} = 9.3 \cdot 10^{-6} \frac{m}{s}$$

With this velocity it takes the particles 0.04 s to travel the distance of 350 nm corresponding to the mean free path calculated above. So for a collisional quenching to be effective we should at least have a luminescence lifetime of 40 ms.

Lifetime measurements for the particles are presented in chapter 8.2, the results will be discussed there.

#### 8.1.4 Influence of the SiO<sub>2</sub> shell

The quantum yields observed for manganese doped ZnS nanoparticles are considerably smaller compared with organic fluorophores with quantum yields up to 100 %. The reasons possible for this could be either radiationless recombination of the electron and the hole or the recombination over the band gap, yielding in the typical blue ZnS emission.

Radiationless emission will mainly occur at the particle surface, were defect states in form of unsaturated bonds act as electron traps. So a saturation of these bonds by coating the particles should prevent this and increase the particle quantum yield.

We chose a SiO<sub>2</sub> coating, since its refractive index matches well with the refractive index of the ZnS, so that the light is diffracted into the particle core ( $n_{ZnS} >$

$n_{SiO_2}$ ). The shell has to be a higher band gap material or an insulator otherwise the shell and not the core would be excited. This is also given with  $SiO_2$  being an insulator.

Although the increase of luminescence by coating particles with an inorganic capping is often reported for CdS [Hen87, Spa87] and CdSe [Kor90, Hoe92, Dab97, Pen97, Hin96], this is not the case for ZnS:Mn particles. Reports on coating ZnS with  $SiO_2$  or incorporating them into  $SiO_2$  thin films can be found [Vel01, Bha02, Bha02/2], they are not concerned with changes of the optical properties.

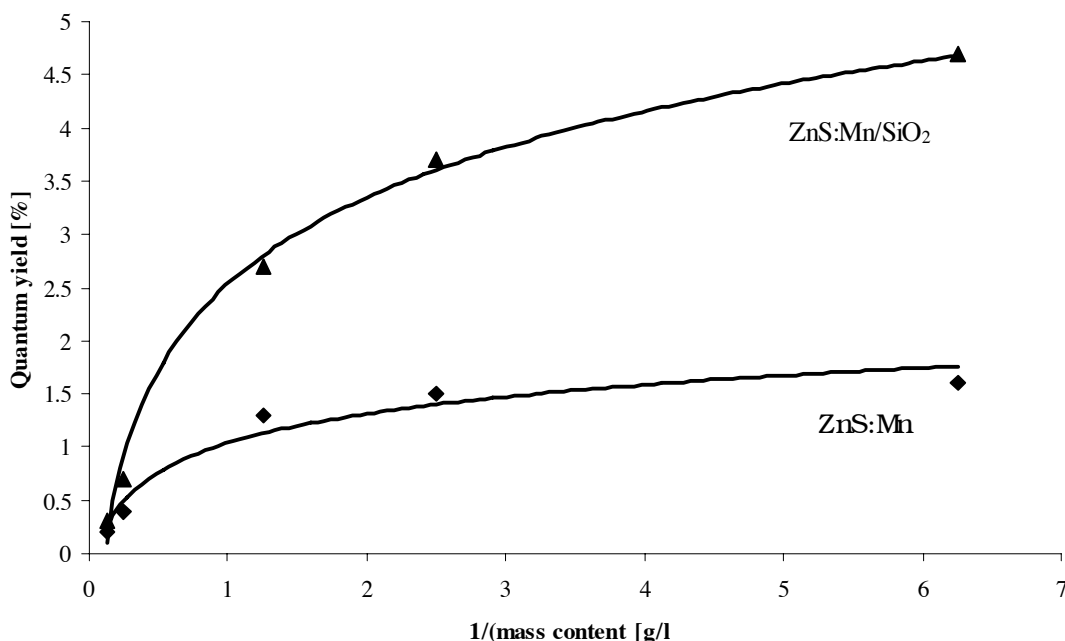


Figure 8.9: Quantum yields of coated and not coated ZnS:Mn nanoparticles.

The only group that observed an increase of the luminescence for  $SiO_2$  coated Zn:Mn nanoparticles are to the authors knowledge Ethiraj *et al* [Eth03]. The coating on thioglycerol stabilized particles was performed with TEOS and particles with a diameter of about 600 nm were obtained. Unfortunately the increase in luminescent intensity or quantum yield was not further quantified.

In figure 8.9 one can see their results affirmed. In this graph the quantum yield curves for a dispersion before and after coating are plotted. The graph for coated particles shows higher quantum yields than for the uncoated particles. One observes an increase of the quantum yield for maximum dilution of a factor of three. So the coating in fact influences the quantum yield as reported [Eth03].

A TEM micrograph and the AUC results for this experiment have already been presented in the figures 6.15 and 6.14 in section 6.6. There one can see that not all particles are coated, and that the resulting particles have sizes from 20 to 80 nm. If a complete coating of the particles could be achieved a further increase of

the fluorescence quantum yield would be possible.

### 8.1.5 Influence of the doping

The orange fluorescence obtained from the particles is due to an electron transition within the d-orbitals of the  $\text{Mn}^{2+}$  doping. So the quantum yield should be dependent on the doping concentration. To investigate this, samples with a molar percentage of 0.05-0.55 at% of manganese were prepared and characterized for their optical properties.

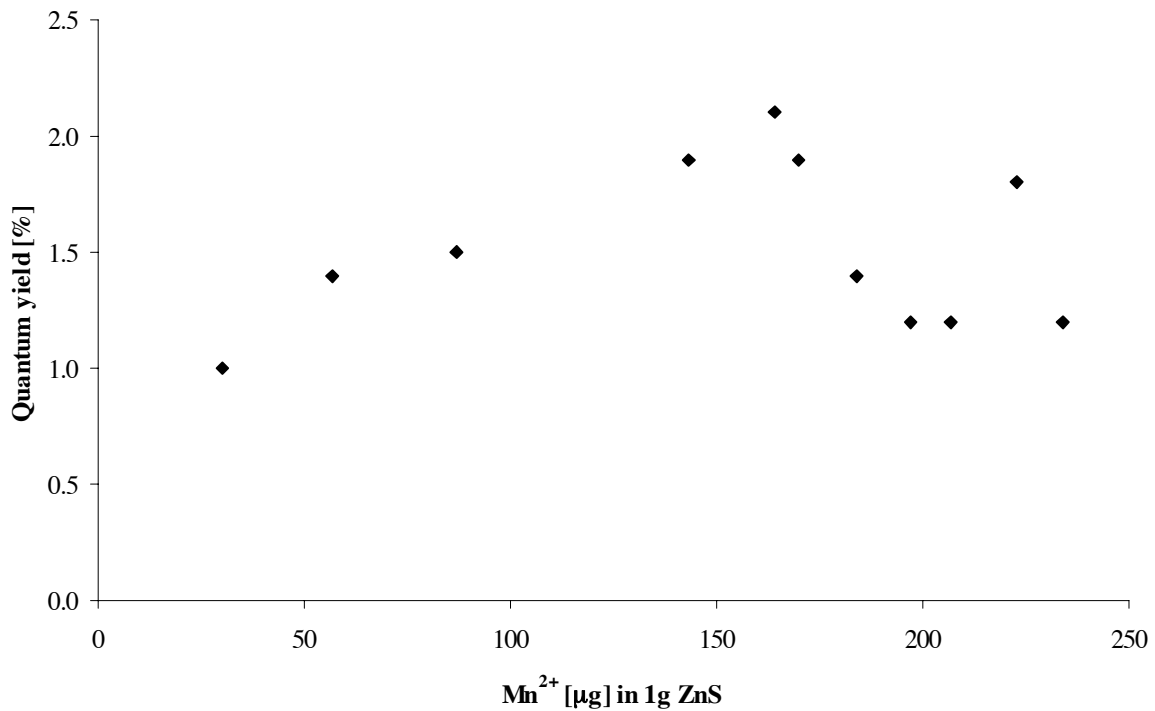


Figure 8.10: Quantum yield for different  $\text{Mn}^{2+}$  contents in 1 g ZnS without cysteine.

In figure 8.10 one can observe that the quantum yield increases first with increasing  $\text{Mn}^{2+}$  content, then it reaches a maximum to then finally decrease with increasing  $\text{Mn}^{2+}$  content. The quantum yields displayed were measured for a dilution of a factor of 100, to have the less fluorescence quenching effect possible. The maximum quantum yield is obtained for a  $\text{Mn}^{2+}$  content of 164  $\mu\text{g}$  per gram ZnS. This corresponds to a doping of 0.03 at%  $\text{Mn}^{2+}$ . The plotted values can also be seen in table 8.1. The value for 223  $\mu\text{g}$   $\text{Mn}^{2+}$  in 1 g ZnS shows a quantum yield of 1.8 % which is too high compared with the quantum yields measured for samples with a similar  $\text{Mn}^{2+}$  content. If we attribute this to a error in one of the

measurements it could be either that the quantum yield was measured too high or the  $\text{Mn}^{2+}$  content.

In table 8.1 one can see that that the quantum yield fits well in the series of measured points since it corresponds to 0.25 at%  $\text{Mn}^{2+}$  in the reaction mixture, but that the  $\text{Mn}^{2+}$  content does not fit at all in the series. So we attribute this point to an error in the ICP measurement. In figure 8.11 one can see the plot of the  $\text{Mn}^{2+}$  to  $\text{Zn}^{2+}$  ratio in the reaction mixture and in the ZnS powders. This graph can give information about the incorporation of  $\text{Mn}^{2+}$  in the particle and about the quality of the ICP measurements.

The measurements show a good linearity for the first three and the last four points. The four points in the middle fit not that well, especially the one 0.25 at% in the reaction mixture. This is the same point that also does not fit in graph 8.10. Errors for the ICP measurements can for example be introduced when the plasma is not stable. Several times the plasma stopped during a series of measurements and had to be restarted this could introduce fluctuations like for the four points in the middle of the measured series.

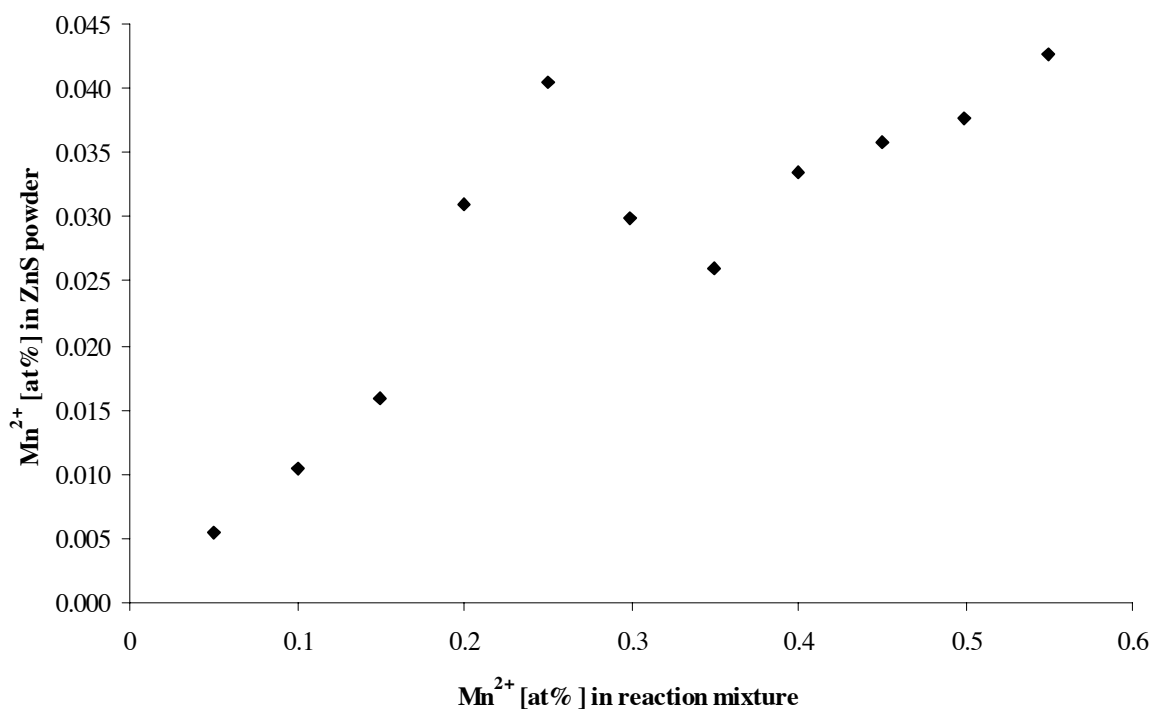


Figure 8.11:  $\text{Mn}^{2+}$  to  $\text{Zn}^{2+}$  ratio in [at%] in reaction mixture and 1 g ZnS determined with AES-ICP.

A decrease in quantum yield for an increase of dopant has been observed by other groups. They report the maximum luminescence intensity (not quantum yield) to occur at 2 at% [Soh96, Soo96] and 10 at% [Bol98] respectively. Only Bol *et al* explain that their value refers to  $\text{Mn}^{2+}$  in the reaction mixture, for the other two publications this was not specified.

Since we either do not know to what their values refer or how much is actually incorporated in the particles in the case of Bol *et al* it is difficult to compare our values with theirs. As it can be seen in table 8.1 there is a factor of about 10 between the  $\text{Mn}^{2+}/\text{Zn}^{2+}$  in the reaction mixture and in the particles. A similar behaviour has been reported by Gallagher *et al* [Gal95]. For an organometallic synthesis they found 0.87 at%  $\text{Mn}^{2+}$  in the powders for 10 at% in the reaction mixture. So only a small percentage of the  $\text{Mn}^{2+}$  is actually incorporated in the particles.

Table 8.1: Manganese contents in reaction mixture, ZnS powder and per particle. [at%] is related to Zn

$\text{Mn}^{2+}$ [at%] in reaction mixture	$\text{Mn}^{2+}$ [at%] in 1g ZnS	$\text{Mn}^{2+}$ [ $\mu\text{g}$ ] in 1g ZnS	QY [%]	$N_{Mn}$
0.05	0.005	30	1.0	0.1
0.1	0.01	57	1.4	0.2
0.15	0.016	87	1.5	0.3
0.2	0.031	170	1.9	0.5
0.25	0.041	223	1.8	0.7
0.3	0.03	164	2.1	0.5
0.35	0.026	143	1.9	0.4
0.4	0.034	184	1.4	0.5
0.45	0.036	197	1.2	0.6
0.5	0.038	207	1.2	0.6
0.55	0.043	234	1.2	0.7

There are different reasons given in literature for the decrease of the quantum yield. Enrichment of  $\text{Mn}^{2+}$  at the particle surface of the ZnS particles, or the formation of separate MnS particles [Soh96], or a so called concentration quenching [Bol98]. Concentration quenching involves resonant transfer of electronic excitation energy from the initially absorbing ion to another identical ion and, after a number of energy transfer steps, to a quenching site (for example a defect) [Bol01/2]. A problem with this theory is the fact, that we do not directly excite the manganese impurity, but the ZnS host. For the energy transfer the emitted radiation would necessarily directly excite the manganese. We tried to do this with the spectrometer, and it was not possible. But this does not proof

that this quenching mechanism is not possible. Another problem is the fact that the concentration of the dopant metal must exceed a limiting value, so that the distance between the  $\text{Mn}^{2+}$  gets small enough for this transfer to take place. So it is interesting to know how many manganese atoms are present in a particle for a certain doping percentage.

Yu *et al* calculated that there are 4 Mn atoms in particle with a diameter of 2.5 nm and a doping of 1 at%. The number of atoms in a cubic ZnS particle  $N_P$  can be calculated with the following equation [Lip89]:

$$N_P = \frac{4}{3}\pi\frac{d^3}{a^3} \quad (8.10)$$

With a lattice constant of  $a=5.82 \text{ \AA}$  [Ave67] and a diameter of 5 nm one obtains with equation 8.10, 2660 atoms per particle. Since ZnS is a one to one compound this corresponds to 1330 Zn atoms per particle. The number of Mn atoms per particle  $N_{Mn}$  for the doping percentages obtained with ICP measurements can be seen in table 8.1. For our small percentages we do not even have one Mn in every particle, so the concentration quenching process is not applicable for our powders. This is also affirmed by magnetization measurements made in the group of Palacio at the University of Saragossa. They showed the  $\text{Mn}^{2+}$  to be homogenously distributed in the particle so that no magnetic interactions between them could be measured (see annex G).

With these information it is difficult to say which effect is responsible for the decrease in fluorescence quantum yields with increasing  $\text{Mn}^{2+}$  content. It is unlikely that it is due to concentration quenching since there is not even a  $\text{Mn}^{2+}$  ion in every particle. The magnetization measurements do not show the presence of  $\text{Mn}^{2+}$  pairs or triplets which confirms this. It is still possible that with increasing  $\text{Mn}^{2+}$  content in the reaction mixture the tendency to form separate, non-luminescent MnS particle increases. That the  $\text{Mn}^{2+}$  is perhaps adsorbed at the surface instead to be incorporated in the particles is also a possibility. This would indicate that the actual incorporation in the particles is difficult, which is also shown by the factor of about 10 between the initially introduced  $\text{Mn}^{2+}$  content, and the content actually found in the particles.

## 8.2 Luminescence lifetimes

A typical problem in biosensor fluorescence measurements, is to separate the fluorescence signal from the background signal. Typical fluorophores such as fluorescein have fluorescence lifetimes in the nanosecond region (see figure 8.12), backgrounds often have lifetimes in the microsecond region. This reduces the signal to noise ration and leads to difficulties to detect the fluorescence of the dye. So a good fluorophore is either one with a very intense emission compared to the background or with a long lifetime.

Luminescence lifetimes can also give information about the recombination mechanism. So one can distinguish between a fluorescence and a phosphorescence mechanism by means of the lifetimes. Fluorescence mechanisms have lifetimes in the nanosecond region, whereas phosphorescence is in the millisecond region. If a decay is mono- or multi exponential can give an information if there is more than one electron population present in the particles.

For the measurements two different setups have been applied. A simple setup with only a flash lamp as excitation source at the CSEM in Neuchatel, and a more complex laser setup at the University of Mulhouse, which gave as the possibility to measure lifetimes in the nanosecond region.

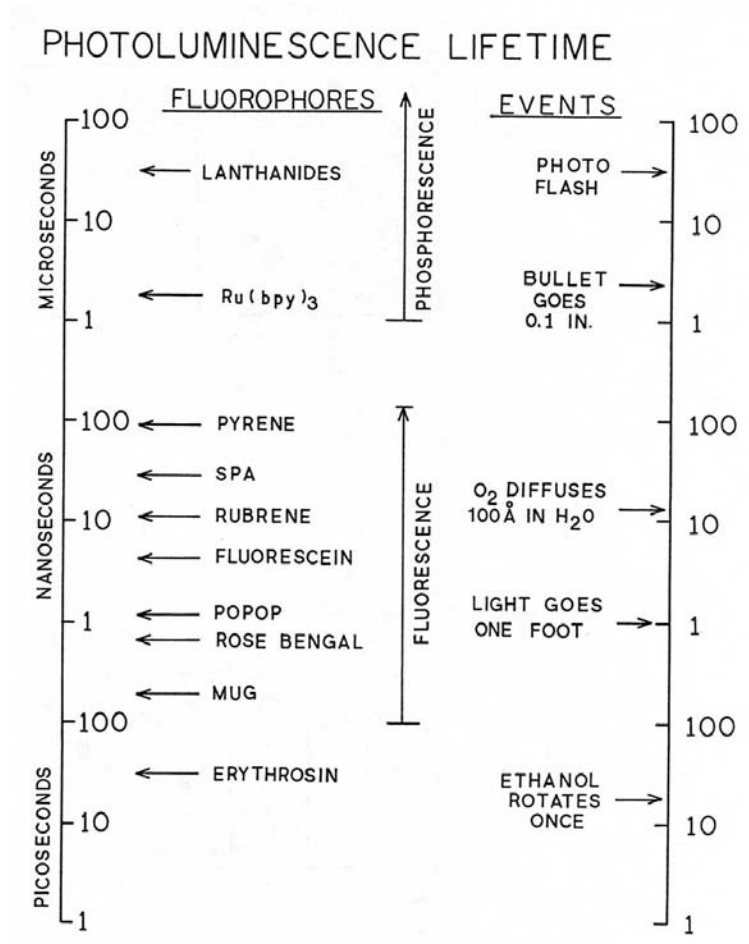


Figure 8.12: List of lifetimes for different fluorophores [Lak99].

With the setup in Mulhouse it was not only possible to measure the long-lived orange emission due to the doping, but also the blue emission due to the ZnS host.

### 8.2.1 Flash lamp measurements

The lifetimes of the ZnS:Mn nanoparticles have been measured at the CSEM in Neuchatel within the framework of the PhD thesis of Caterina Minelli. The excitation wavelength of 310 nm for the particles would require a UV laser for the lifetime measurements. Since these lasers are expensive and require a high security standard, the measurements have been made with a triggered flash lamp. The set up used in Neuchatel is shown in figure 8.13.

For the measurements the samples were either used in form of a dispersion or a drop was dried on a glass slide. Before each measurement the detector was replaced by a camera to allow the correct spot alignment. The flash lamp was triggered at 30 Hz for the sample excitation, the detector recorded the signal with a frequency of 500 kHz.

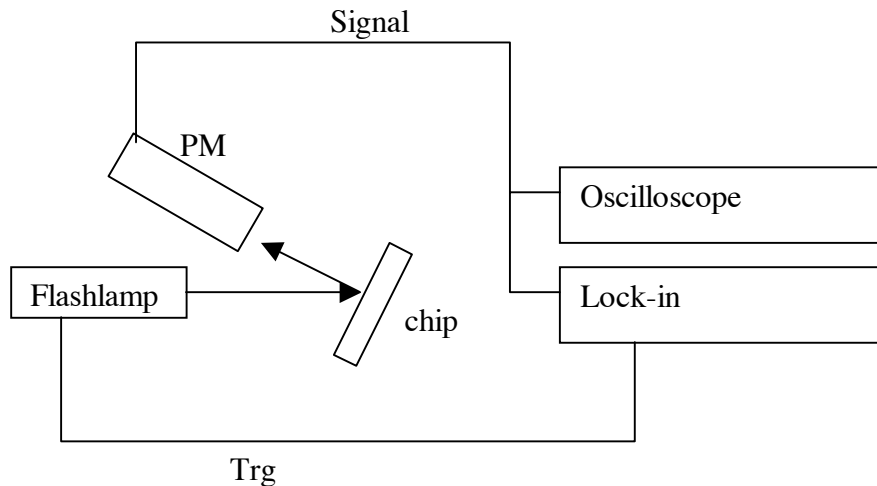


Figure 8.13: Set up for lifetime measurements used at the CSEM.

To record the background signal either the glass slide without the particles or a quartz cuvette with water were measured. The results for background and particle measurements for dispersion measurements can be seen in figure 8.14. The points represent the measured signal, the black curve represents the first order fit made for the measurements. It can be seen that the background signal which comes from the flash lamp and the auto fluorescence of the quartz cuvette, decays more quickly than the particle signal. The background has an average lifetime of  $80 \mu\text{s}$ , the particles about  $260 \mu\text{s}$ . To be sure that the results obtained with this setup were correct, a substance with a known lifetime was measured.



For this FluoroSpheres<sup>®</sup> were used. These are 40 nm carboxylate modified microspheres with  $\text{Eu}^{3+}$  incorporated in an organic coordination complex. They were excited at 365 nm and emit with an emission wavelength of 610 nm, so they could be measured without changing the setup. With 370  $\mu\text{s}$  we obtain a result that indicates a phosphorescence rather than a fluorescence recombination mechanism according to figure 8.12.

The result we obtain with these measurements is that the particles have a lifetime

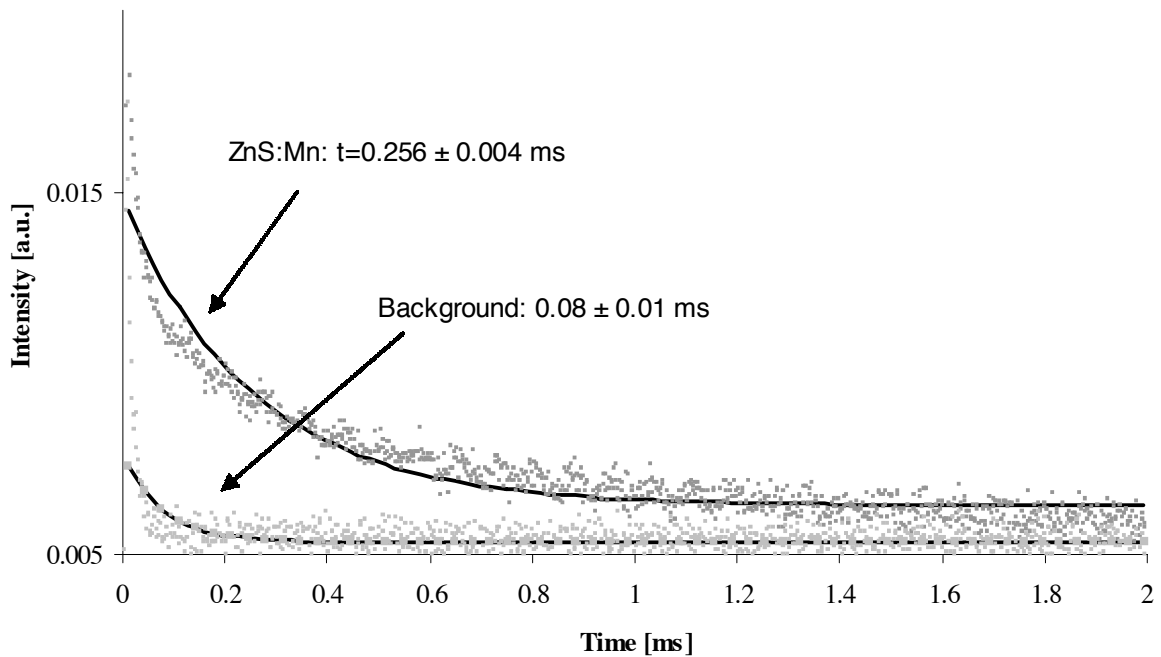


Figure 8.14: Lifetime measurements for ZnS:Mn nanoparticles and the background.

A second result is, that the measurements made for the ZnS:Mn nanoparticles fit better a second order decay than a first order decay. This can be seen in figure 8.14. The mono exponential fit represented in the graph shows a good match to the measurement for long times, at the beginning of the measurements it does not fit as well.

In figure 8.15 one can see the result for a second order fit. That a second order decay matches the measurements better indicates that there is more than one recombination mechanism present in the sample, or that more than not one population of excited electrons exists. Since the luminescence lifetime decays are bound to the energy level structure of the nanoparticles it is not possible to make a statement on this without more precise measurements, and a detailed knowledge of the electronic structure of the particles. But with the fit for a bi

exponential decay two lifetimes are obtained. A faster decay with a lifetime in the region of  $200 \mu\text{s}$ , and a decay with a lifetime of about  $1 \text{ ms}$ .

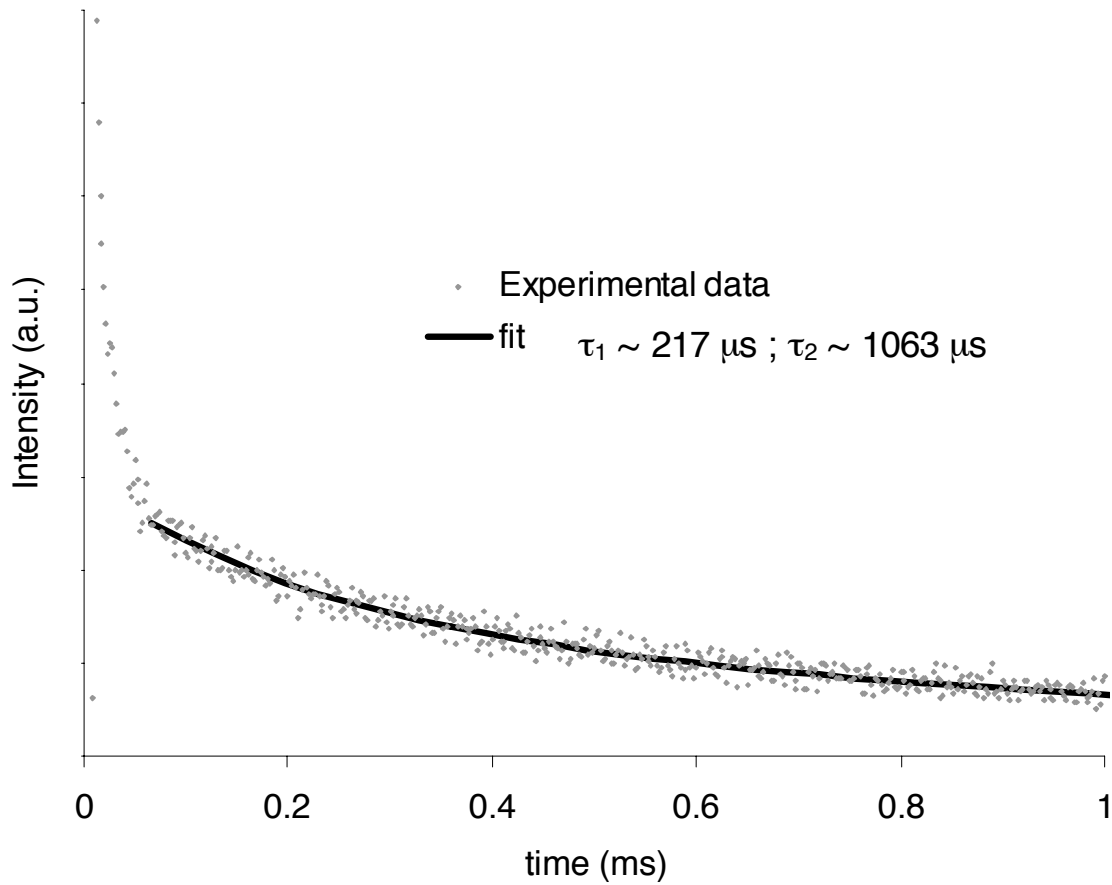


Figure 8.15: Second order fit for the measurements made at the CSEM at Neuchâtel.

### 8.2.2 Nanosecond measurements

To get a better insight in the decay characteristics and to get more precise results, nanosecond measurement with a laser setup have been made at the University of Mulhouse in the group of Professor Allonas. The setup can be seen in figure 8.16. To obtain a 310 nm laser beam the light from a Nd:YAG laser was split into 1064 nm, 532 nm and 355 nm. The 355 nm emission was then split into 620 nm and 829 nm waves and finally a 310 nm laser emission could be obtained with a double frequency device. This beam has to be stabilized and the measurements were then done in a quartz cuvette. As reference the cuvette only filled with water were measured.

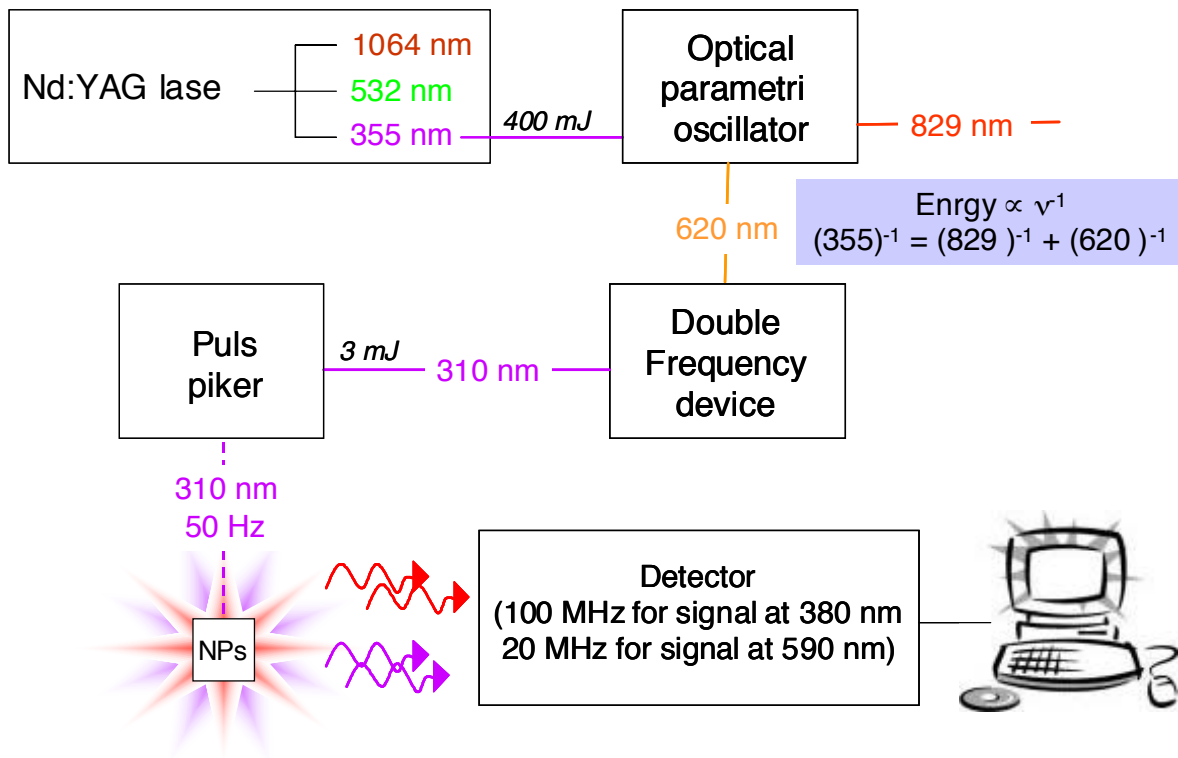


Figure 8.16: Setup for the nanosecond measurements carried out at Mulhouse.

The measurements were made with ZnS:Mn particles and the particles coated with SiO<sub>2</sub>. With these laser measurements it was possible to measure the blue emission due to the ZnS and Mn<sup>2+</sup> emission separately. The maximum of the ZnS emission was measured to be at 380 nm, the one due to the Mn<sup>2+</sup> at 590 nm.

The detection limit of the setup used in Mulhouse is set by the excitation laser pulse. The decay due to this pulse has a full width at half maximum of about 4 ns. That means that only signals with a FWHM of the same order or bigger can

be resolved. The blue emission from the ZnS host is in the order of the excitation laser pulse, so it is necessary to separate this signal from the laser pulse profile. This treatment of the signal is not necessary for the  $\text{Mn}^{2+}$  emission since the luminescence lifetimes are orders of magnitude longer.

The laser excitation pulse of 310 nm and the peak due to the blue ZnS emission can be seen in figure 8.17. As for the results obtained in Neuchatel, also here the decay is better approximated by a bi exponential decay than a mono exponential one. The respective lifetimes obtained for the ZnS emission were 0.77 ns and 11.8 ns.

The result for the  $\text{Mn}^{2+}$  emission is displayed in figure 8.18. As for the ZnS also here the signal can be separated into two signals. The respective lifetimes being 214  $\mu\text{s}$  and 1 ms. The intensity observed for the  $\text{Mn}^{2+}$  emission was considerably lower than the one for the ZnS emission but that does not allow conclusions about the quantum yield, since the quantum yield is not proportional to the luminescence intensity, but to the integral over the emission peak.

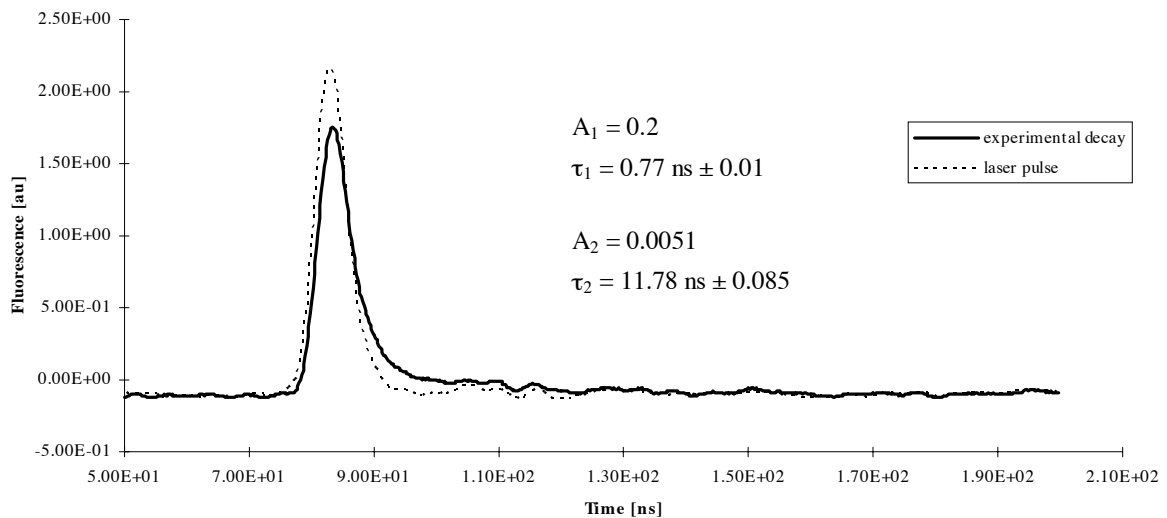


Figure 8.17: Lifetime measurement for the blue ZnS emission, 380 nm.

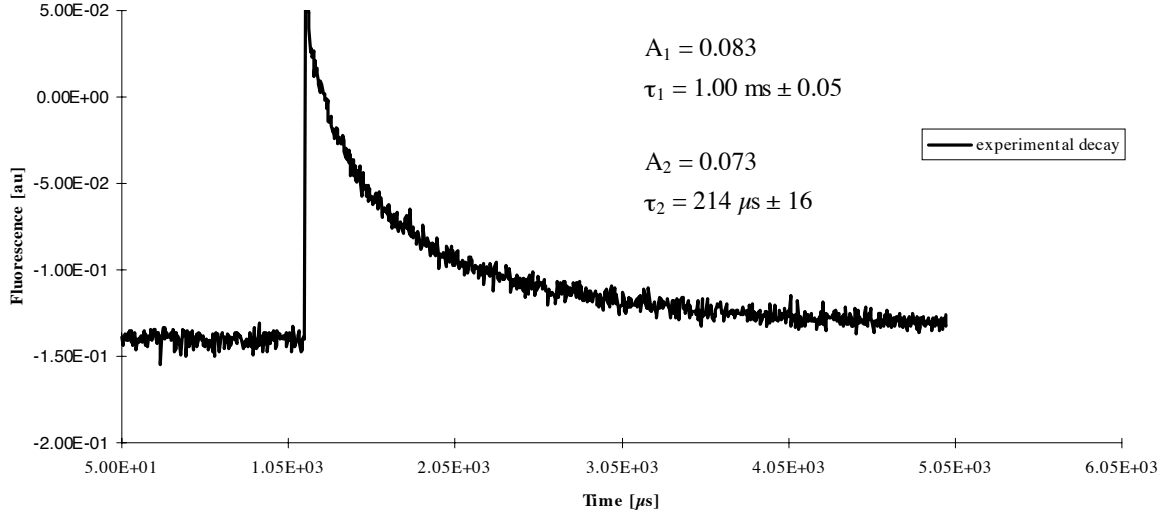


Figure 8.18: Lifetime measurement for the orange  $\text{Mn}^{2+}$  emission, 590 nm.

The same measurements have been carried out for the  $\text{SiO}_2$  coated samples and for the samples diluted by a factor of ten. The results for the fitted function

$$f(x) = y_0 + A_1 \cdot \exp\left(\frac{t}{\tau_1}\right) + A_2 \cdot \exp\left(\frac{t}{\tau_2}\right) \quad (8.11)$$

can be seen in table 8.2 and 8.3. The errors reported are the standard deviations given by the fit. The data analysis error comes from the range in which the fit is done. Varying the extremities of this range can result in changes of the results bigger than the standard deviation.

Table 8.2: Lifetimes for the blue emission due to ZnS at 380 nm.

	$A_1$ [au]	$\tau_1$ [ns]	$A_2$ [au]	$\tau_2$ [ns]
<b>ZnS:Mn</b>	0.2	$0.77 \pm 0.01$	0.0051	$11.78 \pm 0.008$
<b>ZnS:Mn x10</b>	0.13	$1.085 \pm 0.005$	0.0075	$9.5 \pm 0.02$
<b>ZnS:Mn/SiO<sub>2</sub></b>	0.27	$1.776 \pm 0.007$	0.018	$24.6 \pm 0.08$
<b>ZnS:Mn/SiO<sub>2</sub> x10</b>	0.27	$1.9 \pm 0.05$	0.015	$20.96 \pm 0.08$

Table 8.3: Lifetimes for the orange emission due to the  $\text{Mn}^{2+}$  at 590 nm.

	$A_1$ [au]	$\tau_1$ [ $\mu\text{s}$ ]	$A_2$ [au]	$\tau_2$ [ $\mu\text{s}$ ]
<b>ZnS:Mn</b>	0.083	$1000 \pm 50$	0.073	$214 \pm 16$
<b>ZnS:Mn x10</b>	0.022	$1030 \pm 150$	0.011	$111 \pm 51$
<b>ZnS:Mn/SiO<sub>2</sub></b>	0.034	$1710 \pm 100$	0.018	$242 \pm 27$
<b>ZnS:Mn/SiO<sub>2</sub> x10</b>	0.24	$2600 \pm 500$	0.015	$287 \pm 110$

The decay time for the  $\text{Mn}^{2+}$  emission in bulk ZnS is 1.8 ms [Gum81]. Different lifetimes for nanoparticles have been reported since the interest in these materials increased. Bhargava *et al* were the first to publish lifetime measurements on  $\text{Mn}^{2+}$  doped ZnS nanoparticles [Bha94/2, Bha96]. They observed a lifetime shortening from ms to ns. This was also described by Sooklal *et al* [Soo96]. Bol *et al* were the first to report a multi exponential decay for the  $\text{Mn}^{2+}$  emission. They observed besides decays of 40 and 250 ns also a longer decay of about 0.4 ms [Bol98], this was confirmed by the group of Murase [Mur99]. Bol and Murase also measured the lifetimes of the blue ZnS emission. The group of Bol measured lifetimes of 50 and 200 ns, that means lifetimes in the range of the  $\text{Mn}^{2+}$  emission. Murase could with their setup measure lifetimes down to 10 ns. Our measurements confirm the lifetime results for the blue emission of Murase, like Bol and Murase we also measure a ms lifetime for the  $\text{Mn}^{2+}$  emission. But we did not observe ns lifetimes for the orange emission, and also the long (200 ns) lifetime for the ZnS emission could not be observed.

That there are different results for the lifetime measurements can be due to different setups used for the measurements and to the way in which the obtained data were analysed. Ns lifetimes are not observable without a suitable laser set up. How data analysis influences the results can already be seen for the measurements made at the CSEM at Neuchatel. Analysis supposing a mono exponential decay results not in the same value as for the assumption of a bi exponential decay.

Another reason is the fact that we do not measure the same particles. Optical properties are often influenced by the chemical environment. So a different surfactant used for the particle synthesis can already change the luminescence lifetimes. This can also be seen for the measurements made on the "naked" and the  $\text{SiO}_2$  coated particles. The coating leads to an increase of the lifetimes for the blue as well as for the orange emission (see table 8.2 and 8.3), which corresponds to the increase of the quantum yield observed (see section 8.1.4)

In section 8.1.2 we tried to find out if the luminescence quenching observed was of a dynamic quenching or a static quenching nature. Measurements of the quantum yield at different temperatures gave no coherent results and we referred to the possibility to draw conclusions from the lifetime measurements.

If a dynamic quenching would be present for our samples we should observe a

variation of the fluorescence lifetimes with dilution for static quenching not (see section 2.1.4). This is due to the fact that the dynamic quenching depopulates the excited state, whereas the static quenching does not. Static quenching takes a part of the fluorophores out of the system by complex formation. They are not excited and they do not emit, so static quenching does not influence the excited state and so there should no concentration dependence of the lifetimes be observable.

The luminescence quenching of the particles were only investigated for the  $\text{Mn}^{2+}$  emission. With a look at table 8.3 we see that for the  $\text{SiO}_2$  coated particles the lifetimes increase with dilution. This would indicate dynamic quenching. For the cysteine coated particles this not the case.  $\tau_1$  shows only a variation with dilution that is within the statistical error. For  $\tau_2$  we even observe a decrease for the lifetime of almost 50 %. So also with lifetime measurements we do not obtain coherent results.

We also calculated the mean free path and with this the time a particle needs to collide with another particle. For the not diluted dispersions the mean free path was 350 nm and for a collisional quenching we needed at least a luminescence lifetime of 40 ms (see section 8.1.3). So the possibility of a collisional quenching can be excluded with a maximum lifetime of 1 ms measured for the  $\text{Mn}^{2+}$  emission. A static quenching process is also not possible since the lifetimes should be constant for different luminescence intensities which is not the case for our particles.

With the measurements made in the framework of this thesis it was not possible to draw a final conclusion on the quenching mechanism for the quenching due to dispersion concentration. Since it seems to be neither dynamic nor static quenching other effects must be responsible for this phenomenon. In literature whole lists can be found with quenching substances. Since we saw in section 6.5 that there is a large unknown rest present in the powders it is possibly that impurities in the dispersions are responsible for the quenching by a mechanism that is neither dynamic nor static. Another possibility could be that there are agglomeration phenomena present at high concentrations that lead to quenching, but this should normally be visible in the particle size distributions measured.

What can be seen with the lifetime measurements is that the luminescence decays are not mono exponential but at least bi exponential. It is not possible to explain this without knowing the exact recombination mechanism of the electrons in the particle. We can approximate the decay to consist of two populations, but this is only an approximation.

For the  $\text{Mn}^{2+}$  emission that can be explained by the fact that we have very small particles with a large surface to volume ratio. So the two populations we observe could be due to the recombination that take place near the surface and at the surface, and the second could result from recombination in the bulk. But with particles that small nearly every atom in the particle will experience a different electric field, and can thus result in a different lifetime. So it is more likely that

instead of having two populations with two distinct lifetimes, there is a lifetime distribution underlying the two populations that we can resolve with the setup used for these measurements.

For the blue ZnS emission different particles sizes could be responsible for this since the particle size influences the electronic structures of the particles in this size region.

It is in anyway interesting to remark, that the luminescence of the blue ZnS emission is more intense than was expected from the luminescence measurements. This is probably due to a lower sensitivity of the luminescence detector in the UV. So the peak we obtain for the ZnS emission is only a small part of a peak much more intense. So the ratio between the peak intensities of the two emissions depends strongly on the spectrometer and its detector with which the luminescence is detected. This could be seen when the same sample was measured on different fluorescence spectrometers, where we obtained different ratios of the peak intensities for the manganese and the ZnS emission

With this additional knowledge we have to consider a higher loss of quantum yield due to emission directly over the band gap.

From the lifetimes one can attribute the ZnS emission to a fluorescence recombination process and the  $\text{Mn}^{2+}$  emission to a phosphorescence mechanism. This makes sense when we take into account, that the recombination for  $\text{Mn}^{2+}$  emission passes via an actually quantum mechanically forbidden step, which is the case for most phosphorescence mechanisms.

### 8.3 Photo bleaching

One of the disadvantages of organic dyes is the so called photo bleaching, which is the irreversible destruction of the fluorophore under illumination. Often organic dyes have to be handled in the dark and to be stored at low temperatures because they bleach in the sun light. We compared our particles with fluorescein, which is well know and an frequently used organic dye, and with the Alexa-350 fluorophore. The Alexa fluorophores are a series of dyes that cover the whole visible spectrum and have been developed to overcome the disadvantage of photo bleaching.

For the comparison, solutions of the two dyes have been made and measured for their emission, the same for a freshly prepared particle dispersion. The samples have been remeasured after three and four days of exposure to sun light at room temperature respectively. After four days a decrease of particles emission of 9 % has been observed, for the fluorescein the decrease was 23 % and for the Alexa-350 8 %.

This shows that, where photo stability is concerned, we are in the same range as the best dyes available at the moment. The particles do not have to be stored at low temperatures, but can be kept at room temperature in a transparent beaker.



The coated particles even showed an increase in fluorescence quantum yield after three months, which can be seen in figure 8.19.

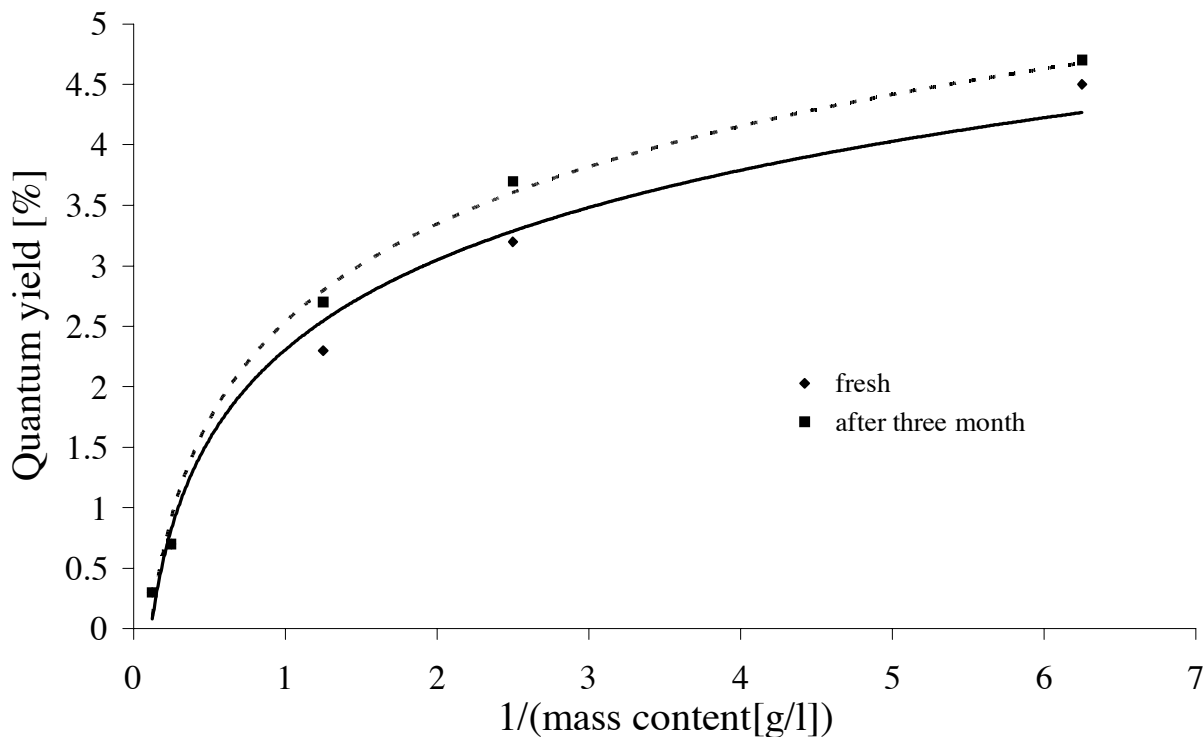


Figure 8.19: Quantum yields for coated particles.

## 8.4 Doping metals

To do multicolour experiments with organic fluorophores one needs a laser for every emission colour, since for these fluorophores excitation and emission spectra are very close. Inorganic nanocrystals can overcome this problem. In our case the doping with different colours would lead to a series of particles, all excitable at 310 nm, but with different emission colours. The ideal case would be a doping with  $\text{Ag}^+$  (blue emission, 440 nm [Iga02]),  $\text{Cu}^{2+}$  (green emission, 470-500 nm [Bol02]),  $\text{Mn}^{2+}$  (orange emission, 585 nm [Gum81]) and  $\text{Eu}^{3+}$  (red emission, 620 nm [Sun98]).

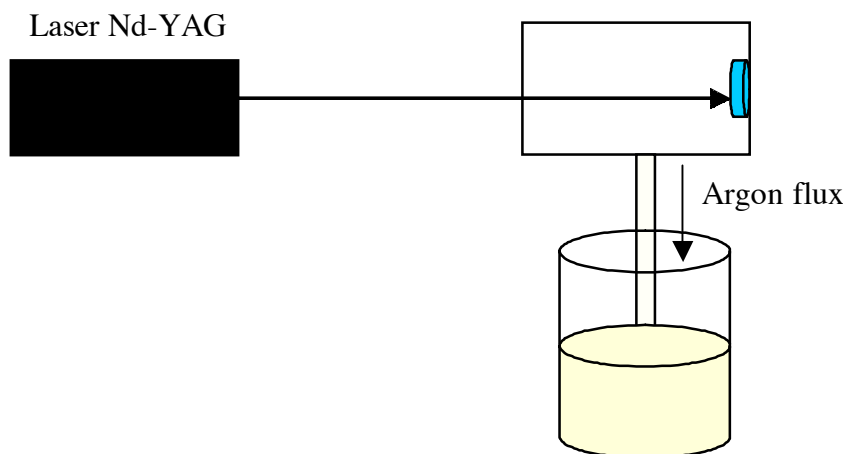


Figure 8.20: Schematic setup of the LINA-Spark Atomizer.

The thesis treats the ZnS:Mn system as a model system, but we also tried to dope with other metals. The reason for the efficient doping for the ZnS:Mn case lies in its solubility products. MnS has a solubility product ( $1.7 \cdot 10^{-16} \frac{\text{mol}^2}{\text{l}^2}$  [Hol95]) which is higher than the one for ZnS ( $1.1 \cdot 10^{-24} \frac{\text{mol}^2}{\text{l}^2}$  [Hol95]). So when the  $\text{Na}_2\text{S}$  solution is added to the  $\text{Zn}^{2+}/\text{Mn}^{2+}$  mixture the ZnS precipitates and in doing so incorporates the Mn in its lattice. For the dopant metals mentioned above, this is not possible because their solubility products are smaller than the one of ZnS, so the dopant sulphide precipitates first and no incorporation in the ZnS lattice takes place, but one obtains a mixture of two separate sulphides. This could be seen best for a  $\text{Zn}^{2+}/\text{Cu}^{2+}$  mixture. Since the CuS is black, the CuS precipitation before the white ZnS precipitate could be observed.

For this reason it was tried to physically dope the ZnS with a laser process. For this the LINA-Spark Atomizer, developed at the Powder Technology Laboratory, was used. The LINA-Spark is a short lived argon plasma, induced by a laser pulse. Generated at the surface of the sample, it evaporates some material, which is then transported in an argon flux, and is then normally deposited on a membrane (see figure 8.20).

HRTEM images of the deposition on the filter showed primary particle sizes of about 5 nm, which is in the range of what we obtain with chemical precipitation. To produce nanoparticles with this laser process ZnS was co precipitated with the sulphide of the metal we wanted to dope it with. Pills were pressed with the powder which could then be used as samples in the atomizer. The material was deposited on a membrane and then characterized for its composition and structure. The characterization showed no change in crystal structure or composition of the sample during the laser ablation. The optical characterization of the deposition showed, that powders that were luminescent before the laser ablation, were also luminescent afterwards (ZnS:Mn), but powders that did not show a

luminescence before the laser process were not doped in the laser process, and so showed no fluorescence afterwards (ZnS:Ag, ZnS:Cu, ZnS:Eu). This indicates, that instead of a real atomization of the sample in the plasma, we have rather an ablation of parts of the sample that are then transported to the membrane, so it is not possible to introduce the dopant metal in the ZnS matrix.

Since the optical properties are not changed in the process and fluorescent samples of the compositions mentioned above can be bought, it would be possible to buy luminescent samples and produce nanoparticles via laser ablation. So we tried to stabilize the ZnS:Mn ablation in a surfactant solution. As surfactants PEI (polyethylenimid), cysteine and PVP (polyvinylpyrrolidon) were used. The dispersions obtained were only stable for 2-3 hours, and PCS measurements showed particles or agglomerates with sizes between 500 and 1000 nm. The primary particles of about 5 nm that could be seen for other ablations could not be seen in dispersion, but agglomeration occurred most probably during the transport in the argon flux. This could be prevented by the use of an aerosol of, for example a cysteine solution, to inhibit the agglomeration during the process.

To conclude, the doping of the ZnS with the LINA-Spark atomizer is not possible, but the process does not alter the optical properties of a already luminescent material. So the process could be used to produce nanopowders with already doped bulk samples. For this one would have to stabilize them directly in a surfactant solution and try to prevent agglomeration during the transport.

## 8.5 Conclusions and discussion

For the application as biosensors the optical properties of the ZnS:Mn nanoparticles are the most important of the particle's characteristics. They have to compete with organic dyes that have quantum yields of sometimes even 100 %. This cannot be achieved with nanoparticles. But they have other advantages. The most prominent is the large Stokes shift between excitation and emission. It is often difficult to measure the fluorescence emission of organic dyes without also measuring the excitation peak, since the excitation and emission spectra are normally very close (see figure 1.2). In the last chapter the optical properties of the particles have been investigated.

It was observed, that the luminescence intensity and also the quantum yield increases with dilution of the dispersions. This phenomenon is called fluorescence quenching. One distinguishes between a dynamic and a static quenching mechanism. The dynamic mechanism depending strongly on the diffusion of the particles in dispersion, should show dependence of the quantum yield on temperature and of the luminescence lifetime on the concentration.

Quantum yield measurements at three different temperatures (5, 25 and 35 °C) showed an increase of the quantum yield with a decrease in temperature. This is not only due to an increase in luminescence emission but also to a decrease

in absorption with lower temperatures. This comes from the temperature dependence of the extinction coefficient of a solution. To get rid of these effects the Stern-Volmer plot is used, where normally the ratio of luminescence without and with quencher is plotted against the quencher concentration in the sample. Since in our case the quencher is part of the system we plotted the ratio of the luminescence for the highest dilution to the luminescence of lower dilution versus the dispersion mass content. The so obtained Stern-Volmer plots are very close together and show no clear difference for the three temperatures, so that no conclusions can be made with these measurements. It is possible, that the differences in temperature were not high enough, or that there is another quenching mechanism present in the sample.

Another method to check on the quenching mechanism are lifetime measurements. For collisional quenching the lifetimes should increase with diluting the dispersion for static quenching the dilution of the samples should not influence the lifetimes. So the behaviour of the luminescence lifetimes with dilution of the dispersions has been investigated. An increase of the luminescence lifetimes for the orange emission has only been observable for  $\tau_1$  of the coated particles. For the uncoated particles the lifetimes either decrease or the changes are within the statistical error. This does not prove a collisional quenching, but since the lifetimes change with dilution it is no static quenching either, since for this the lifetimes should be constant for different concentrations. So for both methods applied to verify the quenching mechanism, the obtained results are not coherent.

When thinking of a collisional quenching, the most likely mechanism would be the loss of excitation energy during collisions between two particles. For this the particles have to collide during the lifetime of the excited state. The longest lifetime for the orange  $\text{Mn}^{2+}$  emission is 1 ms. The mean free path of the particles at highest concentration was calculated to be 350 nm. With the Stokes-Einstein equation it was possible to calculate the velocity of the particles, and with this the time a particle needs for 350 nm. This time was calculated to be 45 ns. This finally proves that the collisional quenching mechanism is not present in the sample.

Since the lifetime results excluded the possibility of a static quenching it is not possible to make a definite statement on the quenching mechanism. It is likely that there are other effects than a simple static or dynamic quenching responsible for the quenching. This could for example be agglomeration phenomena at high particle concentrations. Another possibility could be a quenching due to the large unknown rest in particle composition found in section 6.5.

There is a second luminescence quantum yield phenomenon present in the particles. When the manganese content in the particles is increased the luminescence quantum yield increases first to a maximum value and decrease then with further addition of the dopant. This could be explained for example by a preferred adsorption of the manganese at the particle surface instead of incorporation in

the particle from a certain concentration on. Another reason could be the formation of separate MnS particles. A quenching mechanism, called concentration quenching, can be excluded, since there is not even one  $\text{Mn}^{2+}$  ion present in every particle.

Lifetime measurements of the particles revealed some interesting facts. The blue ZnS and the orange  $\text{Mn}^{2+}$  emissions were measured and it was shown that the blue emission has very short lifetimes in the ns region and a higher intensity than the manganese emission. This is interesting because with the measurements possible with our spectrometer the blue emission is less intense than the orange emission, so that we considered the loss of quantum yield due to this emission as small. With these measurements we saw that the fluorescence from this transition is intense but it decays too quickly to be registered by our photometer.

Two lifetimes could be determined for each transition, but it is more likely that we actually have a lifetime distribution, since the lifetimes vary with the electronic neighbourhood, which can vary a lot in a nanocrystal. Due to the large surface to volume ratio the  $\text{Mn}^{2+}$  can have different lifetimes according to its position in the particle. The different lifetimes for the blue ZnS emission could be due to the particle size distribution.

That the lifetimes change with the chemical and so electronic environment can for example be seen for the coated particles. Here, in the emission spectra an increase of the blue emission intensity can be observed for the coated compared to the not coated particles. This is accompanied by a lifetime and quantum yield enhancement of the coated particles. The increase of the quantum yield by a factor of three is attributed to the saturation of dangling bonds at the particles surface with the coating.

The photo stability of the particles was compared with fluorescein and the Alexa-350 fluorophore which is part of a series of the most photostable fluorophores available at the moment. The photostability of the particle is in the same order of magnitude as the Alexa-350 where the decrease of the fluorescence under irradiation is concerned. The coated particles even show an increase in luminescence quantum yield after three month at room temperature and constant irradiation of sun light.

So the synthesized particles show quantum yields depending on the dispersion concentration and the manganese content in the particles that can be increased by a factor of three by coating the particles with a  $\text{SiO}_2$  shell. Lifetime measurements showed nanosecond lifetimes for the blue emission indicating a fluorescence process for the recombination over the band gap. The lifetimes for the orange emission go up to milli seconds which is in the region of phosphorescence lifetimes. A phosphorescence mechanism is normally related with an intersystem crossing from a singlet to a triplet state, so that the final recombination of the electron and the hole is spin forbidden. In our case the  ${}^4\text{T}_1 \rightarrow {}^6\text{A}_1$  is forbidden by the Laporte rule, which forbids transitions between states of same parity (which forbids all  $d \rightarrow d$  transitions). The orange phosphorescence is ideal for a

biosensor, since it can easily be detected when the background fluorescence has decayed. The particle stability against photo bleaching is comparable with the photostability of the most photostable organic dyes.

## Chapter 9

# Final conclusions and discussion

The goals formulated at the beginning of this work have been the synthesis and characterization of doped ZnS nanoparticles in aqueous dispersion for application as a biosensor in biological and medical analytics. They should be doped with different doping metals to have the opportunity to perform multicolour experiments with a single excitation wavelength, corresponding in our case to the excitation over the ZnS band gap. The particles should be characterized for their chemical composition, their particle size and their optical properties. For the optical properties the quantum yields and fluorescence lifetimes were of special interest. Finally, the particle should be biofunctionalized to allow the attachment of biomolecules.

In the framework of this thesis a synthesis of  $\text{Mn}^{2+}$  doped ZnS particles in aqueous dispersion has been developed and cysteine was used as surfactant. IR spectroscopy indicates that the cysteine is attached to the particle surface via the mercapto group. This also seem likely in view of the high affinity of mercapto groups to ZnS. A second interaction with the particle surface via the amino group is very probable since this would lead to the formation of a chelate complex which is energetically favoured. To confirm this, solid state NMR measurements could be helpful. Since it has already been seen for mercapto stabilized gold particles we also assume a covalent bonding of the cysteine to the surface. This is also encouraged by the decomposition of the cysteine at the particle surface instead of a desorption of the molecule as a whole, and the fact that the  $\text{SO}_2$  evaporates last. When the powders are isolated by addition of cold ethanol a high amount of cysteine can be detected afterwards with elemental analysis which indicates also a covalent bonding.

At a pH of 8.5, which corresponds to the pH of the dispersions after dialysis, the amino as well as the carboxylic group are ionised. The free  $\text{COO}^-$  group at the particle surface is a good starting point for a particle functionalization. But first attempts to biofunctionalize them via this group showed a strong sensitivity of the synthesized particles to changes in ionic strength. Even the addition of the smallest amount of a salt leads to particle flocculation. The dispersions are also

very sensitive to changes of the pH. For pHs smaller than 8 agglomeration starts. Since the particles are stabilized electrostatically the addition of salts leads to the screening of the stabilizing double layer and thus to flocculation of the dispersion. The pH effect can also be explained by this effect but a second point could be the protonation of the SH group at pHs smaller 8. To overcome these problems tests have been made in the framework of another thesis to obtain higher stabilities by addition of polyelectrolytes, where not only electrostatic but also steric effects have to be considered responsible for stabilization.

The chemical composition of the particles was investigated by means of titration, CHNS analysis and AES for ethanol isolated and freeze dried powders. The complete composition could not be obtained, but the ZnS and cysteine content in one gram powder could be determined. The large unknown rest in the freeze dried samples as well as the ethanol isolated ones is probably due to rests of the precursor salts such as sodium, sulphate, etc. Since these impurities can influence the optical properties of the particles it would be important to further purify the samples since a simple dialysis seems insufficient. For this a chromatographic system has been used leading to purer samples. This has also been done in the framework of a second thesis.

For multicolour experiments the particles should be doped with additional transition or rare earth metals. This could not be achieved by chemical coprecipitation, since the sulphides of suitable metals showed a smaller solubility product than ZnS which leads to the formation of a separate doping metal sulphide instead of incorporation in the particles. To overcome this problem we tried to dope the particles physically via a laser process. This showed that powders that already were luminescent before the laser ablation stayed luminescent, but that a doping of non luminescent powders during the process was not possible. It was also difficult to stabilize the ablated particle in aqueous dispersion. The agglomeration during the transport of the powders could perhaps be prevented by transporting the powders in a surfactant containing aerosol instead of argon. To prevent agglomeration during discharging in the surfactant solution an ultrasonic bath could be helpful. On all accounts, when the agglomeration problem can be solved this would be an elegant method to produce luminescent particles in aqueous dispersion starting from luminescent powders that are available on the market. The particles have been coated with an inorganic SiO<sub>2</sub> shell. This coating was performed on the one hand for further stabilizing the particles and on the other hand to passivate the particle surface. The coating performed leads not to single particles coated with a shell but to the formation of beads, that means several particles incorporated in a SiO<sub>2</sub> matrix. This increased the long term stability from 3-4 weeks to several months. But the dispersions were still sensitive to changes in the ionic strength and pH.

The passivation of the surface is important for the optical properties of the particles. A lot of emission is lost due to radiationless recombination of the electron and the hole at the particle surface where so called "dangling bonds", that means



unsaturated valences, act as electron traps. An inorganic capping saturates these bonds and leads to an increase of the quantum yield. In our case the quantum yield increased by a factor of three.

Measuring particle sizes of particles smaller than 10 nm is difficult since most of the commonly used methods such as PCS reach their detection limit in this size region. So the most commonly used method to determine particle sizes for nanoparticles is TEM. But also here one has to pay attention when evaluating the result since there are artefacts due to sample preparation. So it cannot be excluded that agglomerates that can be observed were formed during the drying of the dispersion on the TEM grid. It is also often observed that bigger particles can mainly be found at the outer rim of the grid and the smaller ones in the middle, in any way it is difficult to get an idea of the particle size distribution with TEM micrographs. To overcome this problem we applied different methods to determine the particle size. Asymmetric flow field flow fractionation (aF-FFF), analytical ultracentrifugation (AUC), photon correlation spectroscopy (PCS) and TEM images. We calculated an optical particle size based on the shift of the band observed with UV/vis measurements and the crystallite size based on the peak broadening for x-ray diffraction patterns (XRD). All the mentioned methods have their problems. So, PCS measures not only the particles in dispersion, but also the impurities that are present in the sample. So they have to be centrifuged or filtered to get rid of dust which of course also alters the particle size distribution since it cannot be excluded that one eliminates not only dust but also big particle agglomerates. The AUC results depend strongly on the dispersion concentration and particle density, so an extrapolation for infinite dilutions has to be made and a particle density to be estimated. But the combination of all these methods allows a realistic statement on the particle size.

With AUC, aF-FFF, TEM and PCS the main particle size distribution in the dispersions was determined to go from 3-20 nm with its first maximum at 5 nm. But there are also bigger particles or agglomerates present in the sample which leads to a second maximum at about 17 nm. This result corresponds well with the distribution obtained with TEM, so besides its disadvantages TEM is the fastest methods to get a good idea of the particle size.

The results for calculations based on XRD and UV/vis measurements are in the same region but smaller than what was measured with the other methods. For the XRD results this is known, since this method determines the size of the crystal domains within a particle and not the actual particle size. Since the exciton Bohr diameter for ZnS is 5 nm and most of the particle have been determined to have particle sizes bigger than 5 nm, and since we observe nevertheless a shift of the onset of absorption, we think that the quantum size effect refers also to crystal domains. So a blue shift of the absorption does not necessarily mean that the particles are smaller than the exciton Bohr diameter.

For an application as biosensors the optical properties, especially the quantum yields, of the synthesized particles are of high interest. Quantum yield measure-

ments showed quenching phenomena for the particles and particle dispersions. The luminescence quantum yields depend on the dispersion concentration. The higher the concentration the lower the quantum yield. The second phenomenon affects the  $\text{Mn}^{2+}$  content in the particles.

For the concentration dependence of the quantum yield of the particle dispersions we checked two possible mechanisms for the quenching. Dynamic or collisional quenching, where the quenching is due to collisions between the quencher and the fluorophore. Or static quenching, where the quenching results from the formation of a non fluorescent complex between the quencher and the fluorophore. For this measurements at different temperatures have been made. The effect of the collisional quenching should become stronger for higher temperatures since it is a diffusion dependent phenomenon, for the static quenching the effect should become less pronounced since higher temperatures introduce higher vibration energy in the complex which leads to the destruction of the complex. These measurements did not add to coherent results, probably because the temperature differences for the measurements were not pronounced enough, but it was not possible to perform low temperature measurements with the equipment at our disposition. Another possibility to distinguish between dynamic and static quenching are lifetime measurements. Lifetimes do not depend on the fluorophore concentration. This is still the case when static quenching is present in a sample. When dynamic quenching occurs this changes since the quenching depopulates the excited state. So for dynamic quenching the lifetime increases with decreasing concentration. But likewise the temperature measurements the lifetime results were not coherent. But we determined a maximum luminescence lifetime of about 1 ms for the orange manganese emission. In the case of collisional quenching the most likely mechanism would be quenching due to collisions between two particles. So we calculated the mean free path, and with the diffusion coefficient the velocity of the particles. With the help of these calculations we saw that we would need a lifetime of about 40 ms for the excited state for dynamic quenching to be effective. So dynamic quenching due to particle - particle collisions can be excluded. Finally it is not possible to make a statement on the quenching mechanism. Since the lifetimes change with dilution of the dispersions static quenching is not very likely.

We reported the presence of a large unknown rest in the particle composition so it could be possible that these impurities are responsible for the quenching. Another possibility could be agglomeration effects at high concentrations. Definitely, it could be helpful to investigate once again the temperature dependence but at low temperatures, or to vary the viscosity of the dispersions since this should have the same effect on the quenching as the temperature. Lower viscosities should favour collisional higher viscosities static quenching.

The behaviour of the quantum yield with the manganese content shows an interesting feature. It increases first with increasing  $\text{Mn}^{2+}$  content, reaches then a maximum to then decrease. This development of the quantum yield with the

$\text{Mn}^{2+}$  concentration can be explained either by a preferred adsorption of the  $\text{Mn}^{2+}$  at the particle surface or the formation of separate MnS particles at higher manganese concentrations. A possibility proposed in literature is the so called concentration quenching. Concentration quenching involves resonant transfer of electronic excitation energy from the initially absorbing ion to another identical ion and, after a number of energy transfer steps, to a quenching site (for example a defect). A problem with this theory is the fact, that we do not directly excite the manganese impurity, but the ZnS host. For the energy transfer the emitted radiation would necessarily directly excite the manganese. We tried to do this with the spectrometer, and it was not possible. But this does not prove that this quenching mechanism is not possible. Another problem is the fact that the concentration of the dopant metal must exceed a limiting value, so that the distance between the  $\text{Mn}^{2+}$  ions gets small enough for this transfer to take place. With ICP measurements we saw that even for the highest doping percentage there is not even one manganese ion in every particle. Magnetization measurements showed that the  $\text{Mn}^{2+}$  is homogenously distributed in the particles, so that concentration quenching can be excluded. For a further investigation of the distribution and location of the  $\text{Mn}^{2+}$  in the particles electron spin resonance (ESR) measurements could be helpful.

The observed increase of the quantum yield for the  $\text{SiO}_2$  coated particles compared with the cysteine coated ones can also be observed for the lifetime measurements. Here the  $\text{SiO}_2$  coated particles show a longer lifetime of the excited state than the cysteine coated particles.

The results for nanosecond lifetime measurements showed lifetimes from the micro- to the millisecond region for the orange  $\text{Mn}^{2+}$  emission. This is perfect for applications as biosensors, because this leads to an excellent signal to noise ratio and measurements are possible with a simple flash lamp setup. The lifetimes for the blue ZnS emission go from 1 to 20 ns. This indicates a fluorescence recombination mechanism for the ZnS emission and phosphorescence mechanism for the manganese emission.

Photo bleaching tests showed photostabilities comparable with the Alexa fluorophores which are the most photostable fluorophores available on the market at the moment.

To refer once again to the goals formulated at the beginning of this PhD work, we synthesized particles in aqueous suspension and investigated them for their particle size, composition and optical properties. There has no final answer for the quenching problem been found, but collisional quenching can be excluded. Doping with additional metals was not achieved but first promising tests with a laser process have been carried out. The biofunctionalization of the particles was, for a lack of time, not possible in this work. It will be the subject of another thesis. In this thesis the stability problems that occur with the synthesized particles are also investigated since they complicate the attachment of biomolecules.

Are the synthesized particles apt to replace organic dyes as biosensors? Surely not in the present form.

There stability causes problems for the biofunctionalization, since for a lot of coupling reactions a neutral or acid pH is necessary, which leads in our case to flocculation of the particles. The application in biology and medicine demands stability in media with different and high ionic strengths. This can not be provided with the synthesized particles. The particles have not yet been biofunctionalized for exactly these reasons. The excitation wavelength of 310 nm leads to expensive setups, since for the applications of the particles on a waveguide a flash lamp can not be used, and so a UV laser would be necessary. Also the excitation wavelength can cause problems when the particles have to be excited in cell cultures for example, which can be destroyed by UV laser light. The luminescence intensity is a lot smaller than the one for organic dyes and the development of the new Alexa fluorophores have overcome the problem of photostability for organic dyes.

All these reasons argue against the use of the synthesized particles as biosensors. But besides all this, fact is, that multicolour experiments will never be possible with organic dyes, and in anyway, another system has to be used for this.

So there may still be a lot of research necessary, but a lot of the problems mentioned above can be overcome. In another thesis at our lab experiments have already been carried out with good results, to further stabilize the particles with polyelectrolytes. Biotin has already been attached to the surface. The disadvantage of smaller luminescence quantum yields compared with organic dyes can be overcome with the longer lifetimes. The luminescence intensity can be detected without any problems beside the background luminescence due to a good signal to noise ratio. The large stokes shift makes the separation of excitation and emission easy which is always a big problem with organic dyes.

A bigger problem is the excitation wavelength. To shift it into the visible region, one has to change the system. For example manganese doped CdS could be a solution for this. This system has a excitation wavelength of about 400 nm with the same characteristic manganese emission at 585 nm. So the stokes shift would still be sufficient to easily separate excitation and emission. The experience and knowledge acquired with this work could be used to synthesize the CdS:Mn system even though the synthesis can not be transferred one to one to a new system since it is very sensitive to pH and solubility products.

So we still have the problem of doping the particle with other transition metals. The laser experiments carried out, show that is possible to find processes to achieve doping with different dopants. With already doped material, nanoparticles could be obtained with the LINA-Spark atomizer, if one can find a way to stabilize them so that they do not agglomerate during the transport.

So if the goal is to carry out multicolour experiments on waveguides, it is worth to continue the research on this kind of material. For other applications like for example luminescence detection in cell cultures, it is in my opinion not likely

that the inorganic nanoparticles will replace organic dyes, for which the coupling reactions to biomolecules are well known and already automated.

# Appendix A

## List of symbols and abbreviation

### A.1 Symbols

$\beta_{\frac{1}{2}}$	Full width at half maximum
$\Gamma$	Emissive rate of the fluorophore
$\delta$	Thickness of adsorbed layer
$\varepsilon$	Dielectric constant
$\varepsilon_0$	Electric permittivity of the vacuum
$\varepsilon_r$	Relative permittivity of the medium
$\eta_L$	Viscosity of the suspending liquid
$\eta_s$	Solvent viscosity
$\Theta$	Scattering angle
$\theta_B$	Bragg angle
$\lambda$	Wavelength
$\lambda_0$	Wavelength of the laser
$\lambda_{em}$	Emission wavelength
$\lambda_{ex}$	Excitation wavelength
$\mu_B$	Bohr magneton
$\nu$	Frequency
$\bar{v}$	Partial specific volume
$\rho_p$	Particle density
$\rho_s$	Solvent density
$\sigma$	Surface tension, collision cross section
$\sigma^0$	Surface tension without adsorption
$\tau$	Lifetime
$\tau_0$	Intrinsic lifetime
$\Phi$	Quantum yield
$\Phi_R$	Quantum yield of the reference
$\Phi_S$	Quantum yield of the sample
$\psi$	Electrostatic potential

$\psi_0$	Electrostatic potential at the surface
$\omega$	Centrifugal velocity
A	Number of lattice plane
$A_H$	Hamaker constant
$A_R$	Absorbance of the reference
$A_S$	Absorbance of the sample
$a_B$	Exciton Bohr radius
C	Curie constant
c	Concentration
$c_0$	Concentration without potential
D	Diffusion coefficient
$D_f$	Diffusion coefficient of the fluorophore
$D_q$	Diffusion coefficient of the quencher
d	Diameter
$d_r$	Diameter to a corresponding $r_r$ and $s_r$ value
$d_{aa}$	Distance between two atoms or molecules
$d_{hkl}$	Distance between adjacent planes of a series
$E_g$	Energy gap
e	Elementary charge
$[F]$	Concentration of the uncomplexed fluorophore
$[F]_0$	Total fluorophore concentration
$[F - Q]$	Concentration of the formed complex
F	Fluorescence Intensity with quencher
$F_0$	Fluorescence intensity without quencher
$F_B$	Buoyancy force
$F_C$	Centrifugal force
$F_F$	Frictional force
f	Concentration and shape dependant frictional coefficient
$f$	Fraction of fluorophore not complexed
$\Delta G^{att}$	Free attractive energy
$\Delta G_{elst}$	Electrostatic free energy
$\Delta G_{LJ}$	Lennard-Jones-Potential
$\Delta G_{pot}$	Potential free energy
$\Delta G^{rep}$	Free repulsive energy
g	Lande factor
H	Distance between two flat surfaces
$H_{pd}$	Distance between particle and detector
h	Planck's constant
I	Ionic strength
$I_0$	Incident light intensity
$I_S$	Intensity of the scattered light
K	Dissociation constant
k	Rate of radiationless decay

$k_0$	diffusion-controlled bimolecular rate constant
$k_B$	Boltzman's constant
M	Molecular weight
$M_P$	Molecular weight of a particle
m	Mass
$m_0$	Mass of the electron at rest
$m_e^*$	Effective mass of the electron
$m_h^*$	Effective mass of the hole
$m_P$	Mass of a particle
N	Number density
$N_A$	Avogadro's constant
$N_P$	Number of atoms in a particle
n	Order of reflection
$n_L$	Refractive index of the suspending liquid
$n_p$	Refractive index of particle
$n_R$	Refractive index of the reference
$n_{rel}$	Relative refractive index
$n_S$	Refractive index of the sample
$pK_a$	Acid constant
[Q]	Quencher concentration
R	Gas constant
$R_f$	Molecular radius of the fluorophore
$R_q$	Molecular radius of the quencher
$Ry^*$	Exciton Rydberg Energy
r	Radius
$r_r$	Radial position
S	Spin
s	Sedimentation coefficient
$s_r$	Sedimentation coefficient corresponding to a radial position r
T	Temperature
$T_C$	Curie-Weiss temperature
t	Time
$t_0$	Void time
$t_r$	Retention time
u	Sedimentation velocity
V	Volume
$\bar{v}$	Mean velocity
$V_0$	Volume of the separation channel
$\dot{V}_c$	Cross flow rate
$V_P$	Volume of a particle
$\bar{x}$	mean distance travelled in a certain time
Z	Collision frequency



z Distance from the surface

## A.2 Abbreviations

$\sigma$	Binding molecular orbital
$\sigma^*$	Antibinding molecular orbital
aF-FFF	Asymmetric field flow fractionation
AAS	Atomic absorption spectrometry
AES	Atomic emission spectrometry
AUC	Analytical ultra centrifugation
CHNS analysis	Carbon, hydrogen, nitrogen, sulphour analysis
DVLO theory	Deryagin-Landau-Verwey-Overbeek theory
EDTA	Ethylenediamine tetraacetic acid
FFF	Field flow fractionation
FWHM	Full width at half maximum
HPA	Heyl-phosphonic acid
HOMO	Highest occupied molecular orbital
HRTEM	High resolution electron microscopy
ICP	Inductively coupled plasma
IR	Infra red
LUMO	Lowest unoccupied molecular orbital
MPS	3-(Mercaptopropyl)trimethoxysilane
PCS	Photon correlation spectroscopy
PDS	Particle size distribution
PEI	Polyethylenimid
PhSeTMS	Phenyl(trimethylsilyl)selenium
PVP	Polyvinylpyrrolidon
QD	Quantum dot
QELS	Quasi electric light scattering
QY	Quantum yield
RT	Room temperature
TEM	Transmission electron microscopy
TEOS	Tetraethylorthosilicate
TGA	Thermogravimetric analysis
TOP	n-Trioctylphosphine
TOPO	n-Trioctylphosphine oxide
UV	Ultra violet
Vis	Visible
XRD	X-ray diffraction

# Appendix B

## Instrumentation

- **UV/vis-Absorption spectroscopy** The dispersions containing ZnS:Mn<sup>2+</sup> nanoparticles were placed into quartz cuvettes (1 cm) and characterized by optical absorption spectroscopy with a Perkin Elmer Lambda 900 spectrophotometer. The dispersing agent (0.01M NaOH or water) was used as reference.
- **Fluorescence spectroscopy** The luminescence results were obtained on a Hitachi F-4500 fluorescence spectrophotometer. The dispersions were placed in a 1x1 cm<sup>2</sup> quartz cuvette.
- **X-ray powder diffraction** X-ray powder diffraction patterns were measured using a Siemens Kristalloflex 805, applying the Cu K<sub>α</sub> radiation with  $\lambda = 1.541 \text{ \AA}$ . Samples for X-ray diffraction were prepared by placing the powder on a glass support.
- **X-ray diffraction at Ilford, Fribourg** The instrument used at Ilford for X-ray powder diffraction is a STOE Stadi P Transmission Diffractometer working with Cobalt K<sub>α1</sub> radiation from a primary Germanium (111) curved monochromator crystal (CoK<sub>α1</sub> : wavelength  $\lambda = 0.178896 \text{ nm}$ ). The cobalt X-ray tube runs at 45 kV and 30 mA.
- **Transmission electron microscopy** Samples for transmission electron microscopy were prepared by slowly evaporating the solvent of the nanocrystal dispersion on an amorphous carbon substrate supported on a copper grid. A Philips CM 20 transmission electron microscope operating at an accelerating voltage of 200 kV was used for TEM, a Philips CM 300 transmission microscope operating at 300 kV for HRTEM.
- **Photon correlation spectrometry** Particle size distributions were measured with the Brookhaven Zeta PALS/Zeta potential analyzer. For this the samples were placed in a 1x1 cm<sup>2</sup> diameter plastic cuvette and measured at an angle of 90° with a laser at 670 nm.

- **Zeta potential measurements** For this the Brookhaven ZetaPALS/Zeta potential analyzer was used. The sample was placed together with the electrode in a 1x1 cm<sup>2</sup> plastic cuvette.
- **IR-Spectroscopy** The IR spectra were recorded with a Nicolet 510 FT-IR spectrometer. For this the powder samples were pressed with a diamond on the sample holder. Liquid samples had to be dried with a heat gun before measuring.
- **Thermogravimetric analysis** TGA measurements were carried out with a Mettler TG 50 Thermobalance. For this the sample was placed in ceramic crucibles and inserted in the balance oven.
- **Thermogravimetric analysis coupled with FTIR** For this investigation a Netzsch STA 449 C/3/F Jupiter TGA was used coupled with a Perkin Elmer FT-IR Spectrometer Spektrum 1000.
- **Atomic absorption spectrometry** For the AAS measurements 1 g of powder was dissolved in 10 ml of 0.1M HCl and then diluted 100 times. The measurements were made with a Perkin Elmer 1100B Atomic Absorption Spectrophotometer.
- **Atomic emission spectrometry** The measurements were carried out with a Perkin Elmer emission spectrometer Plasma 2000, for this the samples were dissolved in 0.8 M HNO<sub>3</sub> and then injected in an ICP.
- **Analytical ultra centrifugation** The AUC measurements were carried out with a Beckmann AUC Optima XL-I ultra centrifuge. For this the sample is placed in a sector shaped measuring cell inside the rotor (prevention of convection). The sedimentation process can then be observed with different optical detection systems (UV/VIS absorption or Rayleigh interference optics).
- **Asymmetric flow field flow fractionation** The apparatus for the aFFF measurements was built in the institute of TANK. For the experiments a degenerated cellulose membrane was used. The solvent was water with 0.3 g/l NaCl and 0.08 g/l TWEEN.
- **CHNS analysis** These measurements were carried out with a Perkin Elmer 2400 analyzer. For this they were placed in a tin capsule and heated to a temperature of about 1700 °C.
- **Pycnometer** The density of the particle powders were determined with the Micromeritics AccuPyc 1330 pycnometer working with helium.

- **Squid measurements** Magnetization measurements were made using a SQUID magnetometer from Quantum Design, USA, at temperatures of 1.8, 3 and 300 K at fields from 0 T to 1 T.

# Appendix C

## Rietveld measurements

The spectra were measured and calculated with the  $\text{CoK}_{\alpha 1}$  radiation with a wavelength of  $\lambda=0.178896$  nm.

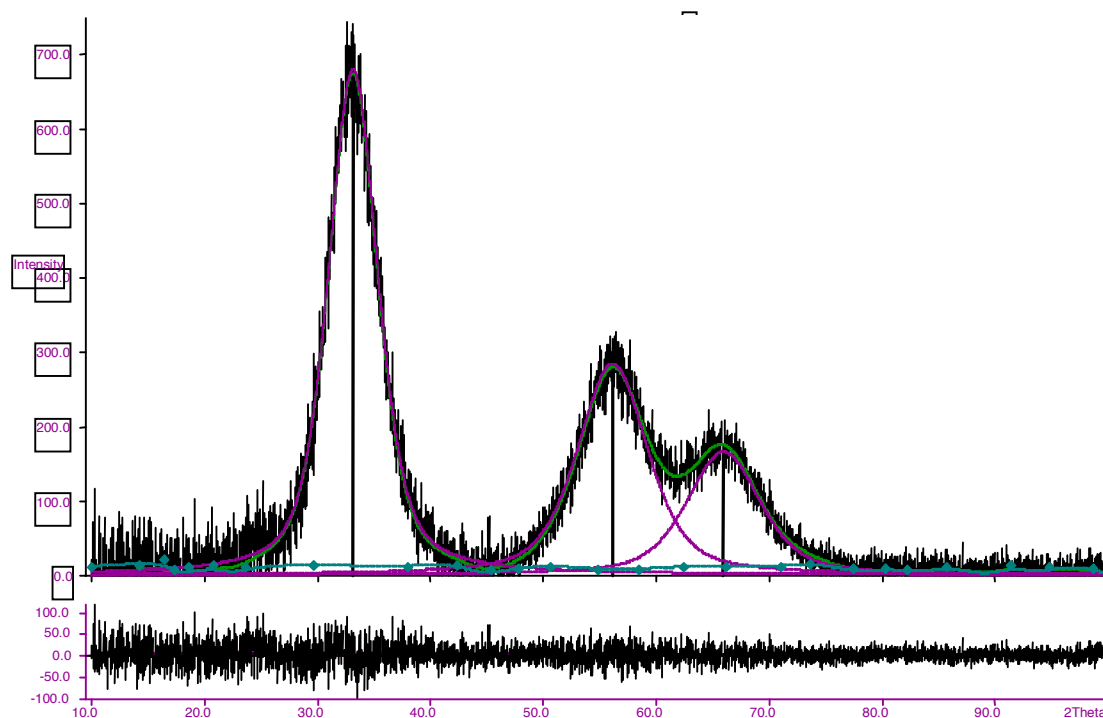


Figure C.1: XRD pattern for ZnS:Mn nanoparticles calculated with the rietveld method.

# Appendix D

## TGA-IR

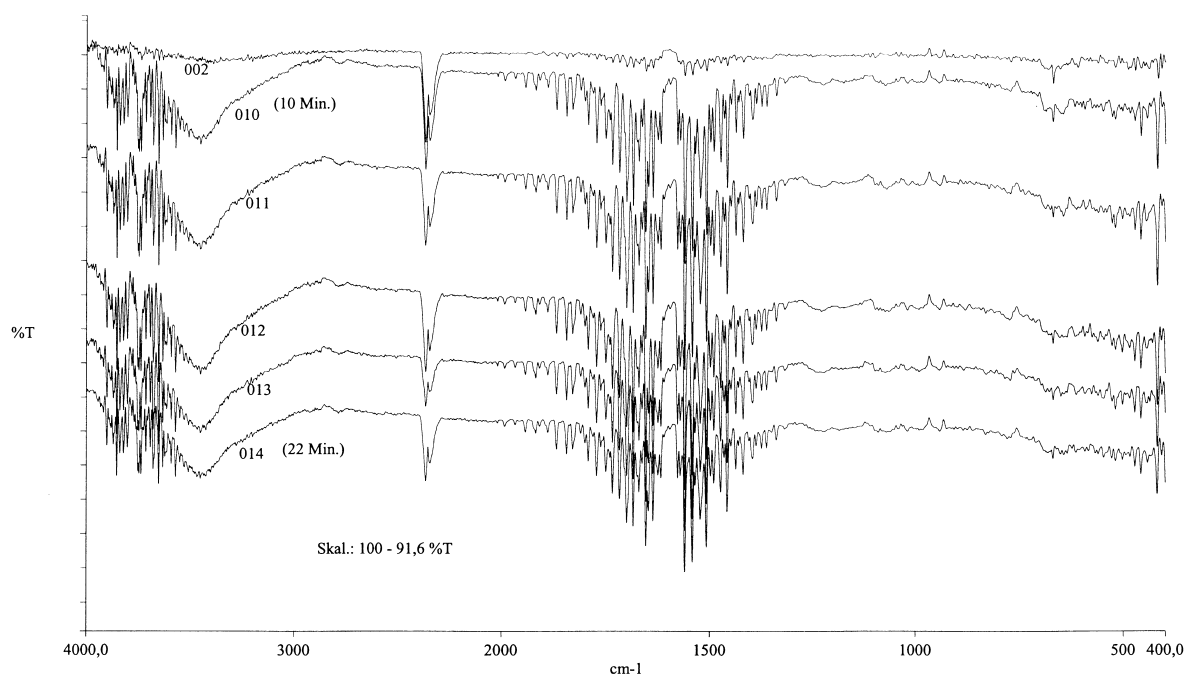


Figure D.1: Ir spectra showing the evaporation of H<sub>2</sub>O and CO<sub>2</sub>.

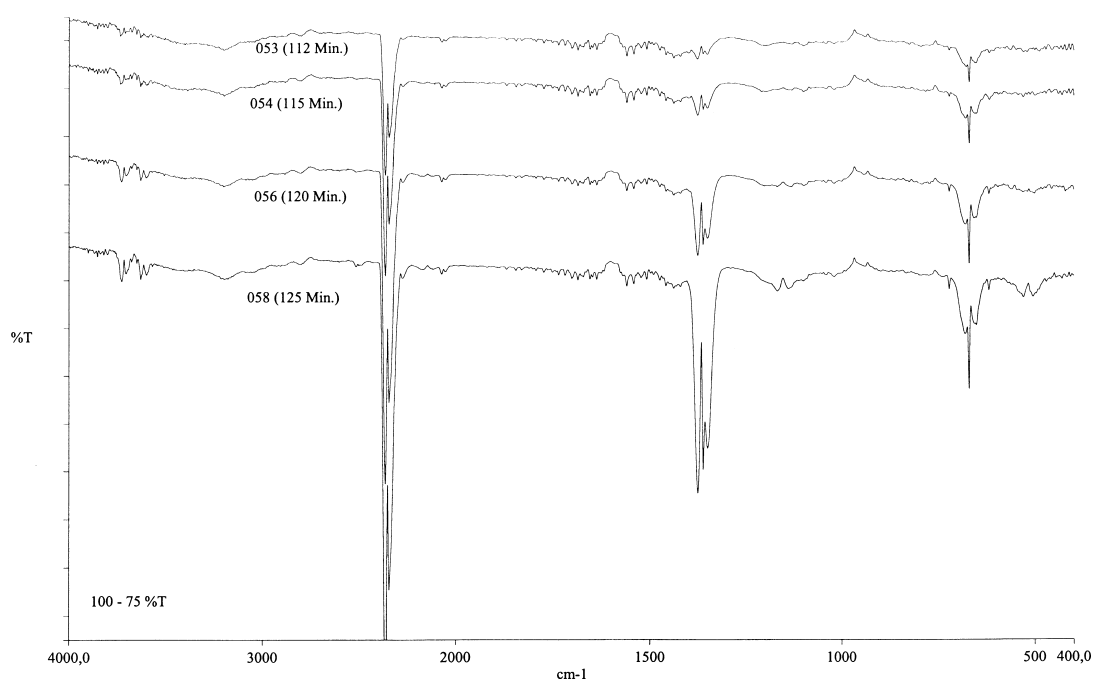
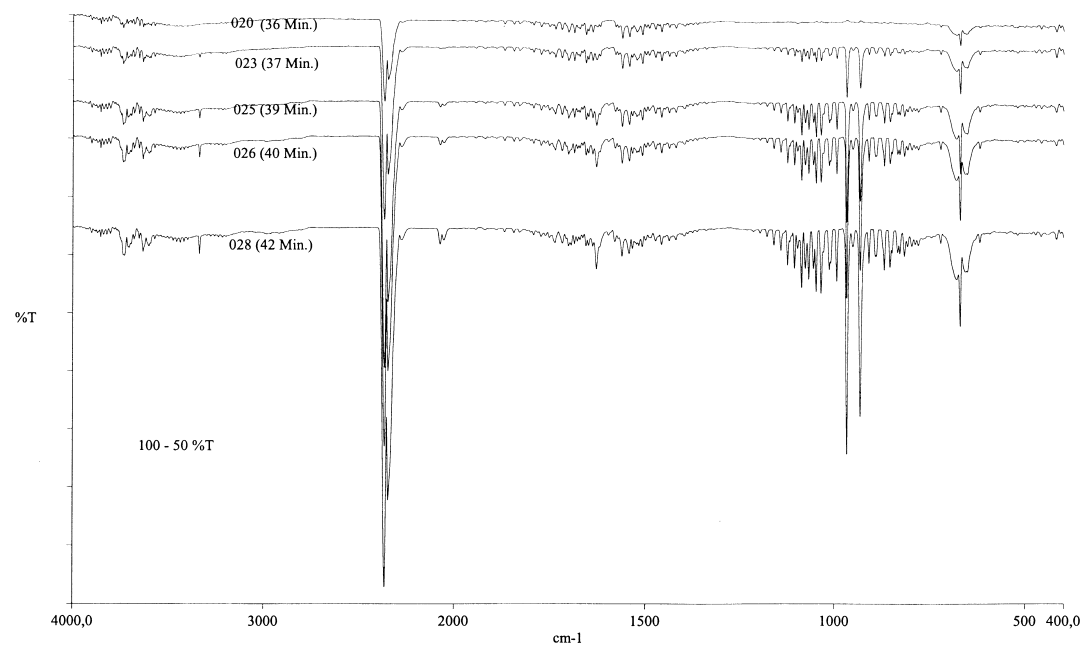


Figure D.2: Ir spectra showing the evaporation of  $\text{NH}_3$  and  $\text{CO}_2$  (upper spectra) and  $\text{SO}_2$  and  $\text{CO}_2$  (lower spectra).

# Appendix E

## Composition

### E.1 Ethanol isolated powders

	C [wt%]	H [wt%]	N [wt%]	S [wt%]
<b>DP350</b>	7.05	1.92	2.58	20.45
<b>DP700</b>	5.19	2.53	3.51	19.97
<b>DP1050</b>	6.05	1.27	2.34	21.06
<b>DP1400</b>	5.48	1.33	2.01	21.98
<b>DP1750</b>	5.43	1.3	2.04	20.96
<b>DP2100</b>	5.1	1.12	1.93	20.62
<b>DP2450</b>	5.65	1.37	2.12	22.11

Table E.1: C, H, N and S content from CHNS analysis

	Zn [wt%]
<b>DP350</b>	29.6
<b>DP700</b>	34.3
<b>DP1050</b>	22.7
<b>DP1400</b>	23.7
<b>DP1750</b>	23.1
<b>DP2100</b>	21.5
<b>DP2450</b>	20.8

Table E.2: Zn content from AES-ICP spectrometry.



	Zn [wt%]
<b>DP350</b>	22.9
<b>DP700</b>	27.5
<b>DP1050</b>	19.6
<b>DP1400</b>	19
<b>DP1750</b>	17
<b>DP2100</b>	19
<b>DP2450</b>	20.9

Table E.3: Zn content from titration.

## E.2 Freeze dried powders

	C [wt%]	H [wt%]	N [wt%]	S [wt%]
<b>0.2</b>	5.77	0.62	1.89	22.48
<b>0.25</b>	7.17	0.89	2.4	22.48
<b>0.3</b>	6.44	0.68	2.02	20.91
<b>0.35</b>	7.39	1.5	2.13	20.34
<b>0.4</b>	5.61	0.8	1.55	19.68
<b>0.45</b>	6.38	0.74	2.25	20.65
<b>0.5</b>	6.97	0.59	2.55	19.39

Table E.4: C, H, N and S content from CHNS analysis.

	Zn [wt%]
<b>0.2</b>	0.44
<b>0.25</b>	0.44
<b>0.3</b>	0.43
<b>0.35</b>	0.41
<b>0.4</b>	0.43
<b>0.45</b>	0.43
<b>0.5</b>	0.45

Table E.5: Zn content from AES-ICP spectrometry.

<b>Zn [wt%]</b>	
<b>0.2</b>	3.5
<b>0.25</b>	3.1
<b>0.3</b>	3
<b>0.35</b>	3.1
<b>0.4</b>	3.2
<b>0.45</b>	3.2
<b>0.5</b>	3.5

Table E.6: Zn content from titration.

# Appendix F

## Particle concentration

To calculate the particle concentration, we assume that all particles have a diameter of 5 nm, that there are 5.5 g ZnS without surfactant in 1l of dispersion and that the particles have the bulk density of 4.1 g/ml. With this we obtain for the particle volume  $V_P$  and the mass  $m_P$ :

$$V_P = \frac{4}{3} \cdot \pi \cdot r^3 = 6.5 \cdot 10^{-26} m^3 \quad (\text{F.1})$$

$$m_P = \rho \cdot V_P = 2.7 \cdot 10^{-22} kg = 2.7 \cdot 10^{-19} g \quad (\text{F.2})$$

To calculate the particle concentration with this, one has to know the molar mass  $M_P$  of the particles which can be calculated with Avogadro's constant:

$$M_P = N_A \cdot m_P = 161597 \frac{g}{mol} \quad (\text{F.3})$$

So with about 5.5 g of ZnS in 1l, we obtain the particle concentration:

$$c_P = 0.035 \frac{mmol}{l}$$

This corresponds to a particle density

$$N = 2.57 \cdot 10^{-22} \frac{1}{m^3}$$

# Appendix G

## Magnetization measurements

For seven ZnS:Mn samples the susceptibility was determined and it could be seen that they samples show a Curie-Weiss behaviour. The Curie-Weiss constants and temperatures can be seen in table G.1. The Curie-Weiss temperatures for all samples were very close to zero, indicating no significant antiferromagnetic interactions associated with Mn<sup>2+</sup> cluster formation. The respective Curie constants can be represented as:

$$C = \frac{N \cdot g^2 \cdot \mu_B^2 \cdot S(S+1)}{3 \cdot k_B} \quad (\text{G.1})$$

where N is the number of magnetic ions, g is the Lande constant, S is the spin associated with the Mn<sup>2+</sup> ion (5/2),  $\mu_B$  is the Bohr magneton and  $k_B$  the Boltzmann constant.

Table G.1: Curie constants and Curie-Weiss temperatures for Mn<sup>2+</sup> samples. The Mn<sup>2+</sup> contents were determined with atomic absorption spectroscopy (AAS).

Mn <sup>2+</sup> [ $\mu\text{g}$ ] in 1g ZnS	C [ $\times 10^{-5}$ ]	T <sub>C</sub> [K]
84	0.8	0.04
132	1.76	0.08
232	2.03	0.19
314	2.77	-0.07
346	2.98	0.28
402	3.58	0.17
570	4.03	-0.12

Magnetization data taken at 1.8 K are represented in figure G.1 together with a fitting of the Brillouin equation. With the small amounts of  $\text{Mn}^{2+}$  present in the samples, the formation of pairs, triplets, etc. can be considered as extremely unlikely. This is evidenced by the magnetization data. The measured points can be fitted by a Brillouin equation with no significant discrepancies such as those associated with nearest neighbour interactions. This suggest that the  $\text{Mn}^{2+}$  is well distributed in the particles

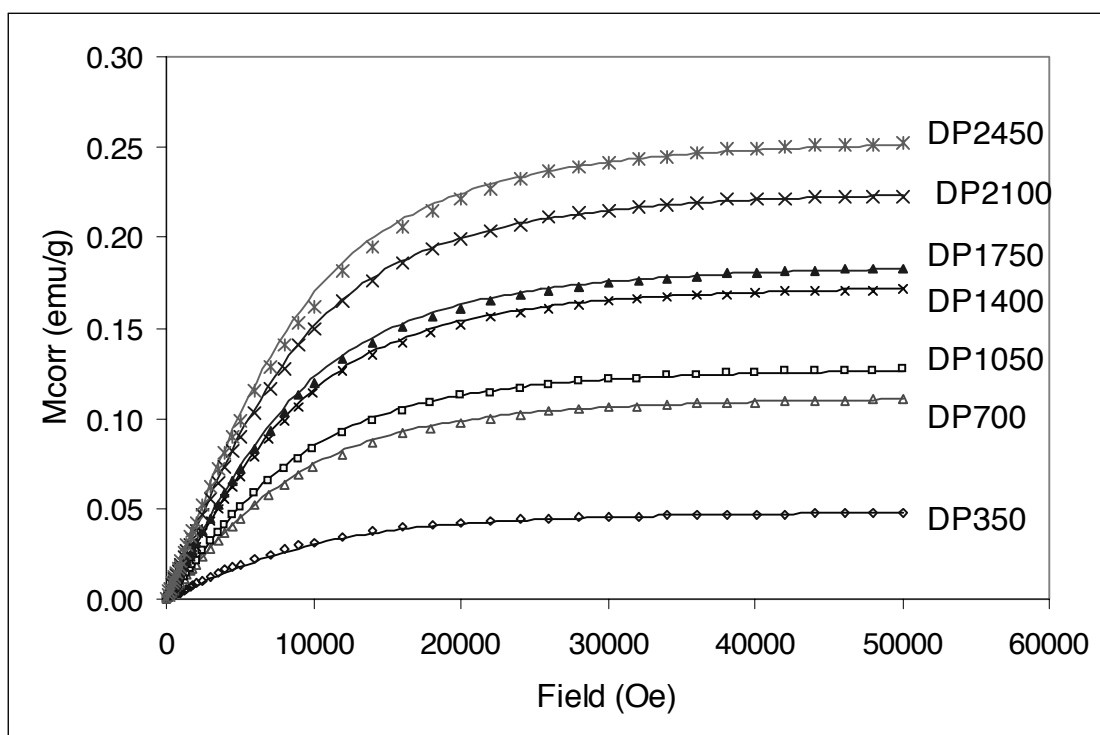


Figure G.1: Magnetization data for ZnS:Mn nanoparticle samples taken at 1-8 K. Experimental datas indicated by symbols, lines represent Brillouin fitting.

# Appendix H

## Bibliography

- [Ald01] J. Aldana, Y.A. Wang, X. Peng, *J. Am. Chem. Soc.*, **123**, 2001, 8844
- [Ate03] N. Atenco-Analco, F. Perez- Rodriguez, N.M. Makarov, *Superficies y Vacio*, **16**, 2003, 7
- [Atk98] P.W. Atkins, *Physical Chemistry*, Oxford University Press, Oxford Melbourne Tokyo, 1998
- [Ave67] M. Aven, J.S. Prener, *Physics and Chemistry of II-VI Compounds*, North Holland, Amsterdam, 1967
- [Baw90] M.G. Bawendi, M.L. Steigerwald, L.E. Brus, *Ann. Rev. Phys. Chem.*, **41**, 1990, 477
- [Bec83] W.G. Becker, A. J. Bard, *J. Phys. Chem.*, **87**, 1983, 4888
- [Ber63] D. Berlincourt, H. Jaffe, L.R. Shiozawa, *Phys. Rev.*, **129**, 1963, 1009
- [Bha94] R.N. Bhargava, D. Gallagher, T. Welker, *J. Lumin.*, **60&61**, 1994, 275
- [Bha94/2] R.N. Bhargava, D. Gallagher, X. Hong, A. Nurmikko, *Phys. Rev. Lett.*, **72**, 1994, 416
- [Bha96] R.N. Bhargava, *J. Lumin.*, **70**, 1996, 85
- [Bha02] B. Bhattacharjee, D. Ganguli, S. Chaudhuri, A.K. Pal, *Thin Solid Films*, **422**, 2002, 98
- [Bha02/2] B. Bhattacharjee, D. Ganguli, K. Iakoubovskii, A. Stesmans, S. Chaudhuri, *Bull. Mater. Sci.*, **25**, 2002, 175
- [Bol98] A.A. Bol, A. Meijerink, *Phys. Rev. B*, **58**, 1998, 15997
- [Bol00] A.A. Bol, A. Meijerink, *J. Lumin.*, **87-89**, 2000, 315

- [Bol01] A.A. Bol, A. Meijerink, *Phys. Stat. Sol (b)*, **224**, 2001, 291
- [Bol01/2] A.A. Bol, A. Meijerink, *J. Phys. Chem. B*, **105**, 2001, 10197
- [Bol02] A.A. Bol, J. Ferwerda, J.A. Bergwerff, A. Meijerink, *J. Lumin.*, **99**, 2002, 325
- Bör00 L. Börger, H. Cölfen, M. Antonietti, *Coll. Surf. A: Physicochem. Engin. Aspects*, **163**, 2000, 29
- [Bro95] Instruction manual for 90Plus/BI-MAS, Multi angle particle sizing option, Operation manual, Brookhaven Instruments, New York, 1995
- [Bru83] L.E. Brus, *J. Chem. Phys.*, **79**, 1983, 5566
- [Bru84] L.E. Brus, *J. Chem. Phys.*, **80**, 1984, 4403
- [Bru98] M. Bruchez jr, M. Moronne, P. Gin, S. Weiss, A.P. Alivisatos, *Science*, **281**, 1998, 2013
- [Buh85] W.E. Buhro, V.L. Colvin, *Nature Materials*, **2**, 2003, 138
- [Bur81] C. Burgess, A. Knowles (ed.), *Standards in absorption spectrometry*, London, New York, Chapman and Hall, 1981
- [Cav69] D. Cavallini, *Arch. Biochem. Biophys.*, **130**, 1969, 354
- [Cha98] W.C.W. Chan, S. Nie, *Science*, **281**, 1998, 2016
- [Che01] W. Chen, R. Sammynaiken, Y. Huang, J.-O. Malm, R. Wallenberg, J.-O. Bovin, V. Zwiller, N.A. Kotov, *J. Appl. Phys.*, **89**, 2001, 1120
- [Cöl00] H. Cölfen, M. Antonietti, *Adv. Poly. Sci.*, **150**, 2000, 67
- [Cou96] G. Counio, S. Esnouf, T. Gacoin, J.P. Boilot, *J. Phys. Chem.*, **100**, 1996. 20021
- [Cou98] G. Counio, T. Gacoin, J.P. Boilot, *J. Phys. Chem. B*, **102**, 1998, 5257
- [Cre87] CRC Handbook of Chemistry and Physics, CRC Press Inc, Florida, USA, 1987
- [Cul78] B.D. Cullity, *Elements of x-ray diffraction*, Second Edition, Addison Wesley Publishing Company, InC, London, 1978
- [Dab97] B.O. Dabbousi, J. Rodriguez-Viejo, F.V. Mikulec, J.R. Heine, H. Mattoussi, R. Ober, K.F. Jensen, M.G. Bawendi, *J. Phys. Chem. B*, **101**, 1997, 9463

- [Dah01] M. Dahan, T. Laurence, F. Pinaud, D.S. Chemal, A.P. Alivisatos, S. Weiss, *Opt. Lett.*, **26**, 2001, 825
- [Dal91] L.-V. Dalmay, *The Handbook of Infrared and Raman Characteristic Frequencies of Organic Molecules*, Academic Press Inc, 1991
- [Dem71] J.N. Demas, G.A. Crosby, *J. Phys. Chem.*, **75**, 1971, 991
- [Din99] A.D. Dinsmore, D.S. Hsu, H.F. Gray, S.B. Qadri, Y. Tian, B.R. Ratna, *Appl. Phys. Lett.*, **75**, 1999, 802
- [Eth03] A.S. Ethiraj, N. Hebalkar, S.K. Kulkarni, R. Pasricha, J. Urban, C. Dem, M. Schmitt, W. Kiefer, L. Weinhardt, S. Joshi, R. Fink, C. Heske, C. Kumpf, E. Umbach, *J. Chem. Phys.*, **118**, 2003, 8945
- [Eva59] H. Evans, E. McKnight, *Am. Mineral.*, **44**, 1959, 1210
- [Eva99] D.F. Evans, H. Wennerström, *The colloidal domain*, Wiley-VCH New York, 1999
- [Eve92] D.H. Everett, *Grundzge der Kolloidwissenschaft*, Steinkopff Verlag Darmstadt, 1992,32
- [Eyc00] A. Eychmüller, *J. Phys. Chem. B*, **104**, 2000, 6514
- [Fen87] J.H. Fendler, *Chem. Rev.*, **87**, 1987, 877
- [Fis86] C.H. Fischer, H. Weller, A. Fojtik, C. Lume-Pereira, E. Janata, A. Henglein, *Ber. Bunsenges. Phys. Chem.*, **90**, 1986, 46
- [Fis89] C.H. Fischer, J. Lilie, H. Weller, L. Katsikas, A. Henglein, *Ber. Bunsenges. Phys. Chem.*, **93**, 1989, 61
- [Fla99] R. Flatt, *Interparticle forces and superplasticizers in cement suspensions*, EPFL Thesis No 2040, 1999
- [Fla03] R.J. Flatt, P. Bowen, *Cem. Concr. Res.*, **33**, 2003, 781
- [Foj84] A. Fojtik, H. Weller, U. Koch, A. Henglein, *Ber. Bunsenges. Phys. Chem.*, **88**, 1984, 969
- [Fri00] J. Fritz, M.K. Baller, H.P. Lang, H. Rothuizen, P. Vettiger, E. Meyer, H.-J. Guntherodt, C. Gerber, J.K. Gimzewski, *Science*, **288**, 2000, 316
- [Gal94] D. Gallagher, W.E. Heady, J.M. Racz, R.N. Bhargava, *J. Crystal Growth*, **138**, 1994, 970
- [Gal95] D. Gallagher, W.E. Heady, J.M. Racz, R.N. Bhargava, *J. Mater. Res.*, **10**, 1995, 870



- [Gap98] S.V. Gaponenko, *Optical Properties of Semiconductor Nanocrystals*
- [Gen98] P.-G. de Gennes, *Croat. Chem. Acta*, **71**, 1998, 833
- [Ger95] E. Gerdes, *Qualitative Anorganische Analyse*, Vieweg Verlag, Braunschweig/Wiesbaden, 1995
- [Ger01] D. Gerion, F. Pinaud, S.C. Williams, W.J. Parak, D. Zanchet, S. Weiss, A.P. Alivisatos, *J. Phys. Chem. B*, **105**, 2001, 8861
- [Gum81] H.-E. Gumlich, *J. Lumin.*, **23**, 1981, 73
- [Gur56] F.R.N. Gurd, *Adv. Protein Chem.*, **62**, 1956, 335
- [Har92] S.E. Harding, A.J. Rowe, J.C. Horton, *Analytical Ultracentrifugation in Biochemistry and Polymer Science*, Royal Society of Chemistry, Cambridge, 1992
- [Häs93] A. Hässelbarth, A. Eychmüller, H. Weller, *Chem. Phys. Lett.*, **203**, 1993, 271
- [Heb01] N. Hebalkar, A. Lobo, S.R. Sainkar, S.D. Pradhan, W. Vogel, J. Urban, S.K. Kulkarni, *J. Mater. Sci.*, **36**, 2001, 4377
- [Hen89] A. Henglein, *Chem. Rev.*, **89**, 1989, 1861
- [Hin96] M.A. Hines, P. Guyot-Sionnest, *J. Phys. Chem.*, **100**, 1996, 468
- [His91] A. His, *J. Coll. Interf. Sci.*, **144**, 1991, 282
- [Hoe92] C.F. Hoener, K.A. Allan, A.J. Bard, A. Campion, M.A. Fox, T.E. Mallouk, S.E. Webber, J.M. White, *J. Phys. Chem.*, **96**, 1992, 3812
- [Hof96] H. Hofmeister, J. Dutta, H. Hofmann, *Phys. Rev. B*, **54**, 1996, 2856
- [Hol95] A.F. Hollemann, E. Wiberg, N. Wiberg, *Lehrbuch der Anorganischen Chemie*, 101. Edition, Walter de Gruyter, Berlin · New York, 1995
- [Hun89] R.J. Hunter, *Foundations of Colloid Science*, Vol. 1, Clarendon Press, Oxford, UK, 1989
- [Iga02] T. Igarashi, T. Kusunoki, K. Ohono, T. Isobe, M. Senna, *Mater. Res. Bull.*, **37**, 2002, 533
- [Ito97] H. Ito, T. Takano, T. Kuroda, F. Minami, H. Akinaga, *J. Lumin.*, **72-74**, 1997, 342
- [Jin96] C. Jin, J. Yu, L. Sun, K. Dou, S. Hou, J. Zhao, Y. Chen, S. Huang, *J. Lumin.*, **66&67**, 1996, 315

- [Kal02] N. Kallay, S. Zalac, *Colloid and Interface Science*, **253**, 2002, 70
- [Kan99] R.S. Kane, R.E. Cohen, *Chem. Mater.*, **11**, 1999, 90
- [Kat94] J.E.B. Katari, V.L. Colvin, A.P. Alivisatos, *J. Phys. Chem.*, **98**, 1994, 4109
- [Ken95] T.A. Kennedy, E.R. Glaser, P.B. Kelin, R.N. Bhargava, *Phys. Rev. B*, **52**, 1995, R14356
- [Kho95] A.A. Khosravi, M. Kundu, B.A. Kuruvilla, G.S. Shekhawat, R.P. Gupta, A.K. Sharma, P.D. Vyas, S.K. Kulkarni, *Appl. Phys. Lett.*, **67**, 1995, 2506
- [Kho00] R. Kho, C.L. Torres-Martinez, R.K. Mehra, *J. Colloid. Interf. Sci.*, **227**, 2000, 561
- [Kit99] C. Kittel, *Einführung in die Festkörperphysik*, Oldenbourg Verlag, München, Wien, 1999
- [Kor90] A. Kortan, R. Hull, R. Opila, M. Bawendi, M. Steigerwald, P. Carroll, L.E. Brus, *J. Am. Chem. Soc.*, **112**, 1990, 1327
- [Lak83] J.R. Lakowicz, *Principles of Fluorescence Spectroscopy*, Kluwer Academic/Plenum Publishers, New York, 1983
- [Lak99] J.R. Lakowicz, *Principles of Fluorescence Spectroscopy*, Kluwer Academic/Plenum Publishers, New York, 1999
- [Lak00] J.R. Lakowicz, I. Gryczynski, Z. Gryczynski, K. Nowaczyk, C.J. Murphy, *Anal. Biochem.*, **280**, 2000, 128
- [Law71] P. Lawaetz, *Phys. Rev. B*, **4**, 1971, 3460
- [Lee99] J. Leeb, V. Gebhardt, G. Müller, D. Haarer, D. Su, M. Giersig, G. McMahon, L. Spanhel, *J. Phys. Chem. B*, **103**, 1999, 7839
- [Lev97] L. Levy, N. Feltin, D. Ingert, M.P. Pileni, *J. Phys. Chem. B*, **101**, 1997, 9153
- [Lew00] J. A. Lewis, H. Matsuyama, G. Kirby, S. Morissette, J.F. Young, *J. Am. Ceram. Soc.*, **83**, 2000, 1905
- [Li01] L.-S. Li, J. Hu, W. Yang, A.P. Alivisatos, *Nano Letters*, **1**, 2001, 349
- [Lip89] P.E. Lippens, M. Lannoo, *Phys. Rev. B*, **39**, 1989, 10935
- [Liu00] J. Liu, J. Alvarez, A.E. Kaifer, *Adv. Mater.*, **12**, 2000, 1381

- [Mah00] R. Mahtab, H.H. Harden, C.J. Murphy, *J. Am. Chem. Soc.*, **122**, 2000, 14
- [Mam01] N.N. Mamedova, A.L. Rogach, J. Studer, *Nano Lett.*, **1**, 2001, 281
- [Man00] L. Manna, E.C. Scher, A.P. Alivisatos, *J. Am. Chem. Soc.*, **122**, 2000, 12700
- [Mat00] H. Mattoussi, J.M. Mauro, E.R. Goldman, G.P. Anderson, V.C. Sundar, F.V. Mikulec, M.G. Bawendi, *J. Am. Chem. Soc.*, **122**, 2000, 12142
- [Mat01] H. Mattoussi, J.M. Mauro, E.R. Goldman, T.M. Green, G.P. Anderson, V.C. Sundar, M.G. Bawendi, *Phys. Stat. Sol.*, **224**, 2001, 277
- [Mee83] S.R. Meech, D. Phillips, *J. Photochem.*, **23**, 1983, 193
- [Mit99] G.P. Mitchell, C.A. Mirkin, R.L. Letsinger, *J. Am. Chem. Soc.*, **121**, 1999, 8122
- [Moe00] P. Moeckle, *Powder characterization, X-ray diffraction*, 2000
- [Mur93] C.B. Murray, D.J. Norris, M.G. Bawendi, *J. Am. Chem. Soc.*, **115**, 1993, 8706
- [Mur99] N. Murase, R. Jagannathan, Y. Kanematsu, M. Watanabe, A. Kurita, K. Hirata, T. Yazawa, T. Kushida, *J. Phys. Chem. B*, **103**, 1999, 754
- [Par02] W.J. Parak, D. Gerion, D. Zanchet, A.S. Woerz, T. Pellegrino, C. Micheel, S.C. Williams, M. Steitz, R.E. Bruehl, Z. Bryant, C. Bustamante, C.R. Bertozzi, A.P. Alivisatos, *Chem. Mater.*, **14**, 2002, 2113
- [Par03] W.J. Parak, D. Gerion, T. Pellegrino, D. Zanchet, C. Micheel, S.C. Williams, R. Boudreau, M.A Le Gros, C.A. Larabell, A.P. Alivisatos. *Nanotechnology*, **14**, 2003, R15
- [Pen97] X. Peng, M.C. Schlamp, A.V. Kadavanich, A.P. Alivisatos, *J. Am. Chem. Soc.*, **119**, 1997, 7019
- [Pen98] X. Peng, J. Wickham, A. P. Alivisatos, *J. Am. Chem. Soc.*, **120**, 1998, 5354
- [Pen00] X. Peng, L. Manna, W. Yang, J. Wickham, E. Scher, A. Kadavanich, A.O. Alivisatos, *Nature*, **404**, 2000, 59
- [Pho91] B.E.A. Saleh, M.C. Teich, *Fundamentals in Photonics*, Wiley Interscience, New York, 1991, 454-456

- [Ral93] G. Ralston, *Introduction to analytical ultracentrifugation*, Beckman, USA, 1993
- [Rog00] A.L. Rogach, D. Nagesha, J.W. Ostrander, M. Giersig, N.A. Kotov, *Chem. Mater.*, **12**, 2000, 2676
- [Rie69] H.M. Rietveld, *J. Appl. Cryst.*, **2**, 1969, 65
- [Rie88] H.M. Rietveld, *Aust. J. Phys.*, **41**, 1988, 113
- [Ros83] R. Rosseti, S. Nakahara, L.E. Brus, *J. Chem. Phys.*, **79**, 1983, 1086
- [Ros84] R. Rosseti, J.L. Ellison, J.M. Gibson, L.E. Brus, *J. Chem. Phys.*, **80**, 1984, 4464
- [Ros85] R. Rosseti, R. Hull, J.M. Gibson, L.E. Brus, *J. Chem. Phys.*, **82**, 1985, 552
- [Rus89] W.B. Russel, D.A. Saville, W.R. Schowalter, *Colloidal Dispersions*, Cambridge University Press, Cambridge, 1989
- [Sch94] G. Schmid, *Clusters and colloids*, Wiley VCH, New York, 1994
- [Sch00] P. Schuck, *Biophys. J.*, **78**, 2000, 1606
- [Soh98] U. Sohling, G. Jung, D.U. Saenger, S. Lu, B. Kutsch, M. Menning, *J. Sol-Gel Sci. Techn.*, **13**, 1998, 685
- [Shi65] H. Shindo, T.L. Brown, *J. Am. Chem. Soc.*, **87**, 1965, 1904
- [Son96] L. Song, C.A. Varma, J.W. Verhoeven, H.J. Tanke, *Biophys. J.*, **70**, 1996, 2959
- [Soo96] K. Sooklal, B.S. Cullum, S.M. Angel, C.J. Murphy, *J. Phys. Chem.*, **100**, 1996, 4551
- [Spa87] L. Spanhel, M. Haase, H. Weller, A. Henglein, *J. Am. Chem. Soc.*, **109**, 1987, 5649
- [Spi93] J. Spinke, M. Liley, H.-J. Guder, L. Angermaier, W. Knoll, *Langmuir*, **9**, 1993, 1821
- [Sta97] W.F. Stafford, *Curr. Opin. Biotechn.*, **8**, 1997, 14
- [Ste88] M.L. Steigerwald, A.P. Alivisatos, J.M. Gibson, T.D. Harris, R. Kortan, A.J. Muller, A.M. Thayer, T.M. Duncan, D.C. Douglass, L.E. Brus, *J. Am. Chem. Soc.*, **110**, 1988, 3046
- [Ste90] M. Steigerwald, L.E. Brus, *Acc. Chem. Res.*, **23**, 1990, 183

- [Stö68] W. Stöber, A. Fink, E. Bohn, *J. Colloid Interface Sci.*, **26**, 1968, 62
- [Sun98] L. Sun, C. Yan, C. Liu, C. Liao, D. Li, J. Yu, *J. Alloys and Compounds*, **275-277**, 1998, 234
- [Sun99] L. Sun, C. Liu, C. Liao, C. Yan, *Solid State Comm.*, **111**, 1999, 483
- [Sve23] T. Svedberg, J.B. Nichols, *J. Am. Chem. Soc.*, **45**, 1923, 2910
- [Swa53] F. Swanson, *Natl. Bur. Stand. (US)*, Circ. **539**, 1953, II 16
- [Uzu03] N. Uzunbojakava, C. Otto, *Optics letters*, **28**, 2003, 2073
- [Vel01] K.P. Velikov, A. van Blaaderen, *Langmuir*, **17**, 2001, 4779
- [Wan87] Y. Wang, A. Suna, W. Mahler, R. Kasowski, *J. Chem. Phys.*, **87**, 1987, 7315
- [Wan87/2] Y. Wang, N. Herron, *J. Phys. Chem.*, **91**, 1987, 257
- [Wan91] Y. Wang, N. Heron, K. Moller, T. Bein, *Solid State Com.*, **77**, 1991, 33
- [Wed97] G. Wedler, *Lehrbuch der physikalischen Chemie*, Wiley-VCH Verlag Weinstadt, 1977, 439
- [Wei88] J. Weidlein, *Schwingungsspektroskopie*, Georg Thieme Verlag, 1988
- [Wel93] H. Weller, *Angew. Chem. Int. Ed. Engl.*, **32**, 1993, 41
- [Wil01] D.M. Willard, L.L. Carillo, J. Jung, A. van Orden, *Nano Lett.*, **1**, 2001, 469
- [Yu96] I. Yu, T. Isobe, M. Senna, *J. Phys. Solids*, **57**, 1996, 373
- [Yu97] J. Yu, H. Liu, Y. Wang, F.E. Fernandez, W. Jia, L. Sun, C. Jin, D. Li, J. Liu, S. Huang, *Opt. Lett.*, **22**, 1997, 913



# Curriculum Vitae

AXMANN Yvonne  
Rue de l'Industrie 5  
CH-1020 Renens  
yaxmann@web.de

21.04.1976  
German  
single  
+41 (0)21 693 68 06

## Education

2001-2004	Swiss Institute of Technology, Lausanne, Switzerland Powder Technology Laboratory PhD Thesis
2001	Swiss Institute of Technology, Lausanne, Switzerland Powder Technology Laboratory Diploma Thesis
1996-2001	University of Ulm, Ulm, Germany Chemistry studies Specialization in analytical chemistry
1987-1996	Burg-Gymnasium, Schorndorf, Germany Maturity

## Publications

Y.Axmann, A. Petri, H. Hofmann,  
ZnS Nanoparticles: Synthesis and Characterization,  
*MRS Fall Meeting Proceedings*, N11.23, 2003

## Hobbies

Sports	Mountain climbing, jogging, skiing
Music	Classical guitar (lessons during 8 years)
Other	Literature, cinema